Investigation of the California Undercurrent off the West Coast of Vancouver Island

by

Maxim Krassovski

diploma with thesis, Moscow State University, 1993

A Thesis Submitted in Partial Fulfillment of the
Requirements for the Degree of

MASTER OF SCIENCE

in the
School of Earth and Ocean Sciences

Supervisory Committee
Dr. Richard E. Thomson, Co-Supervisor (Department of Fisheries and Oceans and School of Earth and Ocean Sciences)
Dr. Christopher J. R. Garrett, Co-Supervisor (School of Earth and Ocean Sciences)
Dr. Richard K. Dewey, Departmental Member (School of Earth and Ocean Sciences)

University of Victoria

This thesis has been reformatted from the original version to save paper

To Maria and Peter

Abstract

Current meter records from a long term mooring site on the continental slope off the west coast of Vancouver Island, British Columbia, Canada are used to investigate the scales of variability of the subsurface California Undercurrent and its relation to possible driving mechanisms. Observed along the west coast of North America from Baja California to Vancouver Island, the California Undercurrent is part of the California Current System, a typical basin-scale eastern boundary circulation system. Of the four instruments at nominal depths of 35, 100, 175, and 400 m, the upper two show seasonally reversing flow, while the 175 m instrument registers a year-round poleward flow. The deepest current meter, located approximately 100 m above the bottom, reflects the influence of a nearby submarine canyon. The flow at 100 and 175 m depths, as well as the water properties sampled in the region with CTD casts, are characteristic of the temporal and spatial variability of the California Undercurrent over the continental slope off central and southern Vancouver Island. The correlation of the 175 m flow with local atmospheric forcing (wind stress) in the low-frequency band (periods of months) is higher than with ocean-wide climatic indices, suggesting that regional processes play a key role in the forcing of the subsurface flow.

Table of contents

List of tables

List of figures

Acknowledgments

I would like to express my deepest gratitude to my primary supervisor, Dr. Richard Thomson, who created a friendly and encouraging atmosphere and made every possible effort (including access to the data, regular discussions on the subject of research, editing the text, and financial support) to ensure efficiency and smoothness of my research. He also provided me with an opportunity to participate in scientific cruises and get a first-hand experience with modern oceanographic instrumentation. I am also very grateful to my co-primary supervisor, Dr. Chris Garrett, for his careful guidance through the research and educational process and many illuminating discussions and useful comments on the text. Dr. Richard Dewey's comments, as a supervisory committee member, have helped to improve the quality of the work. Many useful discussions with Drs. Alexander Rabinovich, Isaac Fine, George Shevchenko, and Evgueni Kulikov have greatly expanded my knowledge in many scientific subjects. Their comments on the text are also acknowledged. The comments and suggestions of the external examiner, Professor Barbara Hickey of the University of Washington, are also gratefully acknowledged. This work is based on the data collected during various scientific projects led by the Institute of Ocean Sciences, and in particular, the La Perouse project supervised by Dr. Richard Thomson. Andrew Lee, David Spear, Tomas Juhász, and Lucius Perreault from the Institute of Ocean Sciences helped with data error check. The work was funded from Dr. Richard Thomson's NSERC Discovery Grant. Last, but not least, I would like to thank my wife, Maria, who trusts that everything I do is good for our family, and my little son, Peter, who stoically endures the moments when I close the door behind me on my way to the office.

1. Introduction

Pronounced biological productivity, high marine traffic, and the potential for mineral resource exploration and extraction make the continental shelf and slope of the eastern North Pacific an area of high economic importance. As a consequence, oceanic processes from Baja California to northern British Columbia have been the focus of considerable research over the past few decades (e.g. Hickey, 1979, 1998; Freeland *et al.*, 1984; Crawford and Thomson, 1991; Pierce *et al.*, 2000; Collins *et al.*, 2004). Although much of the research effort by Canadian and American oceanographers has been directed toward the circulation of the surface ocean, there have been a few long-term measurements of shelf-slope currents along all the Eastern Pacific. In this study, I examine subsurface currents along the Eastern Pacific continental margin using current meter measurements from a slope location which has been occupied nearly continuously for the 20-year period 1985 to 2005.

The current meter series together with the water property data are examined to establish an understanding of the flow in the given location and its relation to atmospheric and oceanic forcing at different scales. Statistical, spectral, and tidal analyses are used to explore the characteristics of the flow. Basic temperature-salinity (T-S) analysis is used to examine the origin of the water type found in the study region. Statistical relation of the flow to different forcing mechanisms is established with correlation and regression analyses.

I evaluate statistical characteristics of the flow, its annual cycle and interannual anomalies, as well as the energy of fluctuations in different frequency bands at different depths. I also evaluate the relative importance of the main source water masses in composition of the water in the region of investigation. Finally, I calculate correlation with possible forcing factors or their proxy variables (wind stress, along-shore sea level gradient, and climate indices reflecting basin-scale processes).

2. Literature review

2.1. General geographical and oceanographic description of the northeast Pacific from California to Vancouver Island

The west coast of North America is characterised by high mountain ranges, numerous embayments and a mostly narrow continental shelf (Figure 2.1.1). Major headlands such as Cape Blanco, Cape Mendocino, and Point Conception disrupt the linear orientation of the coastline and submarine canyons complicate the bathymetry of the continental slope particularly north of the Columbia River. Here, unlike regions to the south, coastal fresh water discharge plays an important role in the shelf circulation as well as in the salt budget off British Columbia and Washington State (Royer, 1982; Reed and Elliott, 1973). The Columbia River, with a mean volume flow rate of 7300 m^3/s (Barnes *et al.*, 1972; Hill *et al*, 1998), inputs 77% of the total drainage between San Francisco and Juan de Fuca Strait (Hickey, 1979). The Fraser River, with a mean discharge rate of 2700 m^3/s (Roden, 1967), is also a major contributor to the net volume of fresh water entering the coastal region. Flows from these major rivers are significantly augmented by the large number of smaller streams and by direct runoff from coastal rainfall in the winter (LeBlond *et al.*, 1983). However, to the south of Columbia River, the climate is more arid and there are no large catchment basins. As a result, there are no major fresh water sources in this region and the total freshwater discharge tends to be low throughout most of the year. Exceptions to low discharge are found on the Oregon coast, where a number of smaller rivers provide substantial freshwater input to the coast during winter and southern California rivers which experience increased outflow during El Niño years (B. Hickey, pers. comm., 2008).

The dominant atmospheric systems in the eastern North Pacific are the North Pacific High and the Aleutian Low (Figure 2.1.2). Their relative strengths and positions undergo a distinct seasonal change. As a result, the interface between these two pressure systems is located at approximately 50° N in summer (the latitude of northern Vancouver Island) and near 40° N in winter (the latitude of San Francisco). The transition from one seasonal pattern to the other is usually quite abrupt and leads to "spring" and "fall" oceanic transitions (Strub *et al.*, 1987a; Thomson and Ware, 1996). The meridional orientation of the coastline and the existence of major orographic features along the west coast of North America facilitate the meridional propagation of orographically trapped atmospheric signals (Dorman, 1985; Mass and Albright, 1987; Hermann *et al.*, 1990; Reason and Dunkley, 1993). Another important influence of the high coastal mountain ranges is that they prevent penetration of continental air masses into the near-shore region. The region from northern California to Vancouver Island is characterised by strong wind forcing with intensive storms in winter with characteristic time scales of 3 to 10 days (Hickey, 1998; Hill *et al.*, 1998).

The upper 1000 m of the North Pacific is dominated by two basin-scale ocean gyres (the subtropical anticyclonic gyre and the subpolar cyclonic gyre) which are, in turn, driven by the large-scale atmospheric circulation patterns (Munk, 1950). The transition between these gyres takes the form of a broad eastward current known as the West Wind Drift or Subarctic Current (Tabata, 1975; Thomson, 1981; Bograd *et al.*, 1999). Upon reaching the continental margin of the eastern Pacific, the current bifurcates into the poleward flowing Alaska Current and the equatorward flowing California Current (CC) (Figure 2.1.1). The meridional location of the bifurcation area undergoes a distinct seasonal change in response to the seasonal change in the atmospheric patterns (e.g. Thomson and Ware, 1996). In winter, the bifurcation is located at approximately at 40°N, off Cape Mendocino, but shifts in summer to around 50°N, off the northern tip of Vancouver Island. Therefore, off Vancouver Island, the summer California Current is replaced in winter by the Alaska Current, both currents occupying a wide area along the coast extending seaward about 1000 km from the lower continental slope. Surface flow along the continental margin, confined to the area above the inner continental slope and outer shelf and driven by the local wind forcing, varies seasonally from the poleward Davidson Current (called the Northeast Pacific Coastal Current by Thomson and Gower, 1998) in winter to the equatorward Shelf-break Current in summer (Thomson and Gower, 1998). The California Undercurrent (CUC), also referred to in some early studies as the California Countercurrent (Reid, 1962, 1963; Reid *et al.*, 1958; Pavlova, 1966; Wickham, 1975), is a year-round subsurface poleward current extending from Baja California to Vancouver Island along the upper slope and outer shelf at depths below the main pycnocline (Hickey, 1979, 1989b, 1998; Pierce *et al.*, 2000). The California Undercurrent may not be distinguishable from the overlying Davidson Current in winter, forming a poleward current extending from the surface to the bottom. The California Current, the Davidson Current, and the California Undercurrent constitute the California Current System (CCS) (Hickey, 1979, 1998). Examples of cross-sections of measured along-shore velocity in summer off Vancouver Island and in summer and winter off Oregon are shown in Figure 2.1.3. The structure and variability in the CUC off southwestern British Columbia is the focus of the present study.

2.2. Oceanographic observations of the California Current System

A number of reviews have been published on eastern boundary currents, among them is a comprehensive review of the day's knowledge about the CCS by Hickey (1979) with a major update by Hickey (1998) and a description of ocean processes common to all eastern ocean boundaries by Hill *et al* (1998). In this section I will briefly review major observation programs off the west coast of North America and their main findings.

Figure 2.1.1. General geographic map and the schematic of major currents in the north-east Pacific. The white circle marks the location of a long-term current meter mooring site maintained by Fisheries and Oceans Canada, a primary source of data for the present study.

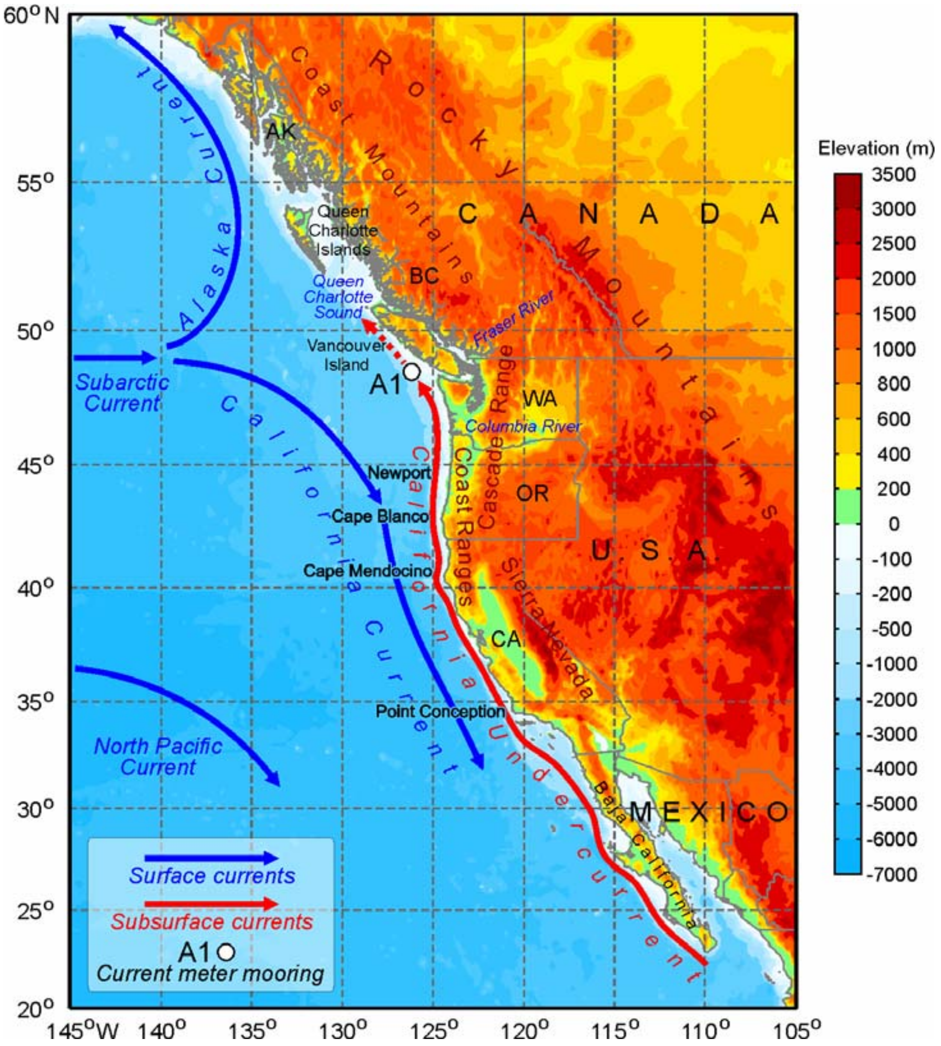

2.2.1. Major observation programs: a short review and historical perspective

Early scientific knowledge about the CCS was first obtained from hydrographic data. Among the earliest scientific observations of the CUC is the cruise of California Division of Fish and Game vessel "Bluefin" off southern California coast in 1937. The results were published by Sverdrup and Fleming (1941). From May to July of 1939, the cruise of R/V "E.W. Scripps" of Scripps Institution of Oceanography covered the area from Baja California to Oregon (Tibby, 1941). Water properties were measured along a number of cross-shore sections extending 500-700 km offshore. The data collected during the cruise were in good agreement with the flow pattern known at that time. Based on the assumption that the Pacific Equatorial and the Pacific Subarctic water are the primary water types involved in the formation of the water properties along the eastern margin of the North Pacific, it was determined by the T-S method that the largest percentage of the Equatorial Water was near the shore and below 200 m. Its maximum contribution decreased from 80% off Baja California to 40% off the Oregon coast (Tibby, 1941).

Several scientific programs with regular hydrographic samplings at standard hydrographic lines off the west coast of North America started in the 1950s and 60s. Hydrographic Line "P", extending from the entrance of Juan de Fuca Strait to Ocean Station Papa (50°N, 145°W), has one of the longest sampling records in the region. It was sampled regularly beginning in 1959 (Tabata and Weichselbaumer, 1992a, 1992b; Whitney and Freeland, 1999). The Line "P" data provide valuable insight into the variability of the northeast Pacific. The station spacing (40 km in the near-shore region), however, is too large to resolve the jet-like currents in the shelf-slope region. Beginning from 1979, the Institute of Ocean Sciences (IOS) in Sidney, BC, Canada, performed conductivity-temperature-depth (CTD) observations at many hydrographic lines across the shelf and slope off the British Columbia west coast with stations separated by about 10 km (Thomson *et al*., 1984). These data are used in the present study to derive mean seasonal circulation patterns off Vancouver Island (Section 5.1).

The Newport Hydrographic (NH) Line along 44.65°N off central Oregon was sampled seasonally from 1961 to 1971 and from mid-1997 through 2003 with some observations also available for 2004 and 2005 (Huyer *et al*., 2007). A large contribution to the knowledge about the CUC on its southern extent was provided by the California Cooperative Oceanic Fisheries Investigation (CalCOFI) program. The program started in 1949 with an aim to explore oceanographic conditions off the California coast and their impact on marine biological processes. The CalCOFI program includes regular quarterly water property surveys at standard cross-sections off the Mexico and California

Figure 2.1.2. Long term mean monthly sea level pressure (mbar) in the North Pacific for February and August from NCEP/NCAR Reanalysis data. The arrows show prevailing wind directions.

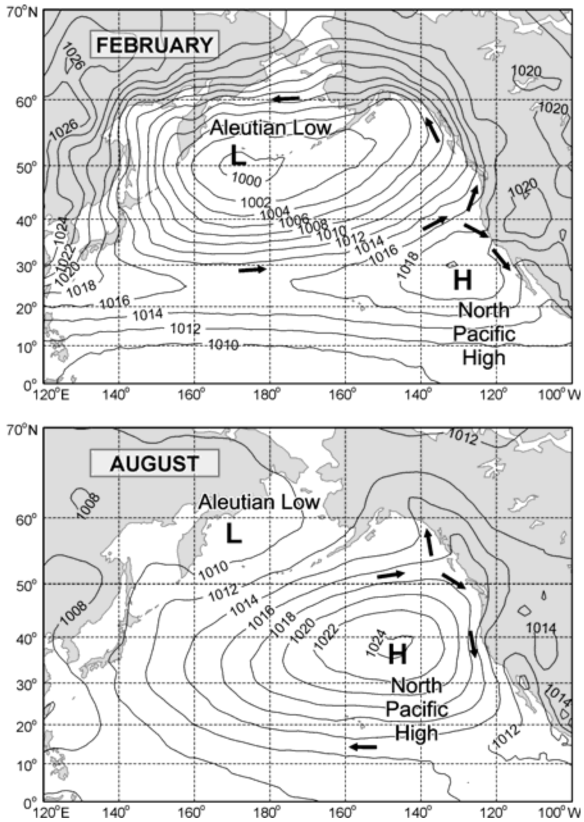

coasts. Early data reports and reviews can be found in Reid *et al.* (1958) and Hewitt (1988).

Ingraham (1967) presents the results of two water property surveys performed at nine cross-shore sections off the Washington and British Columbia coast during the spring and fall of 1963. Both surface and 200 m geostrophic flow was generally poleward with velocities on the order of 0.05-0.1 m/s. The flow (particularly in fall) was complicated by anticyclonic eddies above the continental slope with velocities reaching 0.15 m/s. The net along-shore volume transport was estimated to be 1 Sv in the poleward direction off Washington and 3 Sv off northern Vancouver Island. There was no significant change in along-shore transport from spring to fall. However, indirect evidence for intensification of the CUC and Davidson Current during the fall was found in the increased water temperatures and salinities, and decreased oxygen content, in the area during this season.

Reed and Halpern (1976) show dynamic topography calculations based on a salinity-temperature-depth (STD) survey (150 stations) performed off southern Vancouver Island and Washington State in September 1973. They determined a poleward transport of about 1 Sv, a vertical extent of the Undercurrent of more than 500 m, and high variability in the width of the poleward flow.

The first direct current measurements on the shelf of the Canadian west coast were performed from December 1974 to April 1975 (Huyer et al., 1976). One of two mooring sites was located at the shelf break off Tofino at the west coast of Vancouver Island. Its near-bottom instrument, at 200 m depth, recorded a mean along-shore current of 0.026 – 0.038 m/s in the poleward direction. A temperature rise was observed during the periods of prolonged poleward flow indicating the importance of advection in the formation of local water properties. The general flow indicated winter downwelling conditions.

The next current meter observations off the British Columbia coast were performed in 1979 – 1982. This was an extensive current meter survey, a part of the Coastal Ocean Dynamics Experiment (CODE, Thomson *et al.*, 1985; Huggett *et al.*, 1987). A brief description of the results can be found in (Freeland *et al.*, 1984). The moorings off Vancouver Island were located at cross-sections on La Perouse Bank, off Estevan Point, and off Brooks Peninsula. The measurements showed a seasonally reversing surface flow at all mooring locations and a prevailingly poleward subsurface (deeper than 150 m) flow. The strongest poleward subsurface currents were observed off Estevan Point with mean monthly values of up to 0.2 m/s seaward of the shelf break. A strong seasonal cycle was established in all records with the strongest poleward alongshore component in summer and fall.

The Vancouver Island Coastal Current Experiment was carried out from June to November 1984 and included current meter moorings at the shelf and shelf break off Vancouver Island (Hickey *et al.*, 1991). The instrument at 150 m depth moored at the shelf break off Tofino showed a very weak poleward flow in summer and significant poleward flow (>0.1 m/s) in fall.

The La Perouse project, started in 1985 and operated by the Institute of Ocean Sciences, includes four long-term current measurement sites in the shelf-slope region off Vancouver Island: Site A1 (Figure 2.1.1) on the continental slope off La Perouse Bank, Sites E1 and E3 on the shelf and slope off Estevan Point, and Site BP1 on the slope off Brooks Peninsula (Ware and Thomson, 1986). Sites A1 and E1 continue to be occupied at present, and are sites with some of the longest regular current measurements in the shelf-slope region of the Eastern Pacific. The data from Site A1 constitute the basis for the present work.

Several current meter surveys have been undertaken off Washington and Oregon since the 1970s. From July – September 1972, a current meter survey off southern Washington showed a narrow jet over the upper continental slope with mean maximum velocity of 16 cm/s at a core depth of 192 m (Hickey, 1979, 1989a). Measurements during the California Undercurrent Study experiment conducted from 1977 to 1978 with a set of current meter moorings deployed off Oregon (Huyer *et al.*, 1984) did not register a well defined subsurface core velocity. Among possible reasons for the lack of persistent subsurface flow in the current meter records are a weaker Undercurrent off Oregon or inadequate mooring placement to catch the core which may have shifted in the cross-shore direction due to the atypical, two-step shelf-break profile at the mooring location (B. Hickey, pers. comm., 2008). A strong warm-core eddy passing over the slope as well as gaps in the data may have also prevented establishing a reliable picture of the mean flow. Nevertheless, currents calculated from hydrographic data collected during this experiment show a narrow core of poleward flow over the upper slope off Washington and over the shelf break and outer shelf off Oregon (Hickey, 1989b).

A series of publications on drifter observations off central California (Collins *et al.*, 1996a, 1996b, 2003, 2004; Garfield *et al.*, 1999, 2001) describes the flow statistics of subsurface drifters off central and northern California between Point Conception and Cape Mendocino. The program of observations included 44 acoustically tracked floats which were deployed at pressure levels ranging from 150 to 600 dbar. For the zone of the CUC, the data show a maximum in the mean monthly alongshore velocity of 0.054 m/s in May-June and a minimum of 0.017 m/s in February. In addition to the annual peak, the seasonal cycle has a substantial semi-annual component which gives rise to a second maximum of about 0.04 m/s in November. The drifters showed the continuity of the flow in the zone of the CUC over a 500 km extent in the summer of 2003 (Collins *et al.*, 1996a; Garfield *et al.*, 1999), confirmed the existence of submesoscale eddies and

Figure 2.1.3. Cross-sections of measured along-shore current velocity (a) in July-August 1972 off the Washington coast (from Hickey, 1979), (b) in July 1980 off Estevan Point (from Freeland *et al*., 1984), and (c) seasonal average for summers of 1997-2003 (left panel) and winters of 1998, 2000-2003 (right panel) at the Newport Hydrographic Line (from Huyer *et al*., 2007). Velocity values in cm/s are marked in the plots with equatorward flow shaded in (a) and (b) and coloured with cyan in (c) and poleward flow left blank in (a) and (b) and coloured with magenta in (c).

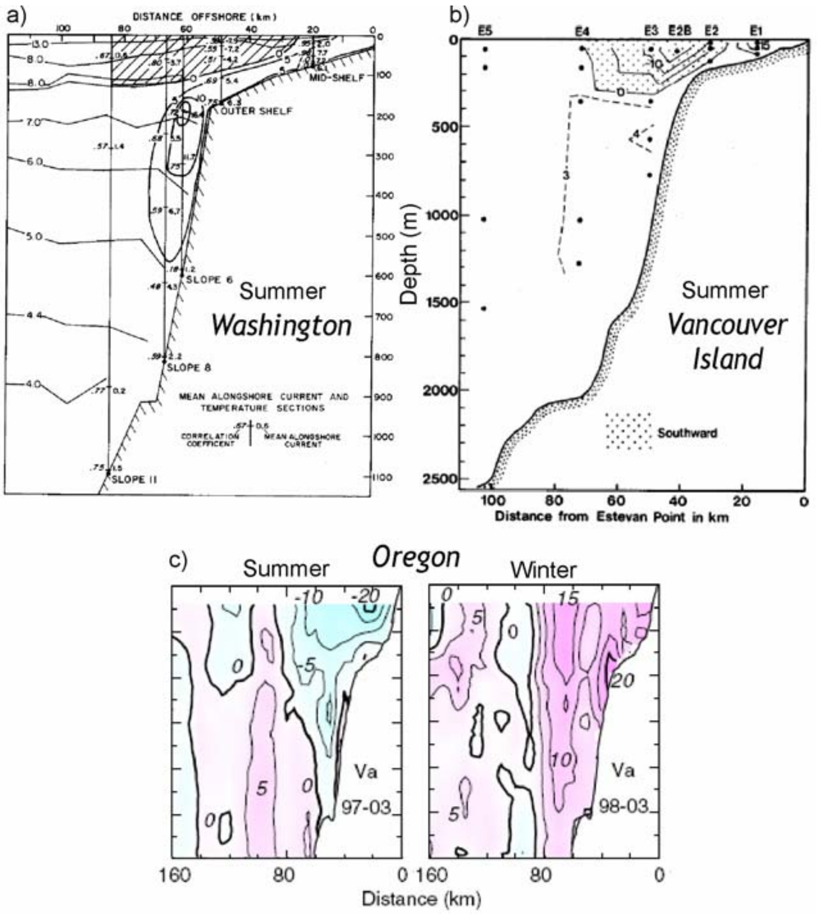

the dominance of anticyclonic eddies and westward drift farther offshore (Garfield *et al*., 1999), and provided estimates of the seasonal variability of the coastal flow (Collins *et al*., 2003; Collins *et al*., 2004). The observations also showed mean and eddy energies higher than those obtained with global high-resolution ocean models (Garfield *et al*., 2001).

Pierce *et al*. (2000) describe a considerable number of direct current measurements at regularly spaced cross-shelf sections. The observations were taken between the latitudes of 33° and 51°N during a July-August survey in 1995 by a ship-mounted Acoustic Doppler Current Profiler (ADCP). The data provide a “snapshot” of summer flow in the zone of the CUC. A poleward flow was generally observed in the depth range of 125 to 325 m with the core located between 200 and 275 m depth. The average vertical location of the core is the same at all latitudes with a possible slight shallowing to the north. The vertical maximum of "spiciness" (high temperature and salinity) can also be traced as far north as 51°N at depths of 150-225 m which is somewhat shallower than the velocity maximum. The maximum poleward velocity in the core of the Undercurrent was 0.2-0.22 m/s and the transport was 0.8 – 0.9 Sv except for the band from 43.5 to 48° N where the maximum velocity was 0.1 m/s and the transport was 0.2 Sv. The characteristic width of the Undercurrent changed with latitude consistent with the first mode baroclinic Rossby radius of deformation (cf. Gill, 1982). The Rossby radius changes from 24.3 km at 35°N to 15.5 km at 49°N (Chelton *et al*., 1998) and this is the approximate distance of the core of the Undercurrent from the shelf break. The decrease in poleward transport in the band from 43° to 48°N can be attributed in part to separation of the equatorward jet near Cape Blanco and its subsequent deepening and interaction with the poleward jet making the latter turn offshore and augment the equatorward flow (cf., Figure 12, Barth *et al*., 2000). Therefore, the large scale coastal promontories are likely to play a considerable role in the control of the poleward flow. Strengthening of the CUC further to the north indicates that its driving mechanism is active at least as far north as the region off Vancouver Island. Possible forcing factors will be discussed in Section 2.3.1.

A general picture of the circulation off the west coast of North America compiled from numerous observation programs includes the year-round broad equatorward-flowing surface CC, the slope-confined poleward-flowing subsurface CUC, the seasonal Davidson Current (in winter) inshore of the CC, and the Shelf-break Current in summer (the summer counterpart to the Davidson Current). In accordance with Thomson and Gower (1998), I distinguish the Shelf-break Current from the broader CC, since it has a distinct nature as an alongshore surface jet associated with upwelling conditions along the coast. Table 2.1.1 summarizes the characteristics of the above currents. The average velocities of the currents comprising the CCS are small (O(0.1) m/s). However, the structure of the flow is highly variable on different time scales (reviewed in the next section), and the instantaneous velocities associated with particular events can be much higher than the mean values.

Table 2.1.1. Characteristics of the currents comprising the California Current System.

	California Current	California Undercurrent	Davidson Current (Inshore countercurrent)/ Shelf-break Current
Direction; seasonal variability	Equatorward year-round (max in summer and early fall). Shifts location to north in summer.	Poleward for most of the year (max in summer and early fall, min in spring) may not be distinguishable from the Davidson Current or may be reversed in winter.	Poleward Davidson Current in fall and winter/ Equatorward Shelf-break Current in summer
Transport	10-12 Sv	1 Sv (down to 325m depth)	?
Dominant structure	Baroclinic	Baroclinic	Barotropic/Baroclinic
Vertical extent	Upper 100-1000 m	Depths of 100 - 500 m	Whole water column/ Upper 100 m
Core depth	Surface	150 - 250 m	No subsurface maximum/ surface-intensified
Horizontal extent	1000 km seaward from the base of slope	20 – 25 km seaward from the shelf break (within 150 km of the coast)	Outer shelf and slope/ shelf break
Width	Order of 1000 km	20 km (10 - 40 km)	100 km off California, 300 km off Washington /~30km
Mean alongshore velocities	~0.1 m/s	Varying from 0.3 to 0.05 m/s, from Baja California to Vancouver Island	~0.25 m/s / ~0.20 m/s
Water properties	Cool, low salinity Subarctic water	Warm, saline Equatorial waters	Equatorial waters/ Subarctic waters

2.2.2. Scales of variability

Tides and inertial oscillations

Tidal and inertial currents are very energetic narrow-band oscillations commonly observed throughout the ocean. In the shelf-slope region off Vancouver Island, diurnal tidal currents prevail over semidiurnal currents on the shelf, where they are mainly barotropic and comprised of a significant continental shelf wave component (Crawford and Thomson, 1982; Cummins *et al.*, 2000). Semidiurnal tidal currents prevail on the outer slope (Crawford and Thomson, 1982) and have a significant baroclinic part resulting from internal wave generation at the shelf break (Drakopoulos and Marsden, 1993; Cummins *et al.*, 2001).

The local inertial frequency changes with latitude from double the Earth's rotation rate at the pole to zero at the Equator. As a result, the characteristics of inertial currents vary along the predominantly meridional west coast of North America. There are critical latitudes for inertial oscillations, where the local inertial frequency is close to the main tidal frequencies. For semidiurnal tidal harmonics, the critical latitude is located in the arctic seas, while for the diurnal frequency it is near 30° latitude (off northern Baja California in the study region). With the possible exception of internal Kelvin waves, freely propagating internal waves of frequency ω are not possible outside the frequency band between the Coriolis frequency, f, and the buoyancy frequency, N, i.e. $f < \omega \le N$ for internal waves (Cox, 1962; Garrett and Munk,1972). Therefore, internal waves of diurnal frequency cannot be generated poleward of the diurnal critical latitudes (such as the coast of Vancouver Island), and only semidiurnal tidally-generated internal waves can exist.

Kundu and Thomson (1990) found strong near-surface inertial currents off Vancouver Island's west coast during the summer and early fall of 1984 directly caused by the winds associated with propagating atmospheric fronts. Sub-surface inertial currents (at depths greater than 40 m) were not correlated with the local atmospheric forcing. Instead, the sub-surface inertial oscillations were suggested to be a superposition of the signals induced at the surface in remote regions and to have propagated to the region of observation along the ray-paths slightly inclined to the horizontal (characteristic of near-inertial oscillations). The tidal and inertial oscillations in long-term current meter records off Vancouver Island are explored in more detail in Section 4.1.

Synoptic, mesoscale, and sub-mesoscale variability

Between the main tidal frequencies and the annual frequency, mesoscale and sub-mesoscale features are responsible for the most of the variability in the coastal currents. The variability is caused by passage of atmospheric fronts and storms, wind-driven upwelling events, and instability in along-shore currents resulting in meanders, eddies, and filaments. These features are mostly irregular in time and produce "red" power spectra instead of sharp peaks typical for tidal and inertial currents. The mesoscale features usually produce steep gradients in physical and biological properties (Rebstock, 2003) and largely control the distribution of biologically rich waters in the coastal regions (Strub *et al.*, 1991; Dewey *et al.*, 1991). Estimates of the mass and nutrient flux due to tidal mixing, wind mixing, outflow out of the Juan de Fuca Strait, and upwelling in the region off the southwest coast of Vancouver Island by Crawford and Dewey (1989) indicate that coastal upwelling plays the most important role in supplying nutrients to the continental shelf. This result is substantiated by modelling studies by Foreman *et al.* (2008) and MacFadyen *et al.* (2008).

Anticyclonic eddies originating from baroclinic instability in the CUC and DC (Northeast Pacific Coastal Current) are observed from southern California to Vancouver Island and further along the Alaskan coast during the time of well-established along-shore currents in late summer, fall, and winter (Huyer *et al*., 1984; Lynn and Simpson, 1987, 1990; Kosro *et al*., 1991; Thomson and Gower, 1998; Chereskin *et al*., 2000; Kosro, 2002). Cyclonic eddies originating from instability in the CUC (Thomson, 1984) and wind-induced cyclonic eddies (Thomson and Gower, 1985), are observed on the Vancouver Island continental slope.

Seasonal changes

In the region of the North American west coast extending from approximately 36°N (central California) to 51°N (northern Vancouver Island), much of the seasonal variability is due to the seasonal reversal in the alongshore winds, which are poleward in winter and equatorward in summer (e.g. Hickey, 1979; Thomson *et al*., 1989; Thomson and Ware, 1996; Huyer, 2003). This atmospheric circulation pattern causes summer upwelling with its maximum usually in summer and early fall and winter downwelling which peaks in January – February. The upwelling strength is not steady within the season and not uniform along the coast. The strength of upwelling can vary substantially within the season according to the changing intensity of forcing alongshore winds. There are areas of stronger coastal upwelling as indicated by comparison of averaged summer and winter surface temperatures along the coast of California (Sverdrup *et al*., 1942). The upwelling also seems to be intensified south of coastal promontories (Reid *et al*., 1958).

Some current meter measurements of more than a year in duration off central California (Huyer *et al*., 1989; Collins *et al*., 1996c), Oregon (Kosro, 2002), and Washington (Werner and Hickey, 1983; Hickey, 1989a) indicate that the mainly year-round poleward CUC may, in fact, reverse its direction to equatorward during the winter season counter to the predominantly poleward flow at the surface. Model studies by Clarke and Van Gorder (1994) suggest that an equatorward undercurrent may be established as a result of poleward propagation of a thermocline depression from the tropical region during El Niño years. This is substantiated by shipborne ADCP observations at cross-shore sections off Oregon and northern California (Kosro, 2002). Kosro (2002) also notes that the equatorward undercurrent is a narrow feature occurring near steep bottom slopes and can be easily missed by geostrophic velocity estimates which frequently lack sufficient horizontal resolution to delineate the flow.

Interannual variability

The ocean-atmosphere system in the northeast Pacific varies at several dominant time scales. Ware and Thomson (2000) explored tree ring growth records on or near the North American west coast from Vancouver (British Columbia) to Visalia (central California) reflecting climatic conditions during past 400 years and identified dominant periods of variability. Specifically, the El Niño–Southern Oscillation (ENSO) cycle has a periodicity of 2-8 years, interdecadal oscillations have periods ranging from 20 to 40 years, and very low frequency multidecadal oscillations are observed at periods of 60-80 years. Similar dominant periods were identified in the time series of oceanic and atmospheric measurements on the British Columbia coast for the past century by Ware (1995).

A variety of large-scale processes is responsible for the variability at interannual scales. The equatorial phenomenon of ENSO is one of the most noticeable reasons for interannual changes in the California Current System (Chelton *et al*., 1982). Observations indicate that strong El Niño episodes (positive ENSO phase; e.g., 1982–3, 1997–8) are associated with elevated water temperature, high sea level, poleward near-surface current anomalies (Lynn, 1983; Huyer *et al*., 2002; Lynn and Bograd, 2002), and possibly with equatorward subsurface slope current anomalies (Clarke and Van Gorder, 1994) in the CCS. However, not all El Niño events affect the CCS, and not all interannual anomalies in the CCS are associated with El Niño (Simpson, 1984b; Ware and Thomson, 2000). According to Ware (1995), only 42% of strong and 25% of moderate El Niño events caused anomalies off the British Columbia coast. There is evidence of modulation of the El Niño signal by interdecadal (Gershunov and Barnett, 1998) and multidecadal (Rasmusson *et al*., 1995) cycles. La Niña episodes (negative ENSO phase) in the equatorial Pacific usually do not result in strong anomalies in the CCS (Smith *et al*., 2001).

The El Niño signal can propagate from the equatorial region to mid-latitudes through the ocean and through the atmosphere (Chavez *et al*., 2002). The oceanic El Niño signal usually arrives first. It propagates from the eastern equatorial Pacific northward and southward along the continental margins as coastally trapped Kelvin waves. Depressed isopycnals, raised sea level, and stronger poleward alongshore currents, carrying warm and more saline water to higher latitudes are all associated with the propagating Kelvin wave (Huyer and Smith, 1985). In the atmosphere, El Niño can cause a shift in the strength and position of dominant atmospheric systems, e.g. more intense Aleutian Low in winter (Harrison and Larkin, 1998) with corresponding stronger southerly winds and enhanced downwelling and poleward current along the coast (Hsieh *et al*., 1995; Huyer *et al*., 2002).

Bidecadal fluctuations are reflected in the Pacific Decadal Oscillation index (PDO) (Mantua *et al*., 1997). PDO is defined as the leading principal component of North Pacific monthly sea surface temperature (SST) variability. Positive (warm) phases and negative (cool) phases of the PDO interchange every 15-25 years with abrupt "regime shifts". Regime shifts are thought to have occurred in 1910 (Lluch-Belda *et al*., 2001), 1925, 1947 (Beamish *et al*., 1999; Overland *et al*., 1999), 1976–77 (Ebbesmeyer *et al*., 1991; Graham, 1994), and 1989 (Beamish *et al*., 1999; Overland *et al*., 1999; Hare and Mantua, 2000). A positive PDO means a stronger Aleutian Low, which effects the circulation in the zone of the CCS similar to El Niño episodes. A strong Aleutian Low is usually accompanied by an increase in frequency and strength of winter storms, and, as a consequence, stronger southerly along-shore winds which causes enhanced downwelling and advection of warmer surface waters to the CCS. Furthermore, a change in local heating can affect water temperature and thermocline depth in certain parts of the CCS (McLain *et al*., 1985). Overall, the large-scale processes that are responsible for the interannual variability in the CCS are all interrelated and it is difficult to delineate their individual effects (Rebstock, 2003).

An example of several large-scale processes acting in unison is the episode of Subarctic water intrusion into the CCS in 2002. Observations from Vancouver Island to southern California in the summer of 2002 revealed unusually cold waters in the surface layers in the CCS (Freeland *et al*., 2003; Bograd and Lynn, 2003). The anomaly was attributed to the increased presence of Subarctic water in the region. According to Freeland *et al.* (2003) and Murphree *et al.* (2003) a chain of large-scale atmosphere-ocean events was responsible for these cold anomalies in the California Current System. Huyer (2003) summarized their view: "There was anomalous Ekman transport of Subarctic water into the North Pacific Current during January-February 2002; the eastward transport of the North Pacific Current was enhanced in late winter; and there was anomalously strong upwelling along the west coast of North America in spring and summer. This sequence of large-scale processes led to a stronger California Current, and thus to enhanced Subarctic influence there".

Long-term trends

The considerable data that have been accumulated indicate that atmospheric forcing and resulting oceanic conditions along the North American west coast were not constant throughout the twentieth century. Based on surface atmospheric pressure data and corresponding geostrophic winds, Hsieh *et al*. (1995) concluded that the atmospheric forcing regime in the region changed around 1940. From 1899 to 1940, the data indicate a slight decline in summer upwelling off southern California and Baja California. Beginning around 1940, the alongshore winds increased in intensity which led to the intensification of downwelling along Alaska and northern BC and upwelling along Baja California, as well as to the increase in summer upwelling between southern BC and Baja California.

Rebstock (2003) reviews other studies that used historical hydrographic, meteorological, and microfossil data to investigate the long-term changes in the CCS. Trenberth and Hoar (1997) found that ENSO events, which strongly influence the CCS (McGowan, 1985; Murphree and Reynolds, 1995) have increased in frequency since the mid-1970s. Intensification of seasonal upwelling-favourable winds along the California coast have been identified by Bakun (1990) and Schwing and Mendelssohn (1997). Graham and Diaz (2001) report an increase in the frequency and intensity of winter cyclones and corresponding strong surface winds in the North Pacific over the last 50 years. The upper ocean temperatures increased off southern California over the same period of time (Roemmich, 1992; Roemmich and McGowan, 1995). This surface-intensified warming has led to an increase in water-column stratification and coincided with an increase in thermocline depth (Miller, 1996; McGowan *et al*., 2003). According to the evidence from microfossils presented by Weinheimer *et al*. (1999), the increase in thermocline depth and stratification that occurred in the 1940s and in 1960 may be a response to regime shifts during the PDO cycle and not a longer-term trend. Rebstock (2003) also notes that the increased stratification and thermocline depth could have had a large negative effect on primary production in the region if it had not been mitigated by the enriching effect of an increase in upwelling due to the increase in wind intensity.

2.3 Dynamical models of the poleward undercurrent

2.3.1. Forcing factors

Wind stress

Several forcing mechanisms have been proposed as possible sources of poleward undercurrents along eastern ocean boundaries. A number of analytical models suggest that a poleward undercurrent is an integral part of the coastal upwelling circulation. The concept was developed by Yoshida (1955), Yoshida and Mao (1967), Allen (1973), Pedlosky (1974, 1978a,b), McCreary (1981), Philander and Yoon (1982), Suginohara (1982), Wang (1982), Middleton and Leth (2004), and Choboter *et al*. (2005). These models use wind stress as the only forcing factor. Wind stress forcing can be localized or extend a considerable distance along the shore. Coastally trapped Kelvin waves generated by upwelling-favourable winds establish a poleward along-shore pressure gradient over time scales of tens of days from the wind onset. This poleward pressure gradient drives the undercurrent, which extends poleward beyond the area of the applied wind stress. Some of the energy of the along-shore currents leaks offshore in the form of westward propagating Rossby waves which weakens the equatorward surface jet and strengthens the poleward undercurrent (McCreary, 1981). According to the above analytical models, the stratification, the baroclinic alongshore pressure gradient, and the vertical mixing of heat and momentum are important factors in the generation of a coastal undercurrent.

Wind stress curl

According to the general theory of wind-driven ocean circulation developed by Sverdrup (1947), Stommel (1948), and Munk (1950), basin-scale flow in the upper 1000 m is determined by the curl of the wind stress over the ocean. Calculations based on the average zonal distribution of the wind stress produce two large gyres in the North Pacific: the Subpolar cyclonic and Subtropical anticyclonic gyres with a boundary between them at about 50°N, the latitude of maximum westward winds (Westerlies). The change of the Coriolis parameter (planetary vorticity) with latitude and the presence of western boundaries are responsible for the westward intensification of the flow, which combined with no-slip condition on the boundary explain the existence of strong and narrow Kuroshio and Oyashio (Thomson and Stewart, 1977). The eastern limbs of the gyres are, in contrast, sluggish and wide.

In the near-shore region along the eastern boundary of the North Pacific, the winds are predominantly meridional and the solution for meridional wind stress is applied to explain the main flow features in the region (Munk, 1950). The along-shore wind reaches its maximum some distance from the shore (about 100 - 200 km offshore) probably as a consequence of rough and elevated coastal terrain along the west coast of the North American continent (Nelson, 1977; Dorman and Winant, 1995; Oey, 1996; Wang, 1997). This offshore maximum in the meridional (equatorward) wind stress produces a zone of positive wind stress curl inshore of the axis of the maximum wind stress with an associated poleward flow and a zone of negative wind stress curl offshore of this axis with corresponding equatorward flow. This distribution in the wind stress curl leads to a depression in the sea surface in the zone of maximum wind stress and associated wind-forced upwelling in the offshore region (Chelton, 1982). This upwelling in offshore regions, caused by surface divergence of the surface current (Ekman pumping), is distinct from the coastal upwelling, which is usually confined within a distance of 20-50 km offshore and caused by the local wind stress and unrelated to the curl of the wind stress. The Sverdrup (1947) theory of wind currents (barotropic, steady state model with positive wind curl near the coastal boundary) reproduces the Davidson Current (Munk, 1950). But the currents in the region are generally neither barotropic nor steady, so the Sverdrup theory accounts at most for a part of the current variability in the CCS.

Hickey (1979) discusses wind curl-driven circulation off the west coast of North America. A correlation analysis between the second empirical orthogonal function (EOF) of dynamic height anomalies and the first EOF of wind stress curl anomalies off southern California provides observational evidence for the wind curl-driven circulation in the offshore region (Chelton, 1982). Cummins and Lagerloef (2004) also found that the ocean responds to the large-scale wind stress curl forcing with a lag of about two years. Time series of the wind stress curl calculated for a particular location near the coast do not, however, appear to be directly correlated with the local dynamic topography and the along-shore currents (Hickey, 1979; Bretschneider and McLain, 1983; McLain and Thomas, 1983).

Remote El Niño forcing

Clarke and Van Gorder (1994) used a numerical model with bottom friction, stratification, and realistic shelf and slope topography to study the response of the coastal ocean to the along-shore propagation of a disturbance of sea level and vertical thermal structure created in the eastern tropical Pacific as a result of El Niño forcing. They found that sea level disturbances should propagate poleward with velocities of 0.4-0.9 m/s, and isotherm disturbances should propagate at about 0.3-0.4 m/s, both in good agreement with the observations. They also found that an equatorward undercurrent is formed above the continental slope, within 500 m from the bottom, while a poleward current is formed in the surface layer. The velocity in the core of the equatorward undercurrent decreases from a maximum of 0.22 m/s at 20°N to 0.08 m/s at 60°N due to bottom friction.

Thermohaline forcing

Thermohaline forcing is another mechanism that can drive along-shore currents. If the water density in the surface layer of the ocean increases towards the pole, it results in a pressure field sloping downward in the poleward direction. This pressure field drives an onshore geostrophic current resulting in downwelling at the eastern ocean boundary. Associated with downwelling are a poleward surface current and an equatorward undercurrent (McCreary *et al*., 1986). This is a situation encountered along the west coast of Australia, where surface water cooling and increased salinity in the poleward direction are responsible for a density increase with latitude which creates a dynamic height drop towards the pole. Off the North American west coast, however, the cooler waters and lower salinity of the surface waters at higher latitudes oppose each other's effect on density, so that the meridional density gradient and corresponding thermohaline forcing likely do not play an important role in this region.

2.3.2. Modification of the flow

In addition to the forcing by the factors described above, several mechanisms exist which can modify the along-slope flow. These mechanisms are briefly reviewed below.

Interaction with bathymetric features

Cross-shelf canyons can strongly modify along-shore flow in a complex way. Upon encountering a canyon, a bottom shelf flow experiences vertical excursions and deviates in cross-shelf direction adjusting its vorticity balance in response to stretching and subsequent compression of the water column (Allen, 1996; Hickey, 1997; Allen *et al*., 2001). An upwelling favourable (equatorward) shelf-break flow (usually observed in the region in June-July) is re-directed up the canyon due to a geostrophically unbalanced upslope pressure gradient (Freeland and Denman, 1982). In the deep layer in a canyon, a cyclonic vortex is formed: upward tilting isopycnals create cyclonic vorticity and a downslope pressure gradient, which slows down and recirculates the initial upslope flow. Upwelling in a cross-slope-shelf canyon (Barkley Canyon) is shown to reach depths of 250 m (Allen *et al*., 2001).

A number of modelling and laboratory studies indicate that large-scale coastal promontories and underwater banks can lead to separation of along-slope flows and formation of filaments, meanders, and eddies (e.g. Bormans and Garrett 1989; Haidvogel *et al*., 1991; McCreary *et al*., 1991; Barth *et al*., 2000; Castelao and Barth, 2006). These features enhance the cross-shore mixing leading to important physical and biological implications.

Arrested Ekman layer or "Slippery slope" phenomenon

The flow along a sloping bottom, such as an along-shore flow above the continental slope, can be enhanced because of a frictional slowing ("arresting") of the bottom Ekman layer. Cross-slope advection of the density gradient in the bottom boundary layer leads to a buoyancy force which opposes the bottom Ekman transport and the Ekman transport is shut down over a certain time (MacCready and Rhines, 1993; Garrett *et al*., 1993; Chapman, 2002). If this time is sufficiently short, the advection of the density gradient and resulting tilt of the isopycnals lead to the thermal wind replacing turbulent stress as the mechanism opposing the along-slope flow. The result is much lower boundary stress than in the case of a simple horizontal bottom; i.e. the slope becomes "slippery". The conditions for such buoyancy shutdown are sufficiently strong stratification and steep slope.

As indicated by the above literature review, considerable knowledge has been accumulated about the CCS throughout its extent. Calculated geostrophic currents and ADCP surveys have provided snapshots of the along-shore circulation, while direct current measurements (a majority of them spanning not more than several months) have shown subseasonal variations of the flow. Time series of current measurements at least several years in duration are needed to establish reliable statistical characteristics of the flow (such as the seasonal cycle), to explore low-frequency changes, and to establish the relation of the currents to the forcing factors proposed by theoretical models. Such series are still rare on the west coast. The availability of a 20-year long series of direct current measurements at the northern extension of the CUC provides a unique opportunity to address these questions.

3. Data

3.1 Mooring and data description

The primary dataset used in the present work is moored current meter data collected as part of the La Perouse project led by the Local Dynamics and Processes Section at the Institute of Ocean Sciences (IOS) in Sidney, BC, Canada. The long-term mooring site, coded A1, is situated on the continental slope in 500 m of water, 60 km offshore from Ucluelet, British Columbia, on the west coast of Vancouver Island (Figure 3.1.1a). The segment of the data series used here spans the 20-year period from 1985 to 2004. During this period, the mooring was serviced regularly twice a year (in spring and fall) with a short time interval between successive deployments, thereby maintaining a nearly-continuous time series (Figure 3.1.2). The positions of individual deployments were typically located within 1 km of each other, although separations were as much as 10 km in some cases (Figure 3.1.1b). Each deployment usually had four instruments on the mooring line positioned at depths of 35, 100, 175, and 400 m (hereinafter referred to as *nominal depths*). The first in the series of deployments had only two instruments, at 35 and 175 m depth. The summer deployments of 2002 and 2003 had an additional instrument at 50 m depth. The actual instrument depth was usually within 20 m of the nominal depth, but in several cases differed by more than 20 m. This issue will be addressed in the next section in more detail.

The main deployment site is located above the northern slope of the bottom promontory between Loudoun Canyon and Barkley Canyon. Two parallel bathymetric cross-slope sections (one going through the main deployment site and the other through a location 3 km to the southeast from the main site) show that the poleward along-isobath flow below approximately 300 m depth is in the shadow of this "underwater headland" (Figure 3.1.1c). As discussed in Section 2.2, cross-slope canyons can alter or disrupt the along-shore current while facilitating cross-slope transport. It will be shown in section 4.1 that such flow features are observed in the current meter records at the nominal 400 m depth.

The instruments deployed – Aanderaa RCM4 current meters – are among the most widely used for current measurements in physical oceanography. The upper instrument in the winter deployment of 2000-2001 and the summer deployments of 2001 and 2002 was an Inter-Ocean S4 electromagnetic current meter. In the case of RCM4, the current is measured with a Savonius rotor (six axisymmetric, curved blades oriented normally to the direction of flow) which rotates under the influence of moving water. The average rate of rotation is recorded on a magnetic tape every 15 min (sampling rate can be adjusted) and direction is measured and recorded once at the end of each sampling interval with a built-in magnetic compass. Speed accuracy is 0.01 m/s or 2% of the actual speed whichever is greater. The bearing friction threshold of the rotor is about 0.02 m/s. This is considered a minimum speed that can be detected by RCM4 from the full rotor stop, however, if the rotor is already rotating, the instrument can measure slower speeds. The

Figure 3.1.1. (a) Location of current meter mooring A1, meteorological buoy 46206, tide gauges, and CTD stations; (b) location of individual deployments at Site A1; and (c) bathymetric cross-sections running parallel to each other through Site A1 and a site 3 km to the southeast along the general orientation of the isobath. Bathymetric data are courtesy of the Canadian Hydrographic Service.

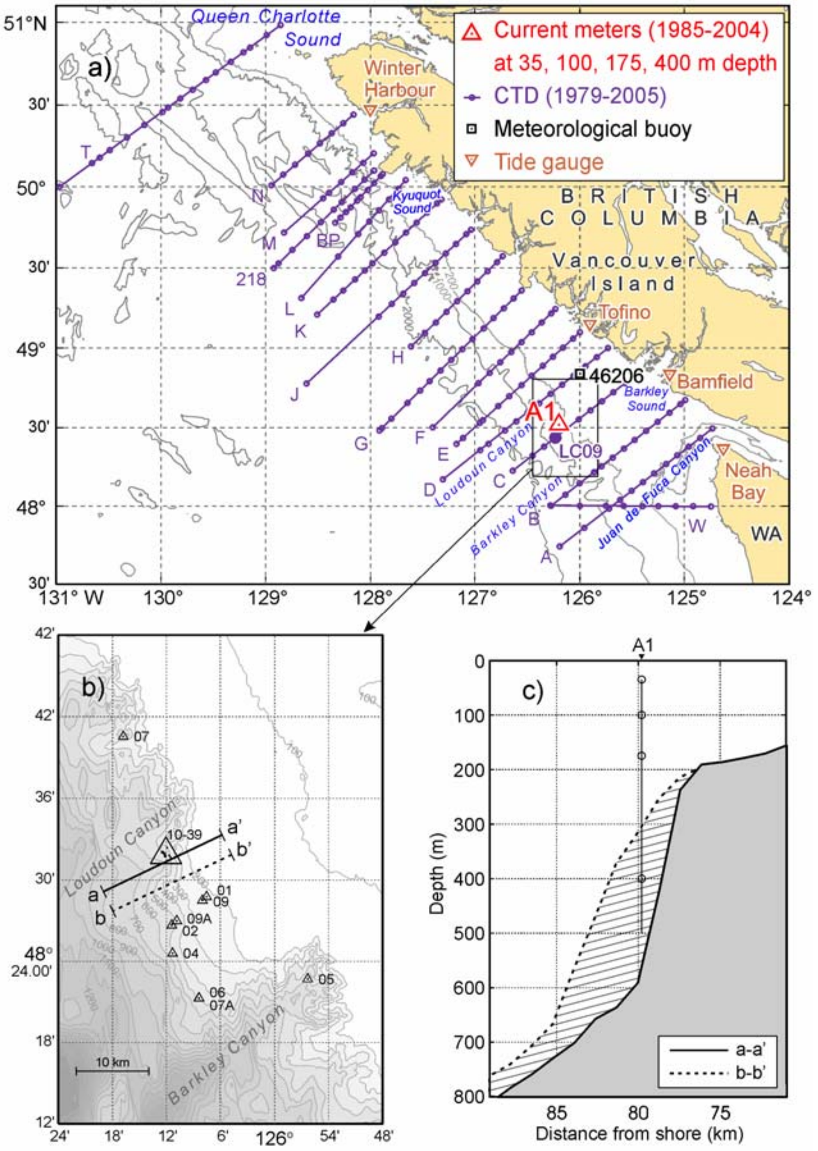

measured speed range can be adjusted according to the actual conditions in the region of deployment. The measured directions are accurate to 5° for speeds in the range of 0.05 to 1 m/s. For the Inter-Ocean S4 current meters, speed accuracy is 2% of reading with a minimum of 0.01 m/s, speed resolution is 0.001-0.002 m/s, compass accuracy is 2°, and compass resolution is 0.5° (Emery and Thomson, 2001). Figure 3.1.3 shows an example of a mooring assembly diagram as well as a general view of the RCM4 current meter.

Other data used in present study are the wind speed and direction measured at meteorological buoy 46206 moored 30 km offshore off Quisitis Point, sea level records at the Tofino and Bamfield tide gauges (obtained from the website of Marine Environmental Data Services (MEDS) of Fisheries and Oceans Canada), atmospheric pressure at sea level (provided by the NOAA-CIRES Climate Diagnostics Center, Boulder, Colorado, USA), and the bathymetry for the Pacific coast of Canada based on Canadian Hydrographic Service data. For the bathymetry data, the distance between data points is 0.5 - 0.7 km for the most of the shelf and slope. Distances become 0.5 km in the zonal direction and 4 km in the meridional direction in the deeper offshore regions.

3.2 Problems and limitations

While the data used in this work are generally of high quality, there are some problems which should be noted here. There are instances of missing data in the time series of current meter records throughout the observation period. Data are missing for periods of several hours to several days during the time the moorings were being serviced. Fish boats hitting a mooring were a frequent cause of lost or damaged equipment during the period of observation. The mooring at Site A1 was hit ten times during the 20 years of operation. In three cases, the mooring was dragged to a different location and depth but continued to record the data. The remaining “hit” deployments experienced total or partial losses of data. The data for the winter of 1988-89 were lost completely for this reason. In winter 1991-1992, the instrument at 175 m depth was flooded and 75% of the data were lost.

Figure 3.1.2. Time periods for current meter data for mooring site A1. The instrument depth was corrected according to the pressure records and comparison of RCM temperature records with nearby CTD temperature records (see text). The numbers near the time axis are the deployment identification numbers for the La Perouse project.

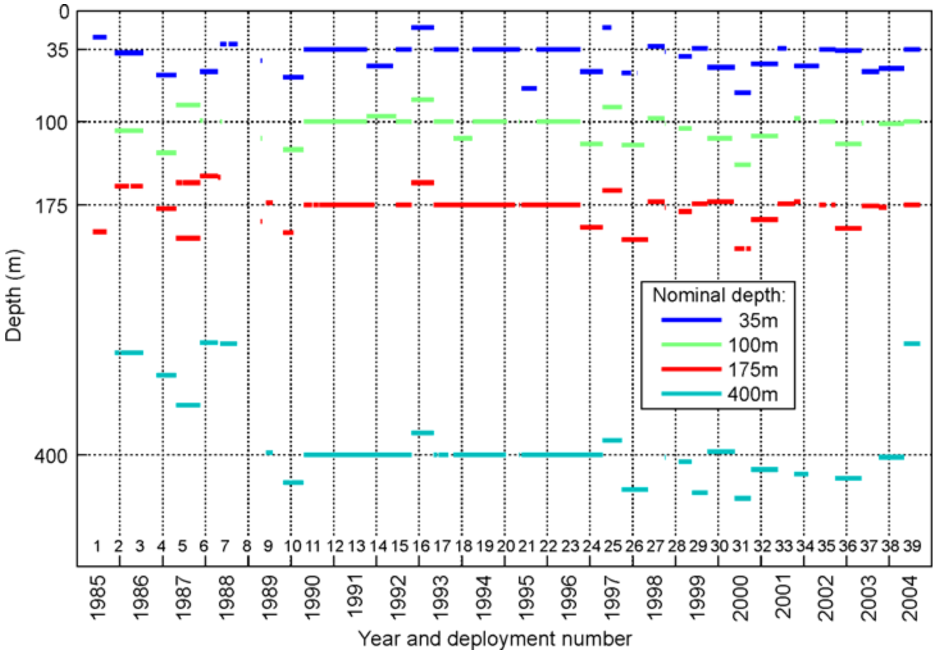

Examination of the instrument depth provided in the header of data files (hereinafter *recorded instrument depth*) and the pressure records for the corresponding instruments revealed discrepancies of up to tens of metres in about 30% of the data files where the pressure records were available. The comments in the data files indicate that the correction of instrument depth according to the pressure records was performed only for the data before the summer of 1989. The large number of depth discrepancies after the summer of 1989 suggests that certain recorded instrument depths may need correction.

The discrepancies between pressure records and recorded instrument depth can spring from erroneous pressure records, incorrect recorded instrument depth, or both. Errors in pressure records can result from incorrect calibration coefficients applied to the raw data, invalid coefficients recorded in calibration tables for the particular sensor, the calibration performed incorrectly, or from a malfunctioning sensor. The recorded instrument depth is provided from the mooring assembly diagram maintained by the Institute of Ocean Sciences and the bottom depth measured by the ship's sounder at the time of deployment of the mooring. Therefore, recorded instrument depth can be incorrect because the mooring was anchored at a different bottom depth than that measured from the ship or incorrect mooring assembly (e.g. use of a wrong connection line). The sounder depth can differ from the mooring depth because of the ship drift during mooring deployment; because of the mooring drift during its descent; and because the actual speed of sound in the water (which varies with water density, which is determined by pressure, temperature, and salinity) may be different from the assumed sound speed. Also, the sounder has a bottom "footprint" which, on the sloping bottom, may yield a depth which is different from the depth of the mooring by 5-10 m, or there may be small scale topographic features that will only be resolved by high resolution sonar surveys in the future (Richard Thomson, personal communication).

The coefficients applied for calibration of the pressure records (recorded in the data files) were checked and were found to correspond to the coefficients recorded in the calibration tables for the corresponding sensors. Other factors, which can lead to

Figure 3.1.3. Typical mooring assembly diagram (courtesy David Spear and Tomas Juhász, IOS) and a view of Aanderaa RCM4 current meter (from Emery and Thomson, 2001).

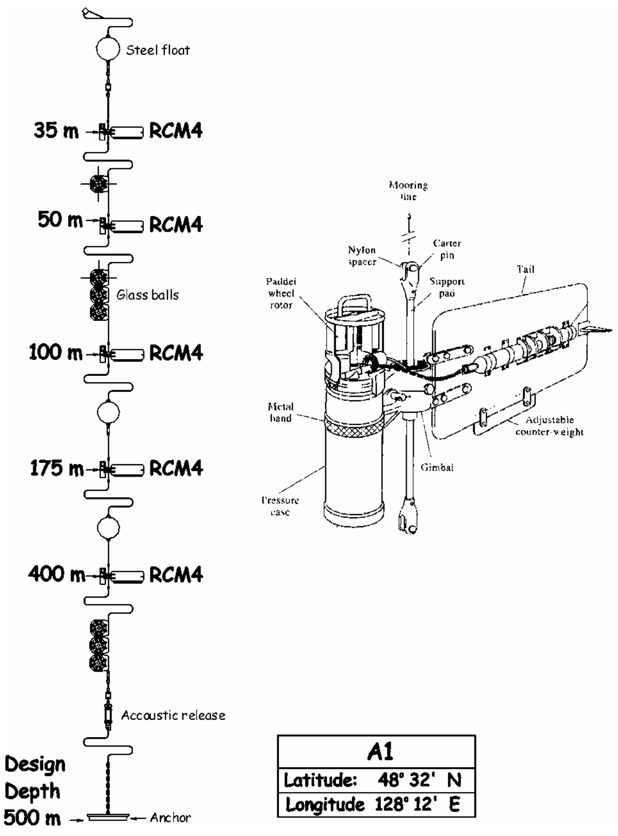

Figure 3.2.1. Pressure and temperature records used to determine the actual instrument depth for the La Perouse mooring #25 in the summer of 1997. Both the pressure and temperature records show that the actual instrument depth was approximately 10-15 m, as opposed to the originally recorded instrument depth of 32 m.

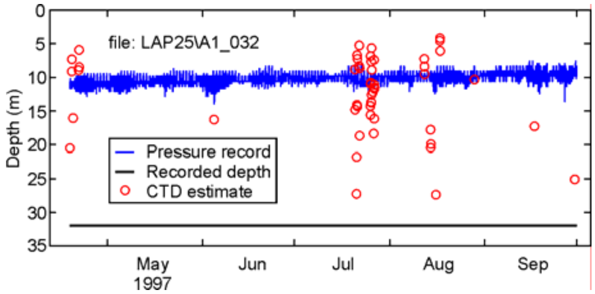

errors in pressure records or in recorded instrument depth, were not possible to check directly. In order to resolve the discrepancy problem, I used two indirect methods. First is the correspondence (where available) of two or more pressure records on the same deployment package. If discrepancies are the same for several instruments on the same mooring, then the pressure records are likely to be correct and the instrument depth adjusted according to the pressure records.

The second method uses temperature as an indicator of depth. The high quality of the temperature records obtained with the sensors installed on the current meters allows comparison with temperature measured by nearby CTD casts made during the period of the deployment. The thermocline with its large vertical temperature gradient gives relatively low uncertainty of the individual estimates. The main thermocline usually extends from 10 to 50 m depth in the region of deployment and is most pronounced from May to November. Therefore, it is for these depths and for this time of year that this method gives the most precise results. With the accuracy of temperature measurements of SBE 25 CTD profiler of ±0.002°C (Emery and Thomson, 2001), the accuracy of RCM4 thermistor of ±0.05°C (Aanderaa Instruments, 1983), and average vertical temperature gradient in the main thermocline of 0.1°C/m, the instrumental error of depth estimates derived from CTD temperature vs. RCM4 temperature is ±0.5 m. Between 80 and 500 m depth, the vertical temperature gradient is approximately 0.01 – 0.005°C/m producing an accuracy of ±5 – 10 m. Unfortunately, temporal and horizontal spatial variations of the thermal structure (e.g. sloping thermocline and internal tides) introduce additional uncertainties which are more difficult to evaluate. The internal tide problem has been dealt with by averaging over all CTD casts taken at a particular location over a particular deployment period. The thermocline slopes upward in the shoreward direction during summer coastal upwelling. To account for this thermocline slope, the selection of CTD stations for the comparison was restricted to stations whose bottom depth did not differ from the mooring depth by more than 200 m, which introduces an uncertainty of ±5m to the estimates taking typical values of bottom (6.2×10^{-2}) and thermocline (1.6×10^{-3}) slope in the area around Station A1. All CTD casts bounded by these isobaths and by a square 40' of longitude by 40' of latitude, with the centre at the actual mooring location, were selected. The temperature record at Site A1 at the time of each CTD cast was compared to the vertical temperature profile to determine the depth at which the instrument at A1 was located. The results of this test generally agree with the instrument depths evaluated using pressure records. An example of such test is shown in Figure 3.2.1. The low resolution of the salinity sensors used on RCM4 instruments prevented similar depth checks using salinity records.

Table 3.2.1. Actual instrument depth range for each nominal depth.

Nominal depth (m)	Actual depth range (m)	
	from	to
35	15	74
100	80	139
175	149	214
400	299	439

Appendix 1 shows the data files for which the instrument depth was corrected according to the two procedures described above. The maximum range of instrument depths for the period 1985 to 2004 for each nominal depth following the corrections is presented in Table 3.2.1.

Another problem with the current meter records is their

Figure 3.2.2. Rotary power spectra for a) Aanderaa RCM4 and b) InterOcean S4 current meter records for the upper instruments (nominal depth of 35 m) of A1 winter deployments of 1994-1995 and 2000-2001, respectively. Note the instrument-dependent roll-off structure for frequencies higher than 10 cpd and 16 cpd, respectively. Tidal peaks and inertial frequency (*f*) are marked by arrows.

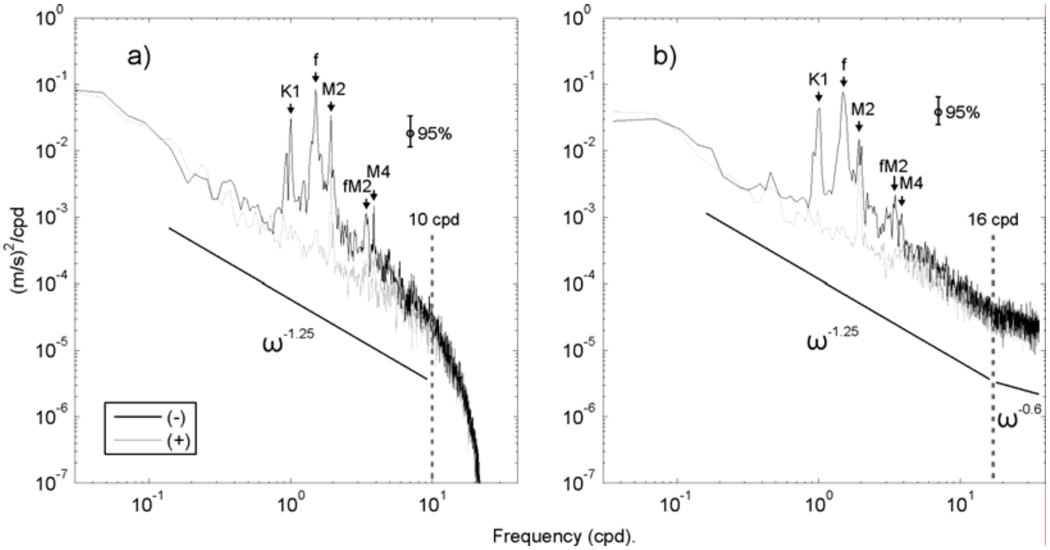

Figure 3.2.3. Examples of erroneous data: (a) unrealistically high speed values with straight lines indicating the instrument compass was stuck along certain directions; (b) absence of low speed values indicating incorrect speed measurement or rotor calibration, and a nearly isotropic flow field where it should have a certain prevailing direction; (c) the compass became stuck along certain directions; (d) a circle with small speed values indicating that some missing speed values were substituted with a value of 0.015 m/s (the value based on the sensitivity threshold for this type of current meter); (e) the plot of actual time between samples indicating periods of missing data.

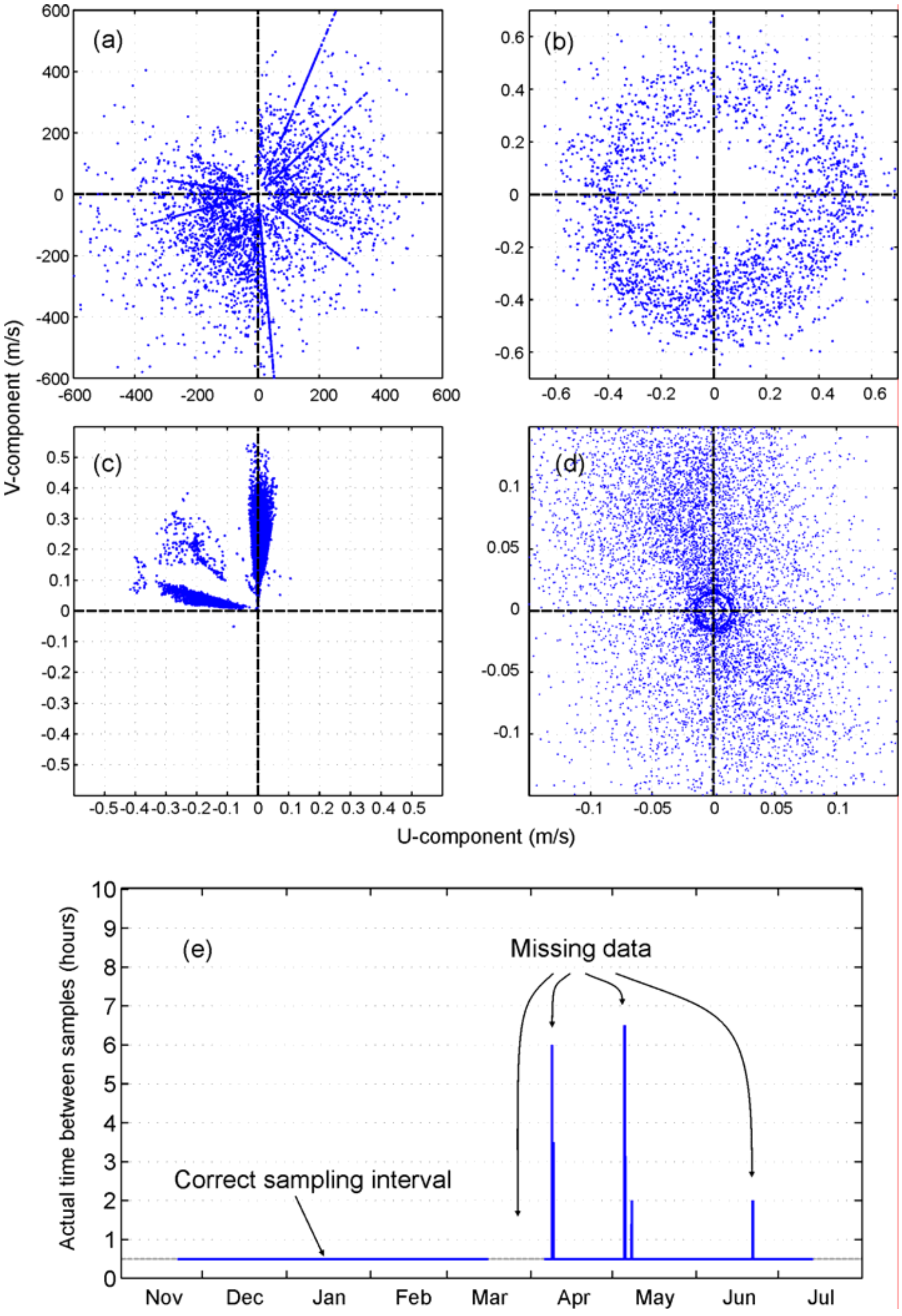

high-frequency content (*f*>10 cpd). There is a strong instrument-specific distortion of the signal at those frequencies. The power spectra of Aanderaa RCM4 current meter records show an abrupt decrease in power at frequencies higher than approximately 10 cpd (Figure 3.2.2a). This is a result of the built-in averaging mechanism for sampled values (Emery and Thomson, 2001). InterOcean S4 current meters, in contrast, produce very gradually sloping spectral background at frequencies higher than 16 cpd (Figure 3.2.2b). An abrupt change of the spectral background slope from $\omega^{-1.25}$ to $\omega^{-0.6}$ indicates that it is an instrument-specific feature: the level of the instrument noise for the InterOcean S4 instrument becomes comparable to the strength of the recorded signal. Therefore, neither instrument allows accurate investigation of the processes with frequencies higher than 10-16 cpd (periods of less than 1.5 – 2.4 hours).

The raw data downloaded from the current meters undergo a routine check by IOS personnel. First, the data are analysed by visual inspection of time series plots and histograms and edited as necessary. De-spiking is done automatically by data processing routines based on certain threshold criteria. Next, calibration formulae are applied to convert the instrument records to values in physical units. Finally, visual check and editing is done once again (Andrew Lee, IOS, pers. comm., 2005).

Figure 3.2.4. Power spectra of the time series of sea level at Bamfield showing aliasing of daily MEDS sea level data. Aliased peaks are marked by blue arrows. The 95% confidence interval is shown.

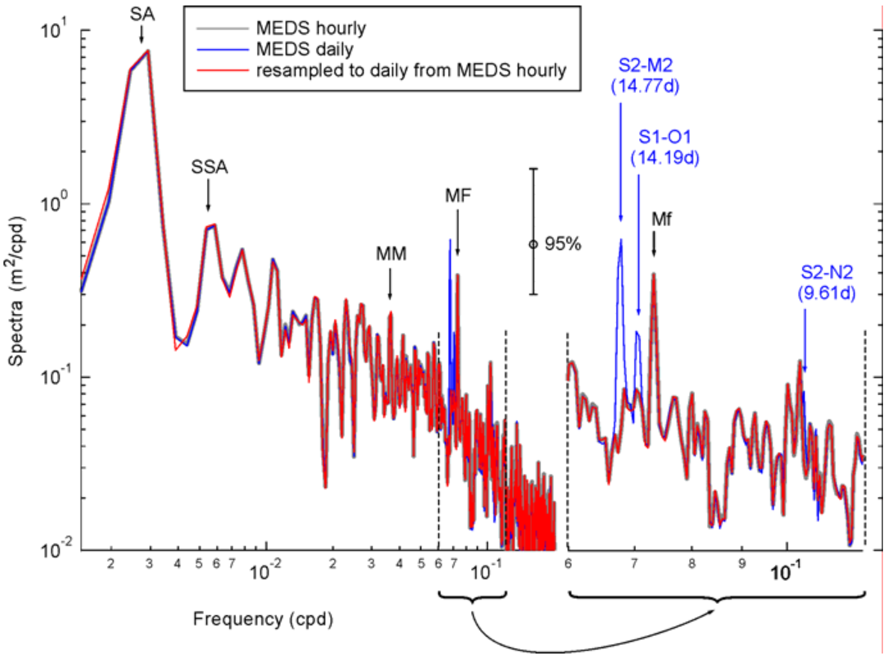

Many errors are removed from the data by the routine check. However, some of the less obvious errors can remain undetected after this check. Several simple tests were developed and applied to the time series to ensure more comprehensive error checks. The tests are based mainly on different methods of visualisation of vector time series. Each plotting method can help find errors undetectable in other types of plots. Some of the detected errors are illustrated in Figure 3.2.3. Scatter plots are useful in detection of errors in compass measurements even if the direction is erroneous only in part of the record. For data obtained close to the shore or to bathymetric features which possess a specific spatial orientation (e.g. continental slope, submarine canyon or ridge), a large difference between the direction of the major axis of variance and the direction of the local isobath may indicate a malfunctioning or incorrectly calibrated compass. A data quality check can also be a "by-product" of tidal analysis. Large residuals after removal of the tide, "unrealistic" ratios of the main tidal harmonic amplitudes, or abruptly changing phase for the harmonics with close frequencies indicate sampling problems (e.g. incorrect sampling times, wrong sampling rate, missing data values) or high noise levels in the record. Plots of actual time between samples versus time show if sampling is constant throughout the series and clearly indicate periods of missing data (Figure 3.2.3e). The variance of the currents obtained from power spectra may help in the detection of errors in rotor calibration. The frequency of the main tidal peaks in power spectra is a good reference for checking the instrument timing.

Power spectra plots also help detect possible aliasing problems. Aliasing is an effect produced by inadequate sampling of a signal when it becomes indistinguishable from a signal of a different frequency (the two signals are said to be aliases of one another). Frequency f is aliased with the frequencies determined by $f_M = nf_S \pm f$, where f_S is the sampling frequency and n is any positive integer (Emery and Thomson, 2001). Therefore, the distortion of power spectra due to aliasing can occur if the signal is undersampled or, in other words, the original signal has strong oscillations at frequencies higher than the Nyquist frequency $f_N = f_S/2$. For example, the energy of strong tidal oscillations in an oceanographic series folds back into lower frequencies when the series is resampled to daily values. Such an aliasing problem was detected in the daily sea level data obtained from the MEDS website. Figure 3.2.4 shows the spectra of hourly and daily sea level records for the Bamfield and Tofino stations. Spectra of the daily series reveal strong aliasing peaks at frequencies S1-O1, S2-M2, and S2-N2, where O1, M2, and N2 denote the frequencies of corresponding tidal components, S1 denotes the daily (sampling) frequency and S2 twice the daily frequency. The frequencies of aliasing peaks indicate that the daily sea level values were obtained without proper removal of the tidal signal and low-pass filtering. Two strong aliasing peaks (S2-M2 with period of 14.77 days and S1-O1 with period of 14.19 days) are close to a real fortnightly tidal peak Mf. As a result, the fortnightly cycle, naturally present in sea level oscillations, became artificially distorted to a significant extent in daily MEDS data. The red curve in Figure 3.2.4 shows the spectrum of the daily series which was resampled from the hourly series after subtraction of tides and low-pass filtering. As the figure shows, this spectrum precisely coincides with the spectrum of hourly series and does not possess aliasing peaks of daily MEDS series.

The data records derived by the quality checks outlined above, followed by elimination of erroneous data, are sufficient to perform statistical, spectral, and tidal analysis of the currents and to establish the scales of variability in the frequency band spanning the range from non-linear tidal oscillations to interannual variations.

4. General properties and statistics

4.1. Statistics and tidal analysis

General statistics

To establish seasonal differences in the general statistical properties of the current at Site A1 and wind at meteorological buoy 46206, the time series were divided in summer and winter parts separated by spring and fall oceanic transitions (see Section 2.1). The transition times were determined as the zero-crossing of band-filtered series of the current at 35 m depth with band edges (cutoff frequencies) corresponding to periods of 90

Figure 4.1.1. Wind and current direction histograms with mean speed for each compass direction for the summer, the winter, and the entire series based on daily values from meteorological buoy 46206 and four nominal depths of Mooring A1. The summer and winter are determined as periods between the spring and fall transitions (see the text). Red bars denote the percentage of speed measurements in each sector. The blue solid curve envelops mean speed values for each sector.

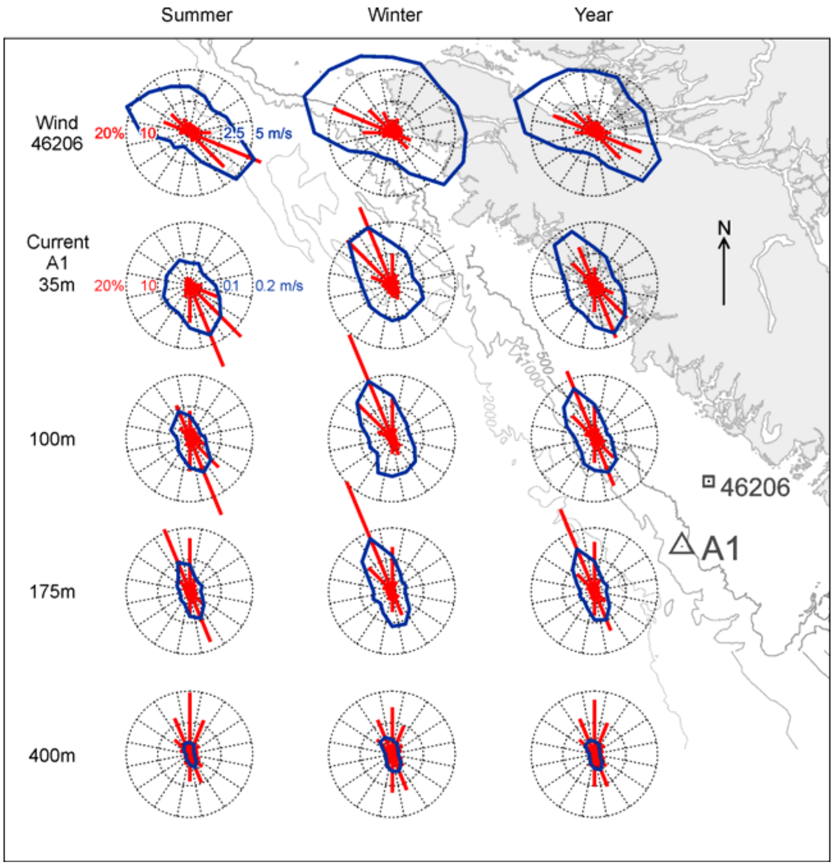

and 400 days since such band-filtered data contain mostly the annual signal with no individual synoptic events. Spring transition time fluctuated from the end of February to the end of April, but, in most cases, it occurred in the end of March or beginning of April. Fall transition time differed from year to year in a wider range (from the end of September to the middle of December), occurring mostly in October. The direction histograms of the daily wind and current vectors (Figure 4.1.1) emphasize seasonal differences in the near-surface wind and underlying flow in the deployment region. Both the wind and near-surface current reverse direction from equatorward in summer to poleward in winter. The direction of the most frequent flow and the direction of the strongest flow for the examined series generally coincide (with two notable exceptions considered below). The wind is aligned with the shore while the flow is aligned with the general orientation of the shelf break for the near-surface current. The principal axis of the near-surface current variance is directed 335° clockwise from true north. This direction is used throughout the text as the alongshore direction whenever the current meter data are rotated to the alongshore and cross-shore coordinate frame. The alongshore direction for the wind is 305° from true north, which is also chosen based on the direction of the principal axis of variance. The principal axis of current variance rotates clockwise with depth aligning with the local bathymetric feature in deeper layers. Below the surface, the current is less disturbed by surface eddies and synoptic activity and becomes more focused in one directional sector.

One case for which the direction of most frequent flow does not coincide with the direction of strongest flow is the mean annual near-surface current. The strongest flow here is poleward and occurs during the winter, caused by strong winter winds. However, the equatorward flow is more frequent, giving rise to yearly averaged equatorward transport (Figure 4.1.2). The other case is the summer flow at 175 m depth. The poleward and the equatorward flow at this depth are equally strong but poleward flow is twice as frequent. Therefore, the net current at 175 m depth is poleward both in summer and in winter (Figure 4.1.2). Summarising the alongshore flow features at Site A1, there is a seasonally reversing flow at 35 and 100 m depth and year-round poleward flow at 175 m and 400 m depth. The yearly averaged flow is equatorward at 35 m depth and poleward in the deeper layers. All these flow characteristics are also reflected quite well in the progressive vector diagrams in Figure 4.1.3. The plots are drawn using the original 30-min current meter data. Although there are periods of missing data, the total number of data points in each month (shown in monthly histograms for each nominal depth) does not differ dramatically thus preserving the overall picture of the flow.

In the cross-shore direction, the onshore wind is stronger than the offshore wind throughout the year (Figure 4.1.1). In contrast, the mean summer onshore near-surface current is less than its offshore counterpart by about 0.05 m/s. The situation is typical of a summer upwelling circulation. The winter downwelling onshore flow is not detectable from the direction histograms, probably because it is masked by the intensive synoptic activity in winter.

Tidal and inertial currents

Tidal variations in sea level and currents are one of the most energetic processes in the sea, particularly in the nearshore zone. Accurate tidal analysis is important for revealing the characteristics of these motions. It is also used to remove highly

Figure 4.1.2. Mean wind and current vectors for the winter, the summer, and the entire series based on daily values from meteorological buoy 46206 and different depths of Mooring A1. The numbers near the arrow tips indicate observation depth and mean speed (×10^{-2} m/s). The yearly vectors are exaggerated with respect to the seasonal vectors by a factor of two for better visualization.

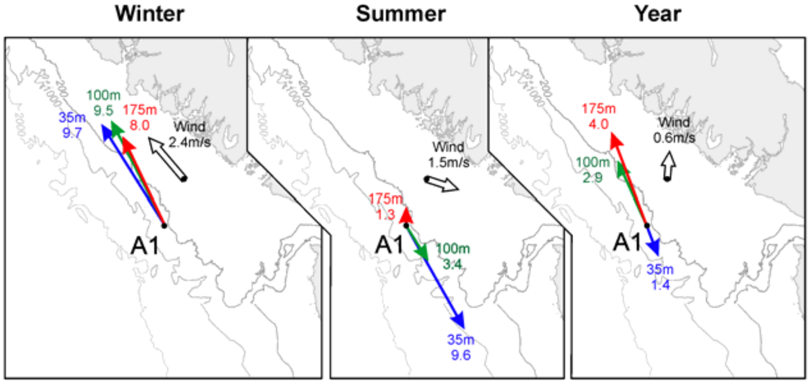

energetic tidal motions from the records for the purpose of investigation of low-frequency processes.

In the shelf-slope region off Vancouver Island, tidal currents change from predominantly diurnal on the shelf to predominantly semidiurnal on the outer slope (Crawford and Thomson, 1982). At Site A1, located on the upper slope, close to the shelf break, the tides are of mixed type with diurnal and semidiurnal currents of approximately the same amplitude (Figure 4.2.1). The local inertial frequency at Site A1 (f = 1.503 cpd) lies midway between the diurnal and semidiurnal frequencies so that inertial currents are distinct from both diurnal and semidiurnal tidal currents. The fact that the inertial frequency is higher than the diurnal but lower than the semidiurnal also implies that fundamentally different processes are involved in the formation of diurnal and semidiurnal currents in the region. Diurnal currents are mainly barotropic and comprised of a significant continental shelf wave component (Crawford and Thomson, 1982); semidiurnal currents have a significant baroclinic component as a consequence of strong internal wave generation at the shelf break (Drakopoulos and Marsden, 1993; Cummins *et al*., 2001).

The harmonic analysis of tidal currents at Site A1 was performed using the least squares method (e.g. Pugh, 1987; Emery and Thomson, 2001) for a set of 16 tidal constituents with two additional constituents (K2 and P1) derived by the Zetler correction procedure (Zetler *et al*., 1965). The correction procedure is used when several close tidal frequencies are not adequately resolved for the series of given length. In this case, theoretical ratios of the tidal constituent amplitudes are used to correct for possible discrepancies with calculated amplitudes. Two software tools were used. One is a Matlab version of Foreman's IOS tidal package (Foreman, 1978; Pawlowicz *et al*., 2002) the other is a Fortran tool (LSM) written by A. Rabinovich of the Tsunami Research Center (Institute of Oceanology, Russian Academy of Science, Moscow). These two tools were compared (Appendix B) and gave very similar results. Based on the test run, the routines can be considered interchangeable for the purposes of the analysis of major tidal constituents and de-tiding. The results of the analysis are presented in Figure 4.1.4 in the form of tidal ellipses for the major semidiurnal (M2) and diurnal (K1 and O1) tidal constituents.

M2 currents at the two upper levels (35 and 100 m) vary considerably from year to year in their orientation, phase, and sense of rotation. This is especially true for the 100 m depth. This indicates the presence of strong incoherent (not phase-locked with tides) baroclinic waves of semidiurnal frequency. The amplitude of semidiurnal currents is lowest at 100 m depth (Figure 4.1.5) with the M2 current usually the weakest (0.02-0.04 m/s) at this depth. Current meters at 175 m depth show high

Figure 4.1.3. Progressive vector diagrams based on all available current meter data at Site A1 for the period 1985 - 2004. The number of values used is provided in the monthly histograms for each depth.

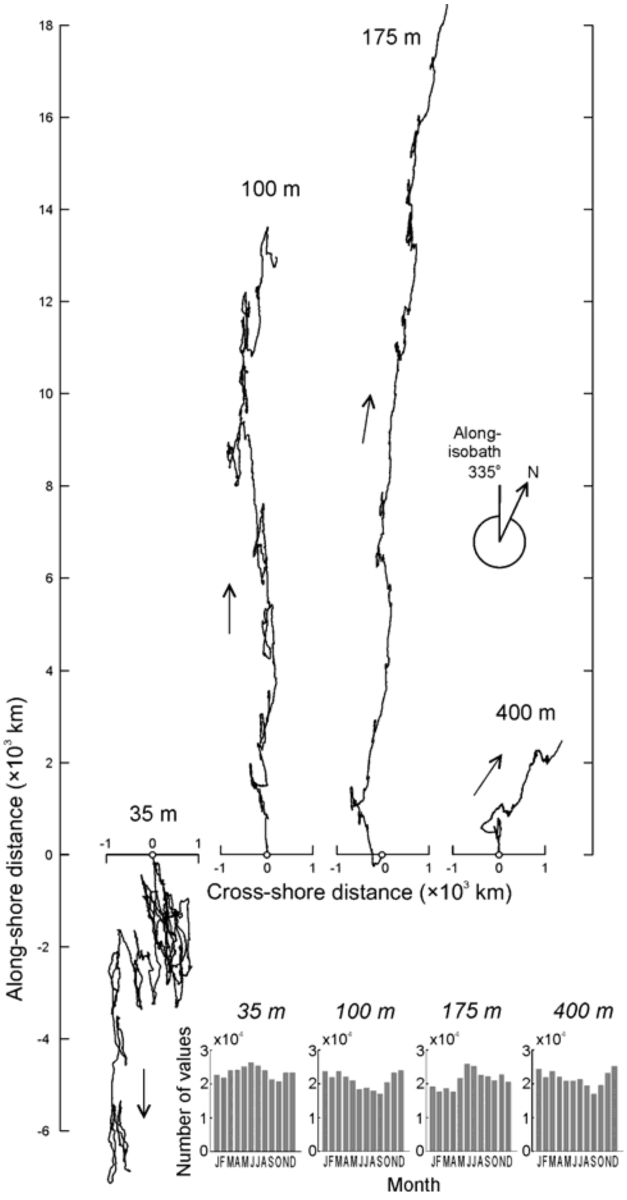

Figure 4.1.4. Tidal ellipses with phases for the K1, O1, and M2 tidal constituents and amplitude of the inertial currents calculated for each deployment at Site A1. Red denotes clockwise rotation and blue denotes counter-clockwise rotation. Only the series longer than 70 days were considered. Note the different scale for the inertial currents.

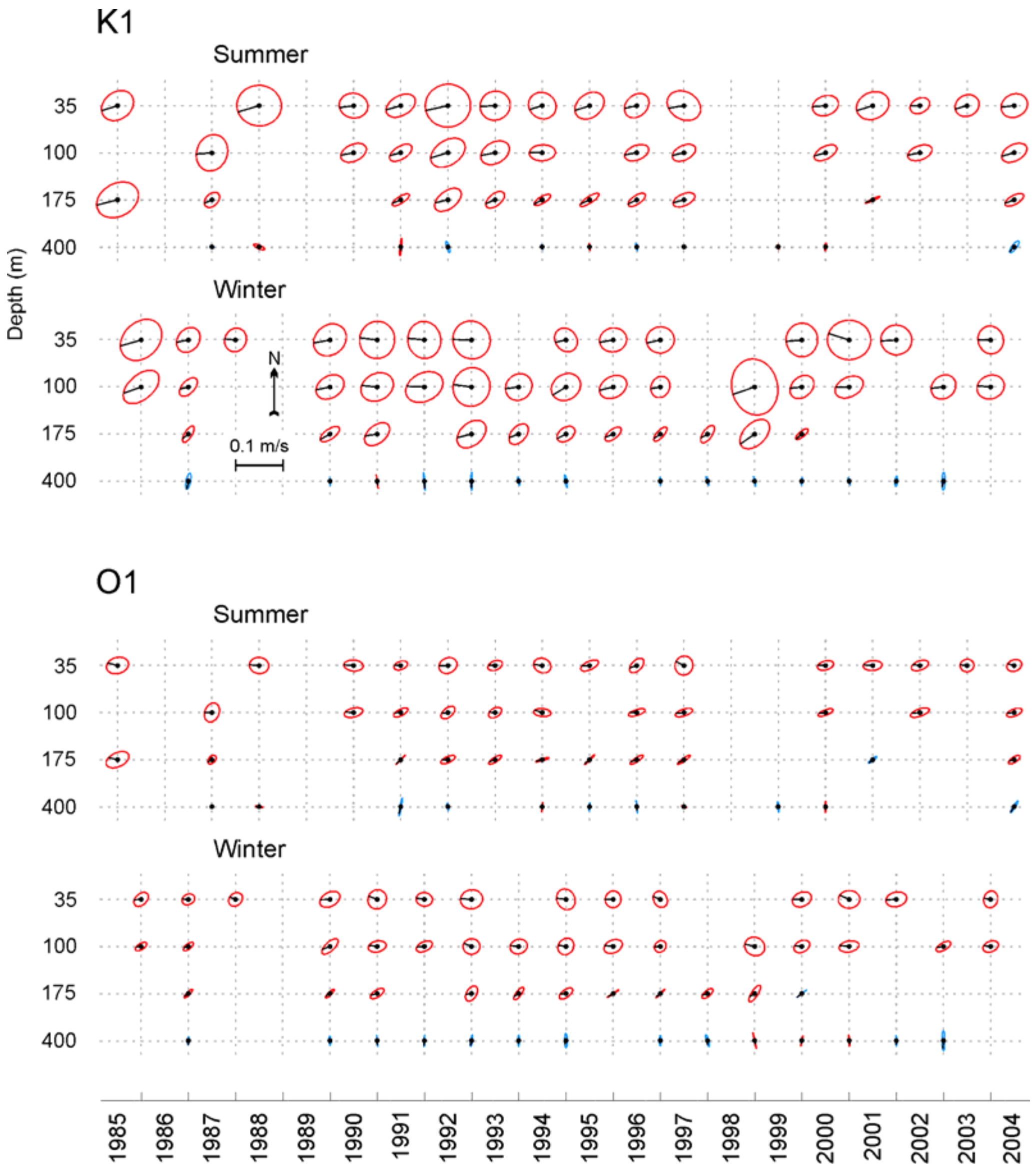

consistency in M2 current amplitude, phase, orientation, and sense of rotation, indicating a large coherent (phase-locked with tides) part in semidiurnal band at this depth which allows for more consistent estimates. M2 currents here are stronger, reaching 0.05-0.06 m/s along the semi-major ellipse axis, oriented predominantly along the shelf break, and rotate counter-clockwise for all deployments. At the depth of the deepest instrument (400 m), the along-shelf flow is likely modified by Loudoun Canyon (Figure 3.1.1). As a result, M2 currents are weak and do not exceed 0.02-0.03 m/s. The ellipses are very elongated and oriented along the axis of the canyon, in the cross-shelf direction. The rotation is predominantly clockwise.

The currents at tidal frequencies recorded during the 1985 summer deployment (first in the series) are anomalously strong, particularly for the M2 constituent (twofold increase in comparison to the rest of the deployments) at the 200 m instrument, 20 m above the bottom. The different character of currents in this case is a consequence of the mooring location. The mooring was located at the shelf break (Figure 3.1.1c). M2 currents are particularly strong in regions of rapidly varying bottom topography and intensive generation of internal waves at the shelf break (Torgrimson and Hickey, 1979). The currents at tidal frequencies recorded by several other deployments in the series, which were deployed at greater distances from the main mooring site, but approximately at the same bottom depth (e.g. deployments 4, 6, and 7: winter ’86-87, winter ’87-88, and summer ’88), does not differ as markedly from the rest of the deployments. This case stresses the fact that the flow regime changes over shorter spatial scales in the cross-isobath direction than in the along-isobath direction.

Diurnal tidal currents in the region of Vancouver Island are strongly influenced by continental shelf waves (Crawford and Thomson, 1982; 1984). These waves are forced by the diurnal tidal flow. Deviation from the equilibrium potential vorticity due to changing bottom topography provides the restoring force. Continental shelf waves are barotropic planetary waves that can exist only at subinertial frequencies (LeBlond and Mysak, 1978); therefore, they do not influence semidiurnal currents and can have diurnal frequency only in the regions poleward of 30^{o} latitude, where the inertial frequency exceeds the diurnal frequency. As a result, the existence of continental shelf waves of diurnal frequency is restricted to mid- to high latitudes. Off the

Figure 4.1.4. (continued)

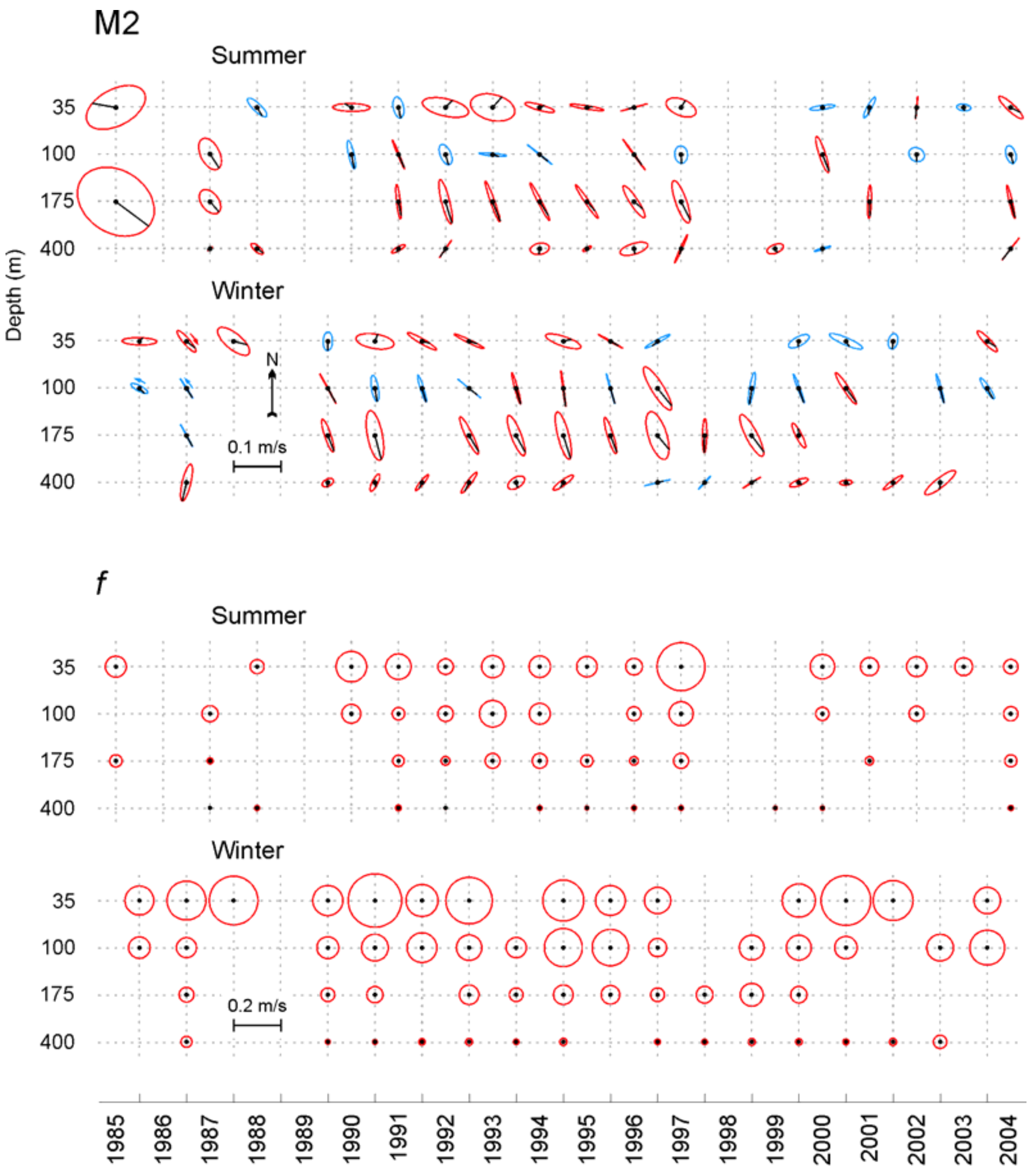

west coast of North America, they were observed only off the Vancouver Island coast and the northern end of the Washington coast (Thomson and Crawford, 1982; Foreman and Thomson, 1997; Cummins *et al.*, 2000). Continental shelf waves are almost horizontally non-divergent and manifest mostly in currents rather than in sea level variations. For a typical depth profile off Vancouver Island, first mode barotropic continental shelf waves have maximum along-shore current amplitude near the coast and maximum cross-shore current amplitude near the shelf break. As a result, in the near-shore region, amplification of diurnal tidal currents due to the presence of continental shelf waves can be five- to tenfold, compared to the region of deep ocean farther offshore (Thomson and Crawford, 1982). Near the shelf break, diurnal currents are expected to be strong, quasi-barotropic with largely clockwise rotation and to have a significant cross-shelf component. In accordance with theory, the observed K1 and O1 currents have almost circular clockwise orbits or elliptical orbits oriented mostly cross-shore with the amplitudes comparable or exceeding those for M2. These features of diurnal currents indicate the presence of coastal trapped waves (Crawford and Thomson, 1984). At 175 m depth, the diurnal currents are weaker than at the upper two levels. The change in speed of diurnal currents with depth indicates that they are influenced by stratification, acquiring a baroclinic component. At all depths, K1 and O1 show very similar features with the exception of amplitude. The ratio of their amplitudes, however, as well as the phase is consistent throughout the observational period. Typical K1 currents are 0.04 to 0.05 m/s at 35m depth and 0.02 to 0.03 m/s at 175 m depth, while corresponding O1 currents are roughly half of that strength. The speed in winter is usually 20% higher than in summer. This is likely caused by changes in modal structure of continental shelf waves due to seasonally varying stratification. At 400 m depth, K1 and O1 currents are very weak with predominantly counter-clockwise rotation.

Figure 4.1.5 shows the vertical distribution of the counter-clockwise and clockwise components of M2 and K1 currents at Site A1. The strength of the counter-clockwise component for both M2 and K1 changes little with depth, having a small local maximum at 175 m depth. This reflects predominantly barotropic character of the counter-clockwise component. The amplitude of the clockwise rotating vector for K1 always exceeds that of the counter-clockwise rotating vector at depths shallower than 300 m. Below this depth, both components have a similar amplitude. The clockwise amplitude of K1 has its maximum at the surface and decreases with depth with maximum rate of decrease at pycnocline depth. The clockwise component of M2 has two local maxima, at the surface and at 175 m depth. At 100 m depth, it has a local minimum and can be weaker than the

Figure 4.1.5. Vertical distribution of the amplitudes of the positively and negatively rotating vectors for the main semi-diurnal (M2) and diurnal (K1) tidal harmonics. '+' and 'o' symbols denote values calculated for individual deployments. Solid lines are corresponding piecewise linear fits with break points at the nominal instrument depths. Anomalously large M2 values for the summer of 1985 are ignored.

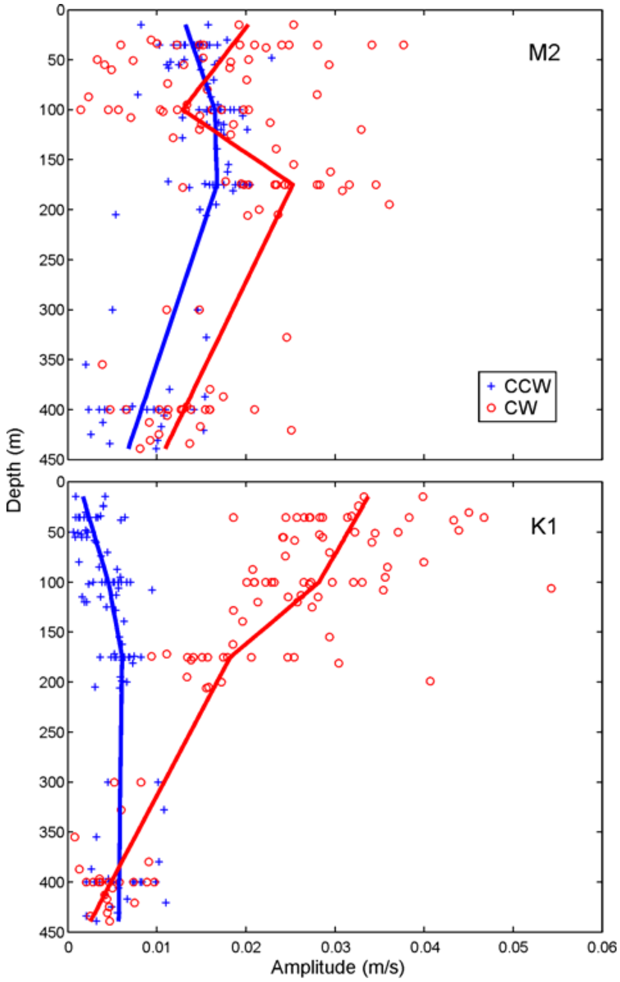

counter-clockwise component at this depth. This shape of the vertical profile of the clockwise M2 component reflects the modal structure of internal waves in the region.

The speed of inertial currents in Figure 4.1.4 was evaluated using rotary spectra (Section 4.2). All energy of the clockwise oscillations in the near-inertial band (1.22 to 1.72 cpd) was assumed to be associated with inertial currents. The square root of the spectral energy integrated over the near-inertial band was taken as an estimate of the speed of the inertial current. Inertial oscillations are surface generated currents forced by the wind fields associated with passing atmospheric fronts (Thomson and Huggett, 1981; D'Asaro, 1985; Kundu and Thomson, 1990). Detailed investigation of seasonal average energy in the near-inertial band will be done in Section 4.2. Here, I only outline major features. As expected, the strength of the observed inertial currents decreases with depth. Winter brings strong winds to the region. As a consequence, inertial currents in winter are about twice as strong as in summer for the near-surface layer. This ratio decreases with depth. The summer of 1997 (a major El Niño year) has anomalously strong inertial currents (more than twice the average summer value). However, wind observations at Station 46206 do not show extraordinary atmospheric activity in the region during that summer. The vertical location of the instruments during the summer 1997 deployment may have also been a factor in the anomalously strong inertial currents. The pressure sensor at the upper instrument of this deployment shows values in the range from 8 to 12 dbar, indicative of the actual instrument depth, which is much closer to the surface than for the rest of the deployments.

4.2. Spectral analysis

The relative importance of processes determining the circulation of the shelf-slope region changes rapidly in both the cross-shore and along-shore directions. The A1 current meter records enable us to establish the contribution the various processes make to the dynamics of the upper slope region off the southern Vancouver Island. Each frequency band of oceanic variability has its own specific characteristics. Spectral analysis allows estimation of the energy as a function of frequency and, consequently, the energy associated with the different types of processes. Using spectral analysis for A1 current meter records, I investigate variability of oceanic currents in different frequency bands with particular focus on tidal, inertial, synoptic, and seasonal variability. Vertical distribution of the spectral energy is evaluated by exploring the series at each nominal depth. Finally, I calculate the broad-band spectra of the combined series spanning the whole period of observation, which allows investigation of low-frequency current oscillations.

Rotary spectral analysis (Gonella, 1972; Mooers, 1973; Emery and Thomson, 2001) is used to examine the current series at station A1. This vector series method is based on the idea of decomposing vector oscillations into negatively (clockwise) and positively (counter-clockwise) rotating vectors as opposed to, say, north-south and east-west decomposition. The main advantage of rotary spectral analysis is that obtained properties are coordinate-independent; i.e. remain the same under rotation of the original Cartesian coordinate system. This approach allows a description of the vector characteristics of the various processes; specifically the orientation of the current ellipse and the sense of rotation. Suppose we have a vector quantity expressed in terms of components $u(t)$ and $v(t)$, then the autospectra of these components are (Gonella, 1972):

$$S_{uu}(\omega) = (2/T) < U(\omega)\, U^*(\omega) >$$

$$S_{vv}(\omega) = (2/T) < V(\omega)\, V^*(\omega) >,$$

and the cross-spectrum is:

$$S_{uv}(\omega) = (2/T) < U(\omega)\, V^*(\omega) >, \qquad 0 \le \omega \le 2\pi f_N$$

where $U(\omega)$ and $V(\omega)$ are the Fourier transforms of the $u(t)$ and $v(t)$ components respectively, * denotes the complex conjugate, $f_N = 1/(2\Delta t)$ is the Nyquist frequency, and Δt is the sampling interval (Emery and Thomson, 2001). I will use the angular frequency ω instead of $2\pi f$ here because symbol 'f' is reserved for the inertial frequency. The Fourier transform is defined as:

$$X(\omega) = \int_0^T x(t) e^{-i\omega t} dt\,,$$

or, in the discrete domain for the time series $x_n = x(n\Delta t)$ of length N, where $n = 1,2,3,\ldots,N$:

$$X_k = \Delta t \sum_{n=1}^{N} x_n e^{-i2\pi kn/N}, k = 1,2,3,\ldots N.$$

Then the positive (counter-clockwise rotating) and negative (clockwise rotating) components of the rotary spectra are defined as:

$$S^-(\omega) = 1/2\, [S_{uu}(\omega) + S_{vv}(\omega) - 2Q_{uv}(\omega)],$$

Figure 4.2.1. Average rotary spectra of A1 currents for summer and winter deployments (1985 – 2005).

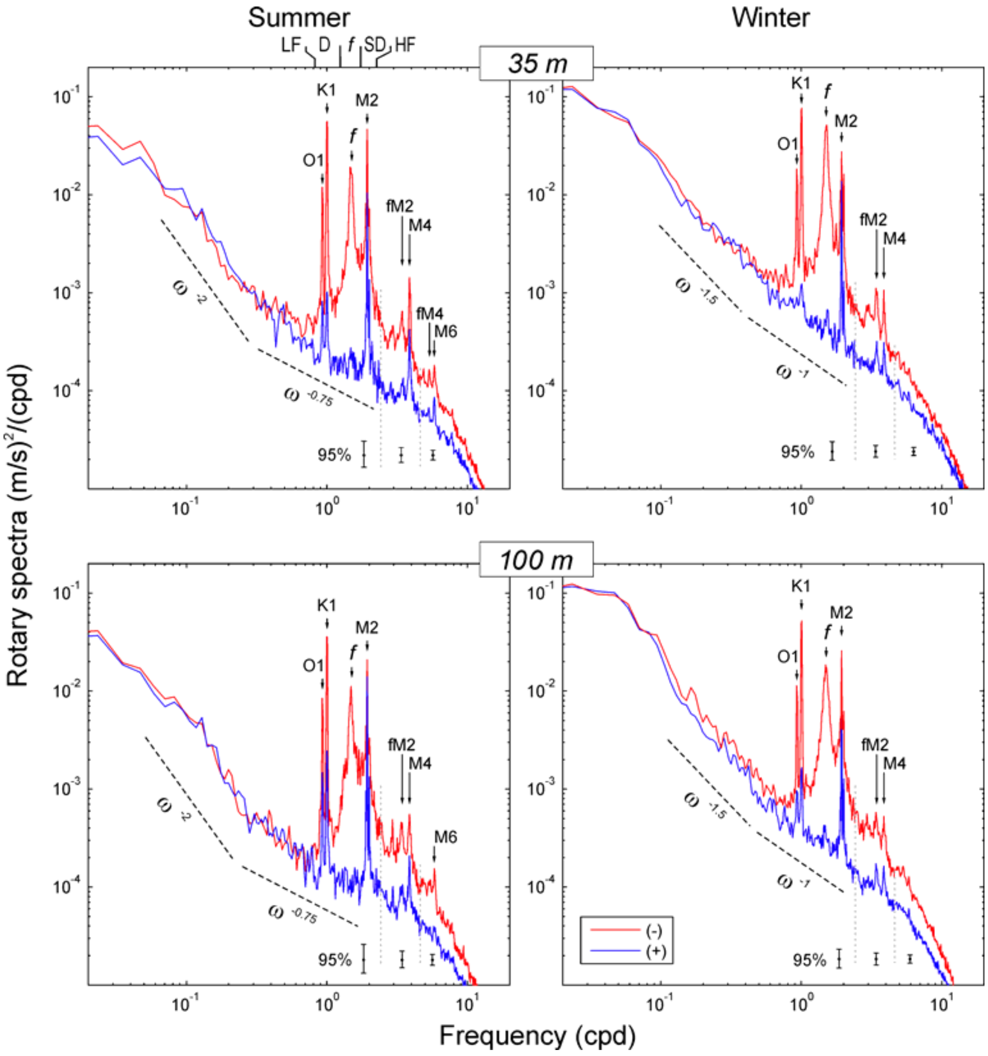

$$S^{+}(\omega) = 1/2\,[S_{uu}(\omega) + S_{vv}(\omega) + 2Q_{uv}(\omega)],$$

where $Q_{uv}(\omega)$ is the quadrature spectrum of the components u and v:

$$Q_{uv}(\omega) = -\mathrm{Im}\{S_{uv}(\omega)\}.$$

According to the above definition, S^{-} and S^{+} satisfy the condition:

$$S^{-}(\omega) + S^{+}(\omega) = S_{total}(\omega),$$

where $S_{total}(\omega) \equiv S_{uu}(\omega) + S_{vv}(\omega)$ (Emery and Thomson, 2001).

All A1 current meter series for the period 1985-2004 were used in the analysis except for the records deemed to be erroneous (specified in Section 3.1). The summer 1985 mooring, which was deployed at a much shallower site (the shelf break) than the rest of the deployments, recorded much stronger semidiurnal currents at all depths and considerably stronger diurnal currents at 175 m depth and will also be excluded from the analysis as non-representative of the average flow.

First, I explore the properties of the summer and winter currents at station A1 at various depths. I consider the integral properties, rather than specific features of individual deployments. For this purpose, I select only sufficiently long records (> 1.5 times the length of the spectral window, which is specified later) where missing data comprise not more than 3% of the record length. Since some of the gaps in the series could be quite extensive, I took a conservative approach and filled the missing data with the mean value for the record. Each winter deployment usually spans a wider period than that defined by the spring and fall oceanic transitions for the corresponding year, but, in order to use the maximum available data, the series were not truncated, so winter series may include data pertaining to the summer season, if summer is defined strictly as the period between the spring and fall oceanic transitions.

Seasonally averaged rotary spectra for each nominal depth are presented in Figure 4.2.1. To suppress high-frequency noise, shorter spectral windows were used for the high-frequency bands, which gives more degrees of freedom. For frequencies less than 2.4 cpd, a spectral window of 85 days was used; for frequencies from 2.4 to 4.6 cpd the window length was 43 days; for higher frequencies, a 21-day window was used. The corresponding 95% confidence intervals are shown in the plots (Figure 4.2.1). The spectra have a background that slopes down from low to high frequencies (red spectra). The power law for the spectral slope (background falloff rate) from 0.1 to 0.3 cpd is ω^{-2} in summer and $\omega^{-1.5}$ in winter. At higher frequencies it is $\omega^{-0.75}$ in summer and ω^{-1} in winter.

The tidal peaks (both diurnal and semidiurnal) and the inertial peak stand out above the background well above the 95% confidence interval. Spectral energy at the K1 frequency is slightly larger than at the M2 frequency at 35 and 100 m depth, and becomes less than the M2 peak at 175 m depth and deeper.

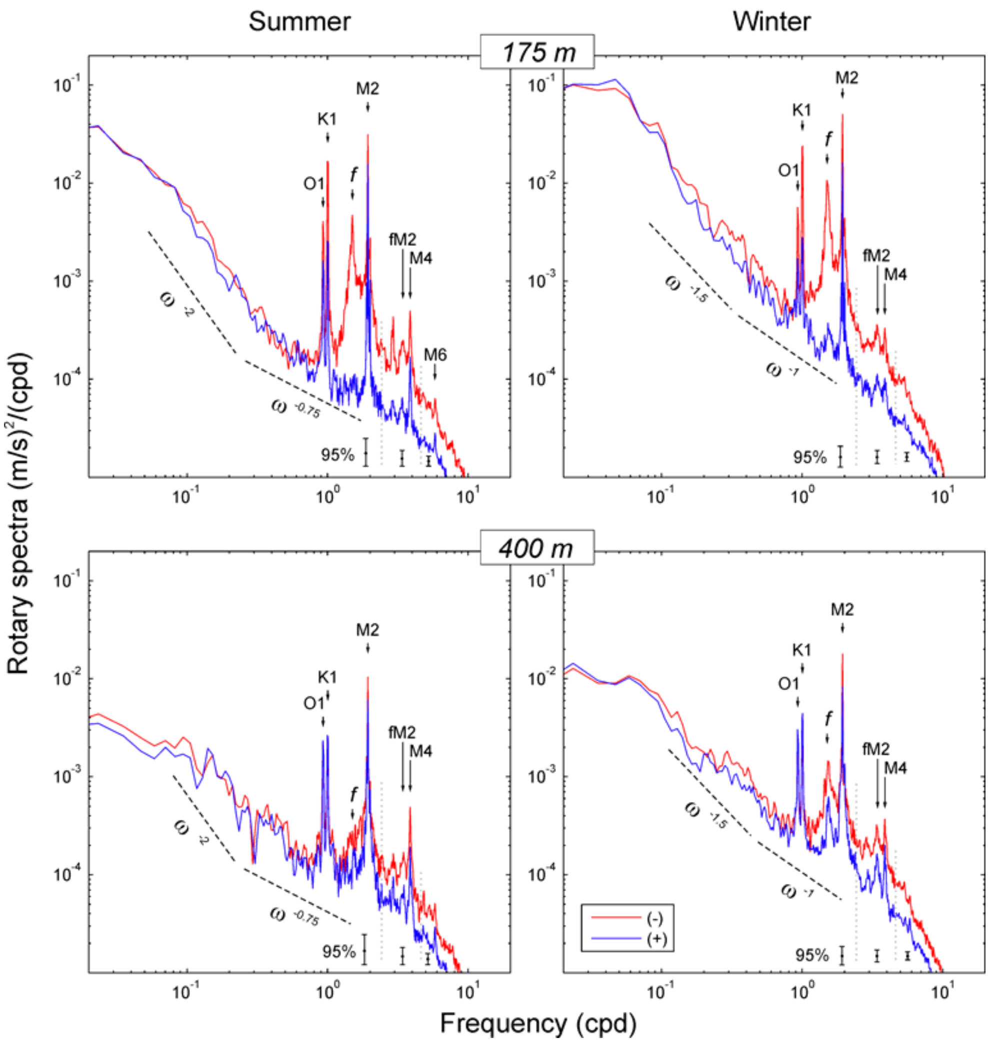

Figure 4.2.1. (Continued)

Near the surface, the tidal and the inertial currents are of the same strength, which indicates that Station A1 is located in the transition zone between the shelf domain, where tidal currents dominate the inertial oscillations, and the offshore domain where inertial currents dominate (Thomson *et al*., 1998).

Diurnal peaks are of slightly larger magnitude in winter than in summer indicating that the amplitude of these currents is only moderately influenced by seasonal factors. However, there is a seasonal change in the phase of diurnal currents off Vancouver Island which is found in the observations and modelling results (Cummins *et al.,* 2000). This seasonal difference, which increases northward with distance from the entrance to Juan de Fuca Strait, is partly attributed to advection by the seasonally changing mean flow off Vancouver Island (Crawford and Thomson, 1984). Other factors, for example relative vorticity induced by the shelf circulation, are likely to be important (Cummins *et al.,* 2000). Semidiurnal currents in the near-surface layer are stronger in summer due to intensive generation of internal waves of semidiurnal frequency at the shelf break (see Section 4.1). The intensification of atmospheric activity in the region in winter is the cause of stronger inertial currents in the upper layer (above the pycnocline, which is typically 20 m deep in the region off southwest Vancouver Island). However, in the subsurface layer, periods of stronger inertial currents are not correlated with the local atmospheric activity (Kundu and Thomson, 1990).

The region near the shelf break off the west coast of Vancouver Island is known for its intensive generation of internal waves (Drakopoulos and Marsden, 1993; Cummins *et al*., 2001). The summer increase in stratification of the upper part of the water column leads to enhanced amplitudes of internal waves. Non-linear semidiurnal and semidiurnal-inertial wave interaction is indicated by the M4 and *f*M2 peaks (Mihaly *et al*., 1998) which are present in all seasons and at all depths, being more pronounced in summer (Figure 4.2.1). The spectral peak at M4 is nearly equally pronounced at all depths, while the peak *f*M2 is more pronounced in the upper layer. The M6 spectral peak is significant in summer down to 175 m depth. Moreover, the peak at the sum of inertial and M4 frequencies (*f*M4) in the spectra of the summer near-surface currents is evidence of non-linear interaction of internal waves of inertial and M4 frequencies. Marginally significant non-linear MK3 and MK5 peaks are present at 35 m depth in the summer spectra. Evidence for the non-linear interaction between inertial and semidiurnal waves (*f*M2) was found in other current meter records collected in the northeast Pacific (Mihaly *et al.,* 1998), while there were no previous reports of *f*M4 waves in this region. The non-linear interaction of inertial and M4 frequencies was recently established in the continental slope region off Portugal (Dias, 2006). The volume of data collected at Station A1 allowed averaging with more degrees of freedom in spectral calculations and a corresponding strong reduction of noise which allows emergence of weak spectral peaks such as *f*M4, MK3, and MK5.

Figure 4.2.2. Isolated segment of the summer 35 m rotary spectra (Figure 4.2.1) showing tidal, inertial, and non-linear tidal and tidal-inertial peaks.

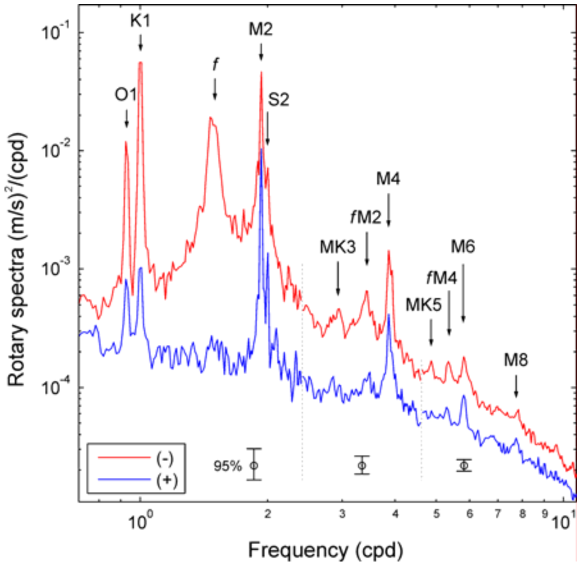

Inertial currents are among the most commonly encountered types of motions in the upper ocean. They represent the free motion of the water particles on the rotating Earth (Thomson, 1981; Stewart, 2003). Inertial currents are induced by wind forcing on the sea surface. When wind relaxes, the Coriolis force remains the primary factor influencing a water particle movement at the sea surface in the open ocean. The Coriolis force acts on a moving particle at 90° to the right from the direction of motion in the northern hemisphere. Therefore, in the absence of other forces, the particle would move in a circle clockwise (CW) in the northern hemisphere. Such motion would produce a peak on the CW component of the rotary spectra while leaving the energy of the counter-clockwise (CCW) component at the background level. Such spectral peaks can be seen at the local inertial frequency *f* in summer spectra of A1 currents at 35, 100, and 175 m depth (Figure 4.2.1). In the winter spectra at these depths, marginally significant inertial peaks emerge in the CCW component, while the CW inertial peak still largely dominates over the CCW peak. This indicates that in winter, the season of strong inertial currents, the inertial motions even near the surface become influenced by the bottom topography (in this case, the proximity of the continental slope) which modifies the circular orbits of inertial motions into elliptical trajectories. According to Eriksen (1982), current ellipses are polarised for the frequencies near the critical frequency σ_c determined by $\sigma_c = (N^2\sin^2\alpha + f^2\cos^2\alpha)^{1/2}$, where N is the buoyancy frequency, f the Coriolis frequency, and α the bottom slope. Taking $\alpha = 3.25\times10^{-2}$ rad, $N = 3.2\times10^{-3}$ rad/s, and $f = 1.09\times10^{-4}$ rad/s, typical for the vicinity of Site A1, we obtain $\sigma_c = 2.07$ cpd, very close to the semidiurnal tidal frequency. For frequencies lower than σ_c a reflection of internal waves from the sloping bottom occurs. Upon reflection, the linear internal waves amplify and turn parallel to the slope, producing current ellipses elongated across the isobaths (Eriksen, 1982).

Inertial currents at 400 m depths are significantly different from the inertial currents at the shallower layers. In summer they are extremely weak, while in winter the inertial peak in the CW spectra is well defined, although much weaker than at the upper layers. Contrary to that, the inertial peak in CCW component of the current at 400 m depth is significantly stronger than those at the upper layers. It stands out from the background well above 95% confidence interval. That is, inertial currents, being nearly circular away from the bottom, induce oscillations in deeper layers where the motions are constrained by the underwater canyon (Figure 3.1.1c) and the current ellipse becomes more elongated but the currents are not exactly rectilinear (CW component still largely prevails). This effect was also observed deep in the axial valley at Endeavour Ridge (Thomson *et al.*, 1990).

To evaluate seasonal changes in the vertical distribution and relative importance of different classes of oceanographic processes, the spectral energy was integrated over specific frequency bands: the low-frequency (LF) band from 0.02 to 0.81 cpd, the diurnal (D) band from 0.81 to 1.22 cpd, the inertial (*f*) band from 1.22 to 1.72 cpd, the semidiurnal (SD) band from 1.72 to 2.23 cpd, and the high-frequency (HF) band from 2.23 to 10.0 cpd. These frequency bands are shown at the upper horizontal axis of the summer 35 m depth plot of the Figure 4.2.1. The bands were delineated using the main spectral features. The D, *f*, and SD bands were centered at corresponding spectral peaks and bounded by the frequencies where the energy falls to the background level. The LF and HF bands include all frequencies lower than the D band and higher than the SD band, respectively. The spectra of RCM-4 and S4 current meter records at frequencies higher than 10 cpd are highly distorted due to their built-in averaging mechanism and instrument response (see Section 3.1). For this reason, frequencies higher than 10 cpd were excluded from the analysis. The energy in the LF band is largely determined by synoptic processes (the LF band starts at 50-day period, therefore neither annual nor interannual oscillations are reflected in LF band in this case). The D and SD bands reflect the tidal energy, while energy in the *f* band represents the energy of wind-generated inertial oscillations. The energy in the HF band largely arises from non-linear tidal and tidal-inertial waves.

Figure 4.2.3 shows the spectral energy integrated over the five frequency bands defined above. The low-frequency motions represent the most energetic part of the spectra (40 to 70% of the total spectral energy). The relative contributions of diurnal, semidiurnal, and high frequency motions to the total energy budget are approximately the same. Both the relative and absolute strength of the inertial currents undergoes significant vertical (see also Figure 4.2.4) and seasonal (see also Figure 4.2.5) change, being approximately twice as strong as the tidal currents in winter, and for upper layers (35 – 175 m depth) and negligibly weak in summer for the deepest layer (400 m depth).

Vertical distribution of the CW, CCW, and total (CW+CCW) energy in the specific spectral bands is presented in Figure 4.2.4. The upper instrument shows the largest energy in all bands except for the LF band in winter. Beside that, the energy in each frequency band has its own characteristic vertical distribution. A near-homogeneous layer of energetic along-shore low-frequency motions forms in the upper 175 m (with the maximum at 100 – 175 m) in winter. Below that depth, the LF energy quickly decreases. Summer LF energy has a maximum near the surface and decreases with depth except for the homogeneous layer between 100 and 175 m depth.

For diurnal and higher frequencies, the CW component generally prevails over the CCW component (Figure 4.2.4), so that the current ellipses have close to circular CW orbits, while at low-frequencies both components are nearly equal, corresponding to rectilinear motions: as was shown with progressive vector diagrams (Figure 4.1.3), the flow is directed along-shore. Semidiurnal currents are clockwise but the CCW component is larger than for diurnal currents, so that semidiurnal ellipses are more polarized than the diurnal ellipses.

The CCW component of the D, *f*, and SD currents is almost uniform in the vertical, consistent with barotropic motions (Figure 4.2.4). In contrast, the CW component experiences pronounced vertical change revealing its highly baroclinic character. Diurnal and particularly inertial energy sharply decrease in the upper 175 m with a subsequent moderate decrease in deeper layers (stratification-modified Coastally Trapped Waves, CTWs, in the D band). The SD energy also generally

Figure 4.2.3. Spectral energy for A1current meter records (1985 - 2004) integrated over five specific frequency bands. (-) denotes CW and (+) CCW rotation.

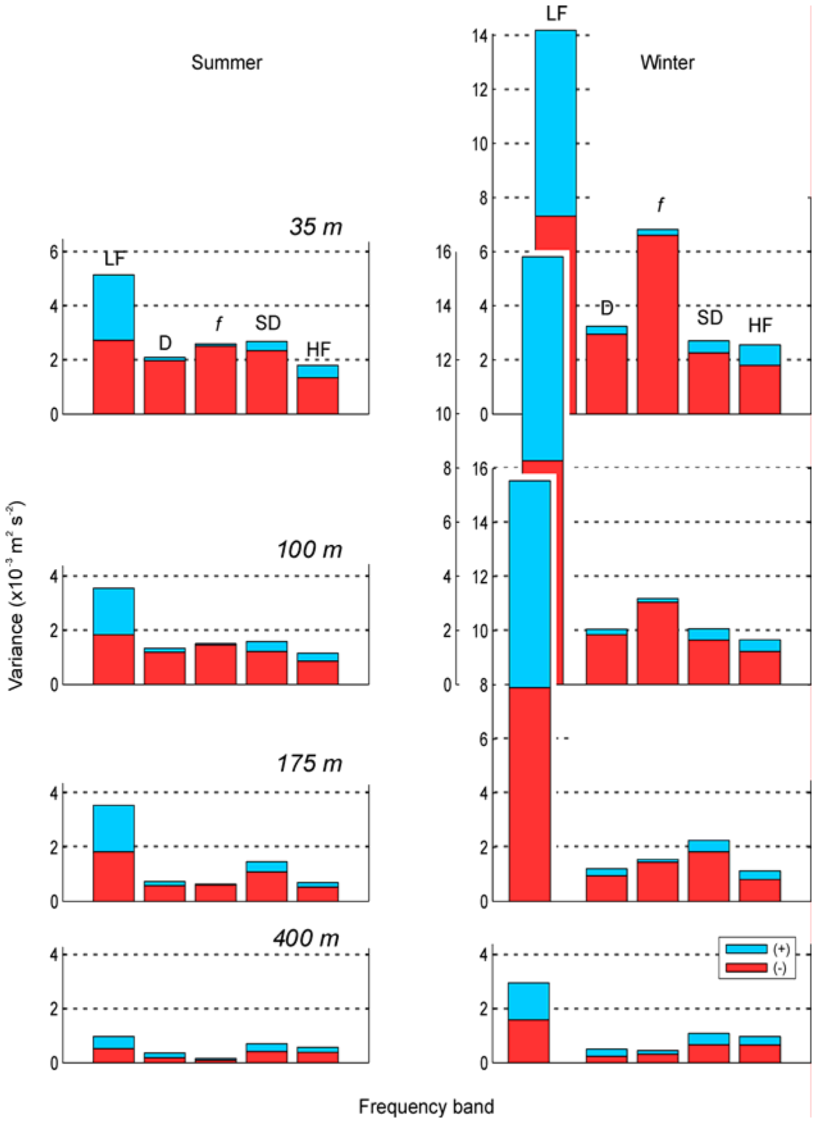

decreases with depth but the rate of the decrease is low between 100 and 175 m (in summer) or there is an increase with a local maximum at 175 m (winter profile). In winter, semidiurnal currents at 175 m depth become almost as strong as at the surface. Further decrease of semidiurnal currents with depth is very gradual, and they become stronger than both diurnal and inertial currents in the deeper layers.

Figure 4.2.5 also shows average band-integrated spectral energy in the diurnal, inertial, and semidiurnal frequency bands, but highlights the seasonal changes. The largest seasonal differences in the spectral energy are associated with winter intensification of atmospheric activity, accompanied by stronger wind forcing. Stronger winter winds cause two to three times stronger low-frequency and inertial oscillations than in summer. Diurnal and semidiurnal energies are slightly higher (10 to 20%) in winter except for the semidiurnal oscillations in the near-surface layer which are 10% more energetic in summer due to the intensive generation of internal waves of semidiurnal frequency as a consequence of enhanced vertical stratification in the upper part of the water column. Large residual variance in the SD band (Figure 4.2.5), particularly in the upper layers, also indicates the significant presence of incoherent baroclinic oscillations (modified internal tides).

To investigate the low-frequency band in more detail, I calculated the rotary spectra of the combined series using all records for each nominal depth (Figure 4.2.6). Here again, I used a frequency-dependent window length to achieve the best compromise between frequency resolution and noise suppression. The borders of the bands and the window length for each band were determined by trial and error. In the band from 9.1×10^{-6} to 3.5×10^{-3} cpd a window of 12.5 years was used; from 3.5×10^{-3} to 1.7×10^{-2} cpd a window of 5.3 years was used; and from 1.7×10^{-2} to 0.6 cpd a window of 340 days was used. For higher frequencies, the window length was taken the same as for the seasonal spectra (see above). Then the parts of the spectra from the above frequency bands were pasted together to obtain combined spectra shown in Figure 4.2.6.

Two distinct broad frequency bands can be defined with respect to the frequency of 0.05 cpd. For frequencies > 0.05 cpd, the spectral background slope and other major features (tidal, inertial, and non-linear peaks) have nearly the same structure at all depths as in Figure 4.2.6. Only the background level and the magnitude of the peaks changes (as described above). At frequencies lower than 0.05 cpd, however, the background falloff rate undergoes a distinct change with depth. It decreases from $\omega^{-0.5}$ near the surface to $\omega^{-0.25}$ at 100 m depth to nearly uniform (frequency-independent) energy level at 175 m depth. The annual

Figure 4.2.4. Vertical distribution of the band-integrated spectral energy for the A1 current meter records (1985 - 2004).

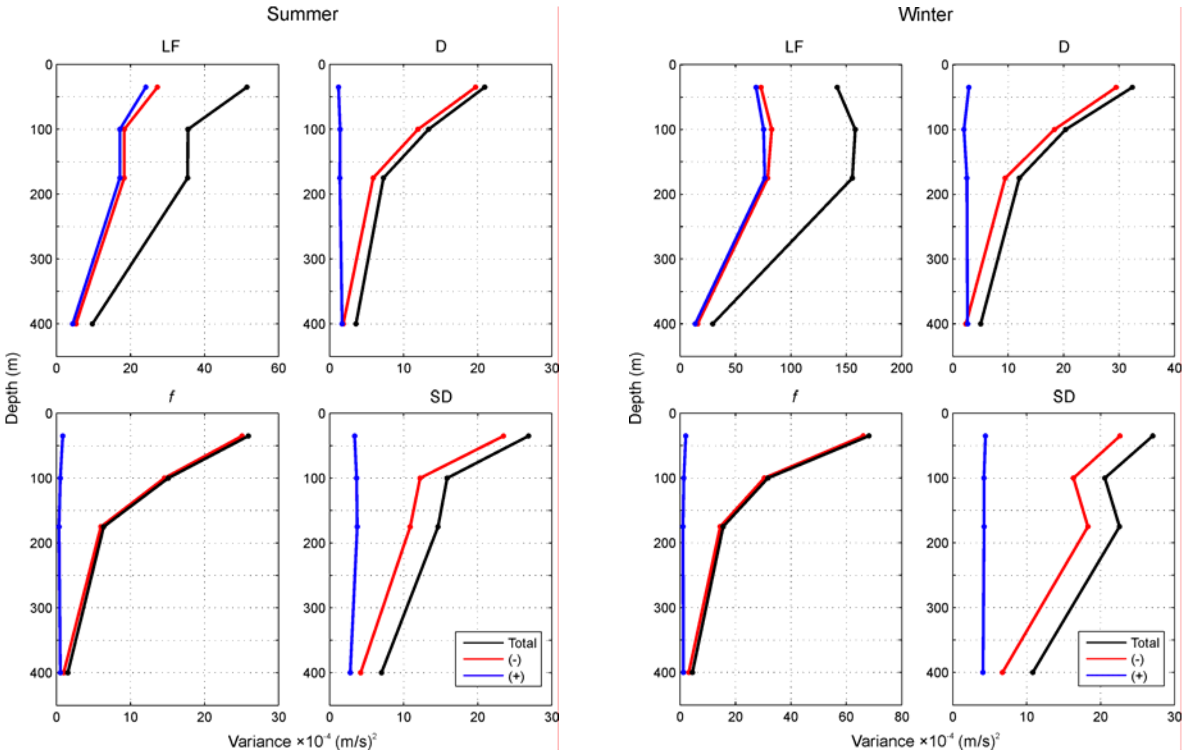

peak (SA) is the most prominent feature of the low-frequency band except for the 400 m depth level where it does not exceed 95% confidence level. The semi-annual peak (SSA) is weak near the surface and does not stand out from the background at all other depths.

The wide band of relatively high energy currents between periods of 2 and 3 years at 35 – 175 m depth is marginally significant, but its presence at all three depth levels (35, 100, and 175 m) indicates that it is a real feature. One suggestion is that this peak is due to ENSO effects. In Section 5.2 (Figure 5.2.3), it will be shown that the alongshore current anomalies at Station A1 which last two to three years correspond somewhat to El Niño episodes. In Section 5.3, it will be confirmed that both the Pacific Decadal Oscillation (PDO) and the El Niño – Southern Oscillation (ENSO) indices are correlated with the alongshore current at Station A1 down to 175 m depth, the PDO playing a more important role in the near-surface currents and the ENSO possessing higher correlation with currents in the intermediate layers. Since the PDO and ENSO are mutually correlated, it is difficult to make a distinction between their individual contributions based purely on statistical analysis. However, physical concepts proposed suggest that the ENSO likely exerts more immediate influence on the slope currents, affecting them via coastally trapped waves propagating from the equatorial region poleward along the eastern oceanic boundaries (Clarke and Van Gorder, 1994; Sections 2.2.2 and 5.3).

Summarizing the findings of the spectral analysis, the currents in the region are dominated by the low frequency motions, of which the most energetic is the annual cycle (except for the flow at 400 m depth which is affected by the submarine canyon), and by narrow-band diurnal, semidiurnal, and inertial oscillations. Internal tides influence the flow down to 175 m depth. Non-linear interactions of tidally induced waves with each other and with inertial waves play a dominant role in the high-frequency band. There is also some evidence for the influence of El Niño oscillations on the currents at Station A1.

Figure 4.2.5. Average band-integrated spectral energy by season for the A1 current meter records (1985 - 2004) in the diurnal (D), inertial (*f*), and semidiurnal (SD) bands. Darker and lighter colors for the D and SD bands denote coherent (explained with least squares harmonic tidal analysis) and random (residual) variance, respectively.

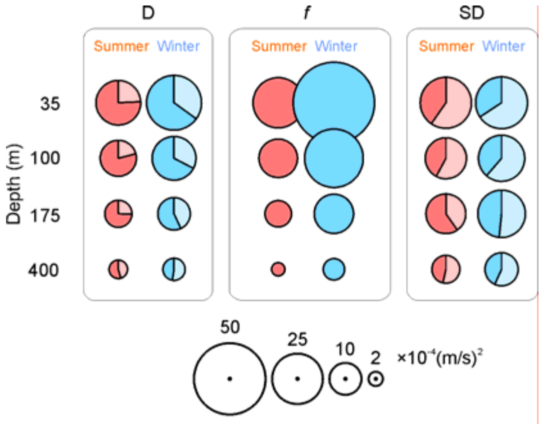

Actual values ×10⁻⁴ (m/s)²

Depth (m)	D		f		SD	
	Summer	Winter	Summer	Winter	Summer	Winter
35	19.5	29.5	24.8	64.6	25.7	26.4
100	12.8	18.7	14.5	33.6	16.5	20.9
175	7.2	10.3	6.9	15.1	15.5	22.1
400	3.4	4.8	1.7	4.5	7.6	10.8

Figure 4.2.6. Broadband rotary spectra for the series combined over the entire period of observations (39 deployments: 1985 - 2004).

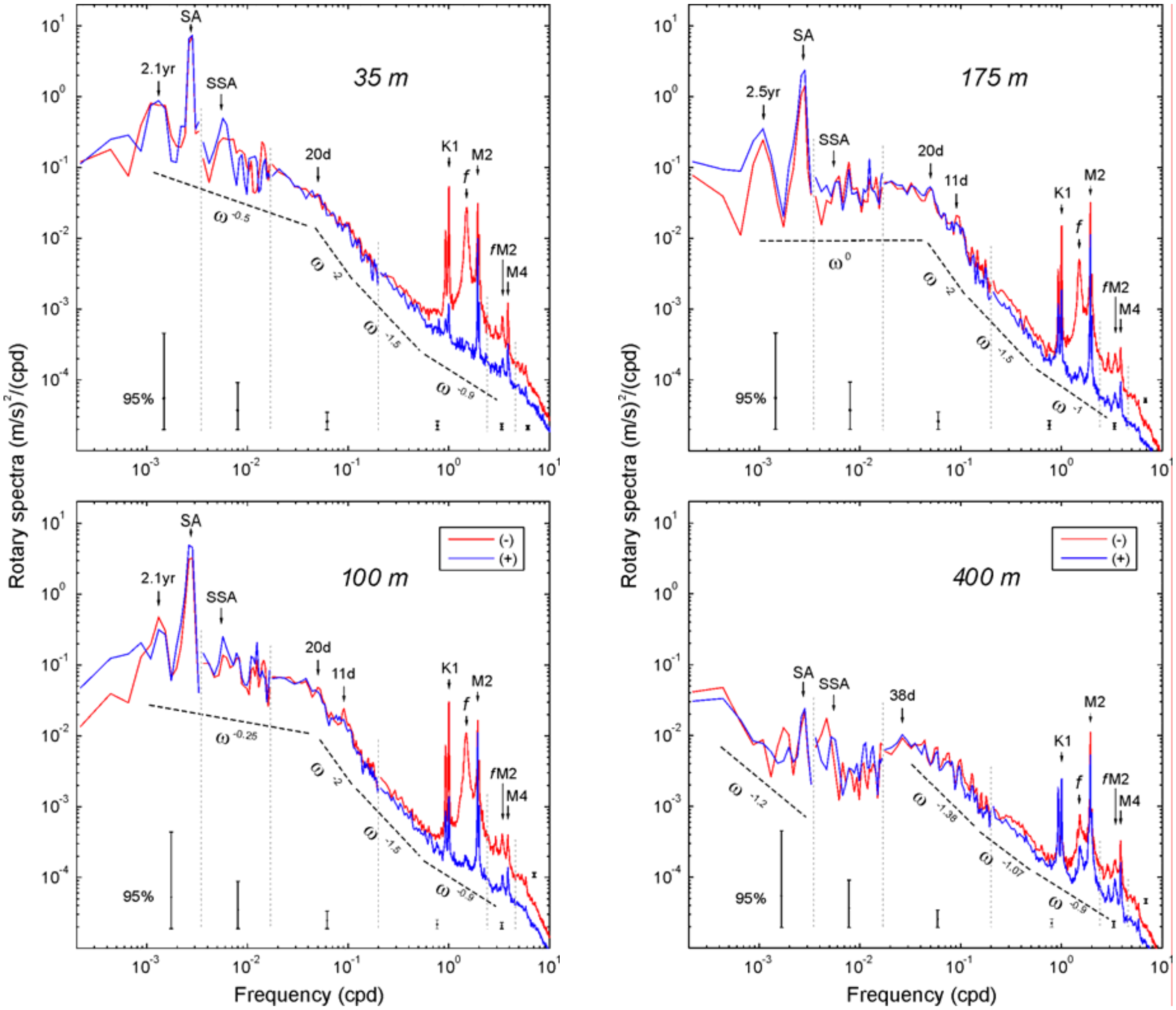

4.3. Water property characteristics

This section examines the water properties observed in the area of Station A1, the source region of this water, and the relative contribution of each water mass to the observed water properties. The concept of water mass in physical oceanography is summarised by Dobrovol'skii (1961) who defined water mass as a "large volume of water, formed in a certain region of the World Ocean – the home or source of this mass, under certain conditions, which possesses over a long time almost constant and continuous distribution of physical, chemical and biological characteristics, which make up a single system, and which displaces itself a single whole". Primary water mass classification based on temperature and salinity characteristics and their distribution in the World Ocean are described in Sverdrup *et al.* (1942), which is still considered a classical work on the subject (Warren, 1992). Based on this seminal work and some later publications (e.g. Mamayev, 1975), the classification was updated and slightly expanded by Emery and Meincke (1986). According to Emery and Meincke (1986), there are three main water masses in the upper layer (0-500 m) of the northeast Pacific (Figure 4.3.1). These are the Pacific Subarctic Upper Water (PSUW), the East North Pacific Central Water (ENPCW), and the Pacific Equatorial Water (PEW). The PSUW is relatively cold (range 3.0 – 15.0oC) and fresh (range 32.6 – 33.6 psu) water. It is formed in the Subarctic North Pacific by surface cooling and freshening. The PEW is characterised by relatively high salinity (34.5 – 36.0 psu) and high temperature (7 – 23oC). According to Emery and Meincke (1986), the source region of PEW is the central and western equatorial Pacific.

The A1 mooring region is located away from the areas of major water mass formation (Figure 4.3.1) and, therefore, consists of a mixture of different water masses advected to the study region by the currents. The relative content of each water type is determined by the distance from the source, the intensity and continuity of the flow, and the strength of mixing the flow encounters on its way from the source. Emery and Meincke (1986) distinguish the water in this area as a separate water mass, the Eastern North Pacific Transition Water (ENPTW), noting that it represents the mixture of PSUW with coastal waters along the eastern boundary. The PSUW and PEW appear to have greater influence on the formation of water properties in the region than the ENPCW due to the prevalence of along-shore advection compared to onshore transport toward the eastern boundary of the North Pacific.

Observed properties of the CUC include high temperature and salinity, high nutrient content, and low dissolved oxygen relative to the upper layer water brought by the CC from the north (Mackas *et al.*, 1987). All of these properties are indicative of water of equatorial origin (the PEW) contrary to the PSUW, prevailing closer to the surface. To evaluate the relative content of each of these two water masses in the water column over the upper continental slope, I examine averaged temperature-salinity (T-S) curves for all available data for the standard CTD station LC09 located close to the A1 mooring site (the map in Figure 3.1.1 shows the station location). March and July curves in

Figure 4.3.1. Supply of PEW to the CUC region. The upper water masses in the North-Eastern Pacific according to Sverdrup *et al*. (1942) and Emery and Meincke (1986), and schematic of major currents in the equatorial region influencing the depth range of 100-400 m.

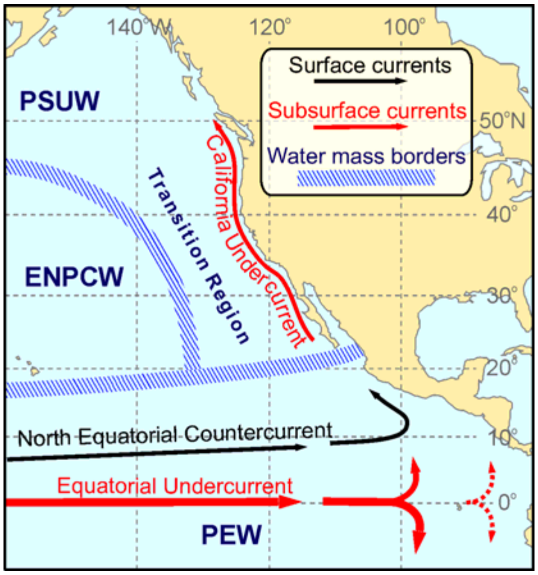

Figure 4.3.2 are intended to represent winter and summer conditions in the area. It is seen from the figure that the maximum contribution from the PEW (40%) roughly coincides with in situ density σ_t=26.55, which is located at a depth of 175 m in the summer and 200 m in the winter. Therefore, we can assume that the maximum poleward transport (core of the Undercurrent) near Station A1 also occurs near this depth. At 100 m the PEW content drops under 30%. Seasonal variations below 150 m are very small suggesting that the flow at those depths carries water of the same origin throughout the year. Above 150 m, summer flow brings water containing properties of the PSUW to the study region, while in winter the water properties are closer to the PEW.

To explore spatial and seasonal variations of the relative PEW content in the water above the continental slope off Vancouver Island, I used hydrographic data collected during oceanographic cruises organized by the Institute of Ocean Sciences (IOS) in the study region. The IOS data repository contains over 16,000 CTD profiles sampled in the area bounded by 47° and 51°N and 124° and 130°W for the time period from the beginning of CTD measurements up to December 2005. All CTD profiles arranged in lines across the slope were selected and sorted into groups, each group representing one cross-section. Altogether, over 800 individual cross-sections were identified and examined. The cross-sections were then sorted into groups according to their location. Each such group is a standard hydrographic line occupied by IOS (Figure 4.3.2). The lines usually extend about 100 km offshore to depths of 1000 – 2000 m; i.e. they span the shelf and most of the slope. The cross-sections chosen for the analysis were subject to certain additional constraints, which allowed calculation of geostrophic velocity on those cross-sections (the results of geostrophic velocity calculations will be presented in the next section). Altogether, 293 individual water property cross-sections were chosen for the analysis. The data span the period between 1979 and 2005.

Figure 4.3.3 shows the seasonal average PEW content at each hydrographic line. Maximum PEW concentration marks the core of the Undercurrent. In most cases, the core is located between 150 and 200 m depth, with elevated PEW concentration spread vertically from 100 m to 400 m depth. In the cross-shore direction, the core of the elevated PEW concentration is either attached to the shelf break (typical winter picture) or separated from the shelf break by 5 to 40 km (typical for summer). Although the peak of the PEW concentration is close to the shelf break, the tongue of the equatorial water spreads far seaward beyond the sampled area of most cross-sections. The hydrographic lines with the farthest seaward extent (Lines G and T extend 100 and 150 km from the shelf break, respectively) still show a highly elevated PEW concentration (>35%) in the layer from 100 to 200 m depth at their outer edge. White areas in the near-surface layer (upper 100 m) contain water whose properties are affected by external processes (air-sea interaction) and can not be obtained by mixing of the PSUW and PEW with the assumption that water properties are conserved.

Figure 4.3.4 shows the along-shore and vertical distribution of the seasonal average PEW percentage in the area extending 60 km seaward from the shelf break. In summer, maximum PEW concentration is observed around 175 m depth along the entire coast of Vancouver Island. In winter, the core of high PEW concentration shoals from about 200 to 175 m depth over the extent of the examined region. A tongue of water with elevated PSUW content at depths below approximately 400 m and with maximum at about 700 m depth indicates a weak equatorward flow at those depths, which is consistent with the model studies of McCreary (1981) and Clarke and Van Gorder (1994) and also observed by Werner and Hickey (1983) and Hickey (1989a) which suggest a weak equatorward baroclinic pressure gradient below the poleward undercurrent.

Figure 4.3.5 shows that the average PEW concentration in the zone of the CUC drops from 31 to 23% over the 400 km extent from the southern part of Vancouver Island to southern Queen Charlotte Sound. This yields a gradient of 2% per 100 km of along-shore distance. Assuming a roughly meridional coastline to the south of Vancouver Island and a linear change of the PEW concentration at the above rate along the entire coast, I estimate that 100% PEW occurs around 19°N, which corresponds remarkably well with the location of the northern boundary of the PEW source region (Figure 4.3.1). The spatial maximum of the

Figure 4.3.2. T-S diagram showing March and July average curves based on CTD data for LC09 in the vicinity of A1 (bottom depth 600 m) and characteristic curves for PSUW and PEW based on data from World Ocean Atlas (Levitus, 1994). Also shown is the percentage of PEW assuming mixing between the two water masses along surfaces of constant σ_t. The green lines are constant σ_t curves.

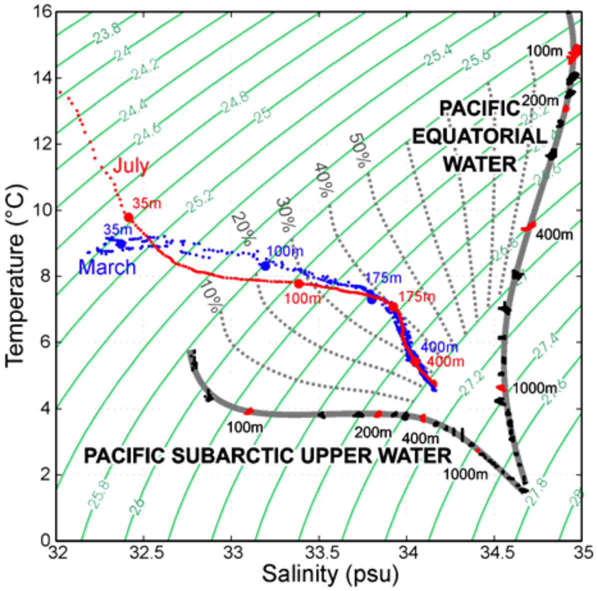

Figure 4.3.3. Seasonal average (from 1979 to 2005) PEW content at the standard hydrographic lines (labelled in boxes at the top of each pair of plots) off the west coast of Vancouver Island (see Figure 3.1.1). The blank areas at low depths contain water which can not be obtained by mixing of PSUW and PEW. The numbers and stripes at the bottom of each plot denote the number of sampled profiles used for averaging on the corresponding cross-shore extent. Isopycnals with corresponding σ_t values are also shown in the plots.

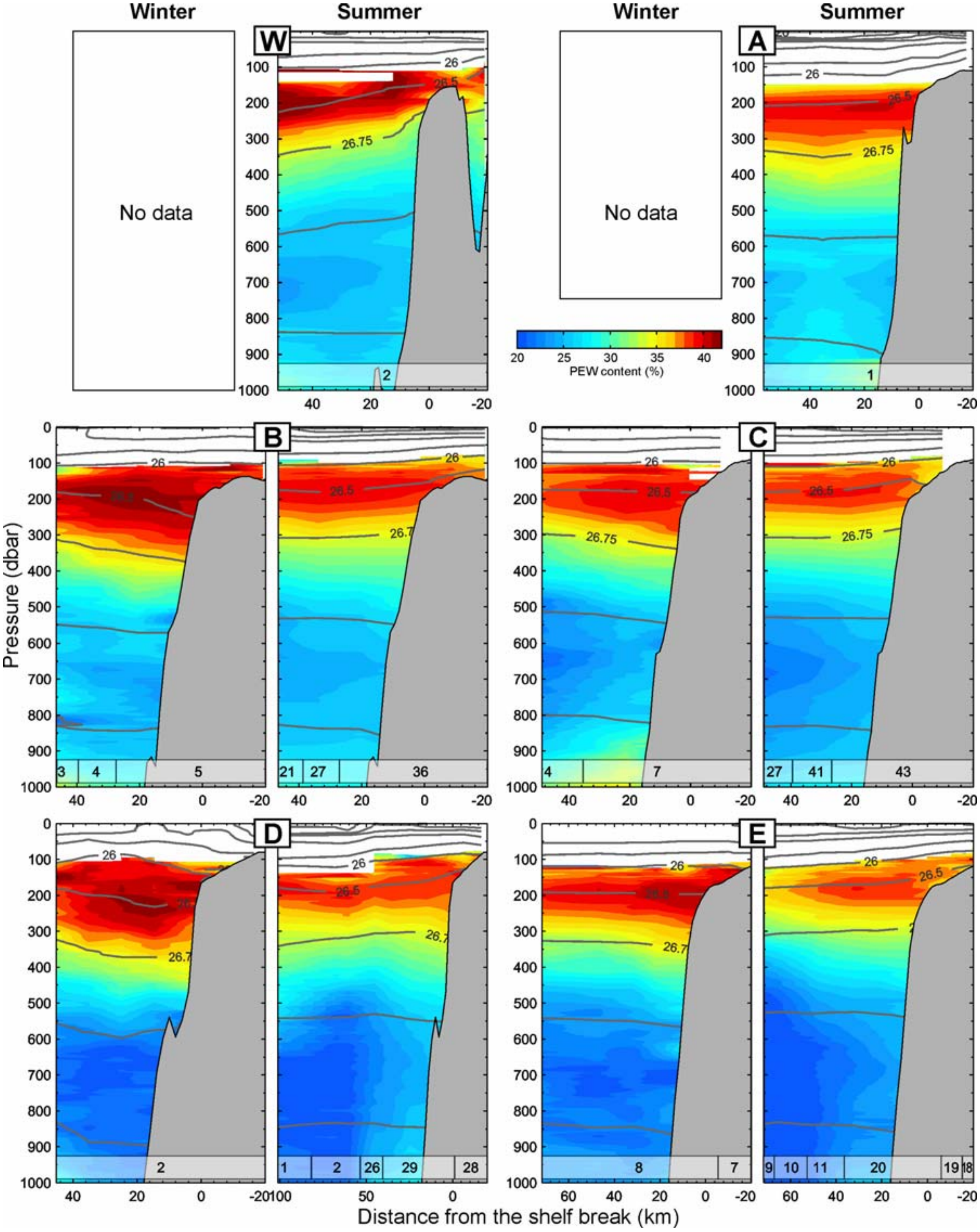

PEW concentration (mean concentration in the core of the Undercurrent) off the southern Vancouver Island is around 40% and drops in the poleward direction by roughly 1% every 100 km. Although the along-shore gradient is evident, this rate of change is less reliably established than in the case of average concentration because the line-to-line variations (the "noise") are larger. I note that the obtained linear trend of 1% per 100 km is too low to gain 100% concentration from the initial 40% at the same southern location of 19°N as for the average concentration. The rate of change of the PEW concentration in the core of the Undercurrent may, therefore, vary along the coast and may be lower off Vancouver Island then to the south.

The distribution of water properties established by the above analysis is consistent with the vertical structure of along-shore flow pattern established in Section 4.1 using current meter data: the seasonally varying flow in the upper layers and predominantly poleward year-round flow at 175 m and below. The above analysis justifies the assumption that the PSUW and the PEW both play a key role in formation of the water properties in the California Current System off Vancouver Island. The same

Figure 4.3.3. (continued)

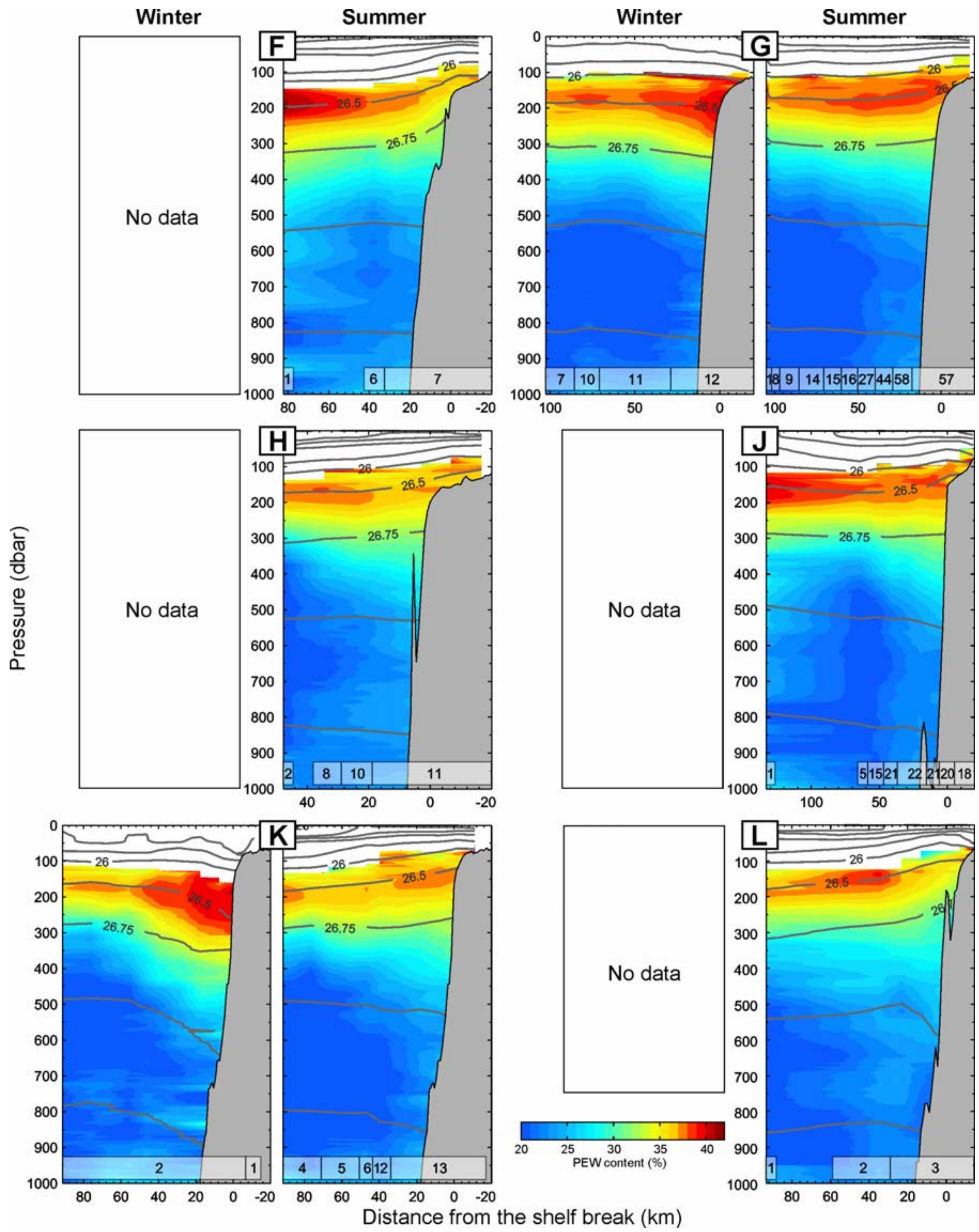

is considered true for the whole extent of the CCS (e.g. Tibby, 1941; Sverdrup and Fleming, 1941; Reid *et al*., 1958).

Having established the presence of the PEW in the CUC off Vancouver Island, it is now worthwhile to trace the path of this water from its origin in the Equatorial Pacific. There are two strong currents in the equatorial current system that can carry high temperature and high salinity PEW from the region of its formation to the eastern part of the ocean. These are the Equatorial Undercurrent (EUC) and the North Equatorial Countercurrent (NECC). The EUC is a year-round subsurface flow bounded by the top and bottom of the thermocline with speeds reaching 1-1.5 m/s at core depths of 40-200 m. The EUC is centered at the equator with half-width of about 2^{o} latitude (~200 km) and has a total transport of 30-40 Sv (Wyrtki, 1967). The NECC is a surface flow, located between 5 and 10^{o} N, with maximum near-surface velocities of 0.4-0.6 m/s and velocities of 0.1 m/s extending to depths of about 200 m. The average transport is 15 Sv (Wyrtki, 1967). The NECC is a year-round current with a considerable seasonal component: from February to April it weakens and narrows relative to the rest of the year.

There is a range of opinions about the ultimate fate of the EUC. Some studies (e.g. Eden and Timmerman, 2004) suggest that it loses most of its strength before reaching the Galapagos Islands off the South American coast. Other studies (Stevenson and Taft, 1971) find evidence of the EUC to the east from the Galapagos Islands. Philander (1980) discusses a mechanism of

Figure 4.3.3. (continued)

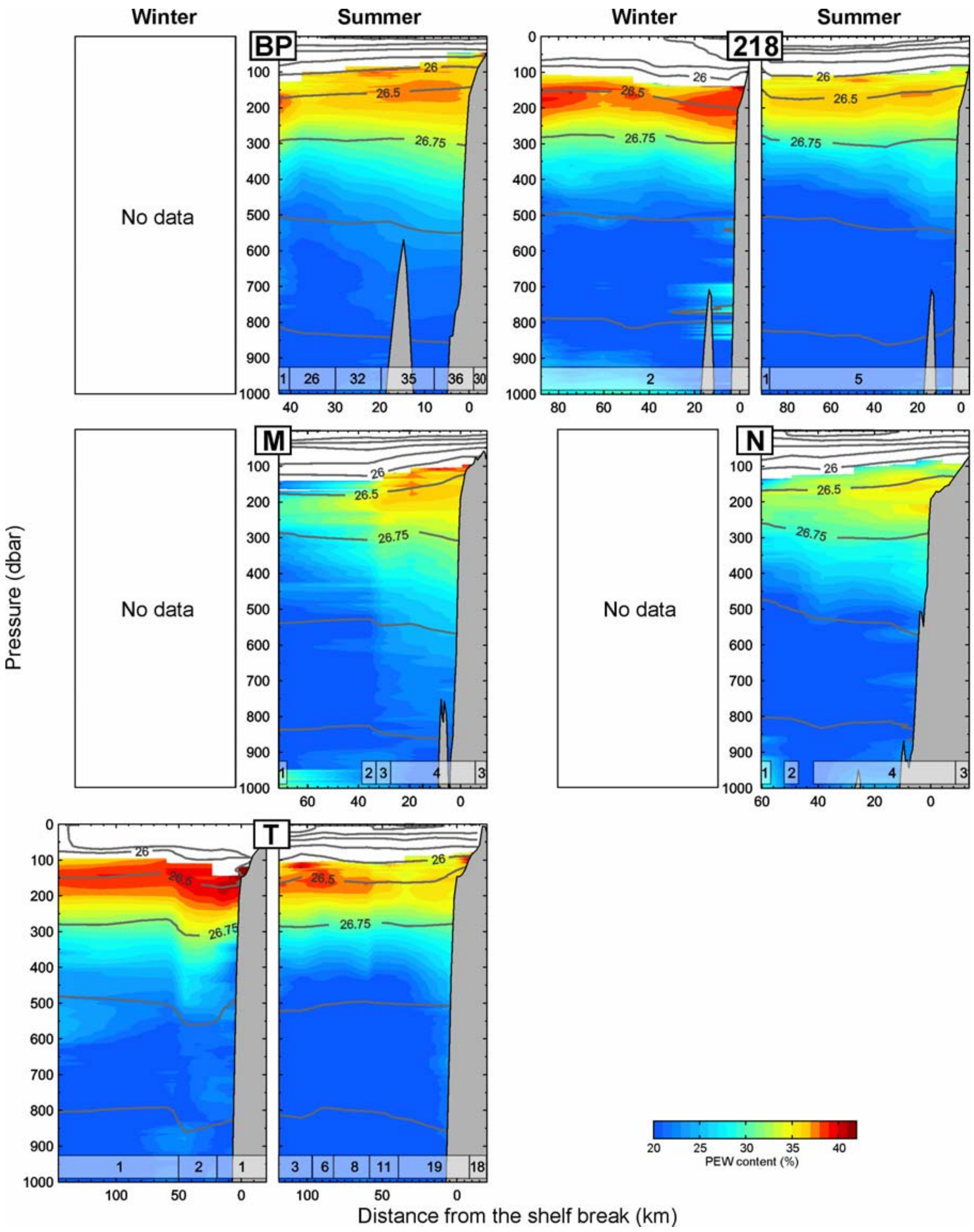

cessation of the EUC by equatorially trapped Kelvin and Rossby waves which destroy the eastward pressure gradient force, the driving force of the EUC. The deceleration and decay begins at about 100°W, roughly 1000 km upstream of the Galapagos Islands. In its final decay stage, the EUC probably broadens, weakens, and deepens and has a highly variable structure both in space and in time (Philander, 1980; Steger *et al*., 1998; Eden and Timmerman, 2004). The water brought by the EUC and the NECC to the Eastern Equatorial Pacific spreads in meridional direction into the tropical regions both in the northern and in the southern direction (Wyrtki, 1967). Using the denitrification parameter N^* as a tracer, Castro *et al*. (2001) conclude that the PEW from the eastern tropical North Pacific is advected further to the north by the CUC. Pierce *et al*. (2000) trace the vertical maximum of spiciness (high temperature and salinity, an indicator of the equatorial water) along the continental slope from 34 to 51°N in the layer from 100 to 250 m depth. They also use potential vorticity as a tracer, which indicates a continuous flow near $\sigma_t = 26.6$-26.7 level (200-250 m depth), the depths of the poleward Undercurrent.

The vertical and cross-shore distributions of PEW allow for estimation of the vertical or horizontal mixing coefficients. Consider a diffusion equation for a property C (PEW concentration in this case) along the shore:

Figure 4.3.4. Seasonal average PEW content at the standard hydrographic lines (marked with vertical lines and letters) as a function of distance along the west coast of Vancouver Island calculated for the cross-shore range from the shelf break to 60 km seaward of the shelf break. The averages are calculated using data from 1979 to 2005.

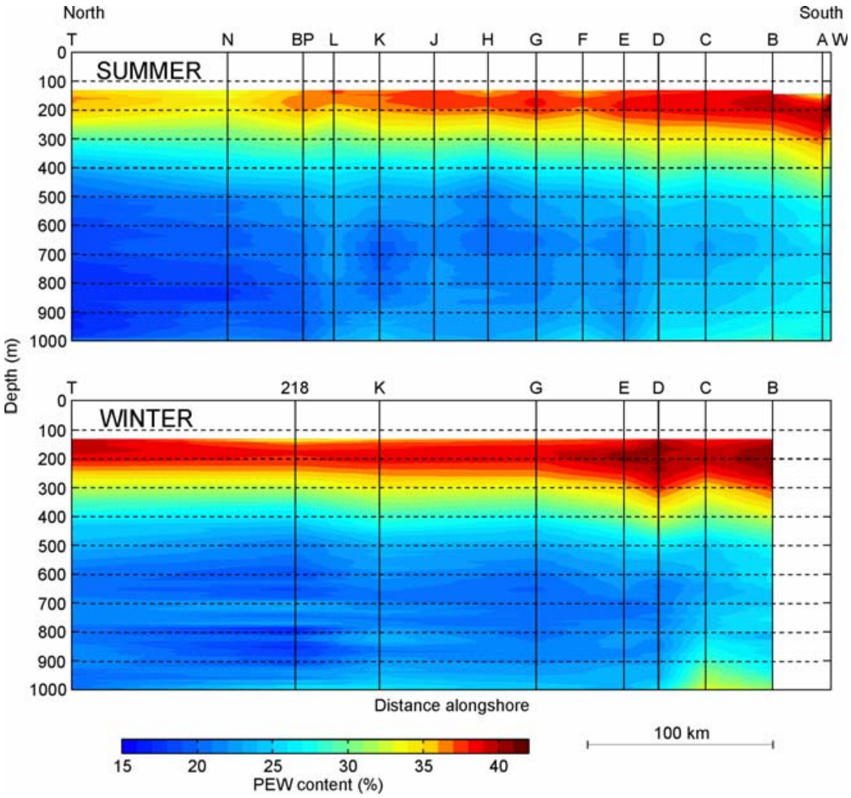

$$v\frac{\partial C}{\partial y}=\frac{\partial}{\partial x}\left(K_h\frac{\partial C}{\partial x}\right)+\frac{\partial}{\partial y}\left(K_h\frac{\partial C}{\partial y}\right)+\frac{\partial}{\partial z}\left(K_v\frac{\partial C}{\partial z}\right) \tag{4.3.1}$$

where x, y, and z are the cross-shore, alongshore, and vertical coordinates, respectively, v is the alongshore component of the current velocity, and K_v and K_h are the vertical and horizontal mixing coefficients, respectively. Let us first consider only vertical mixing. Assume C changes as

$$C = C_0 e^{-y/L}\frac{H^2}{z^2+H^2}, \tag{4.3.2}$$

(C. Garrett, pers. comm., 2008) where C_0 is the initial value of C (at the southern boundary of the undercurrent), L is the alongshore length scale of the current, and $H=H(x)$ is half the vertical width of the current. In this expression, $H^2/(z^2+H^2)$ models the vertical profile of C with maximum value at $z = 0$ (the core of the PEW concentration). Ignoring horizontal mixing, (4.3.1) at $z = 0$ becomes

$$\frac{v}{L}=2\frac{K_v}{H^2}, \tag{4.3.3}$$

from which

$$K_v=\frac{1}{2}\frac{vH^2}{L}. \tag{4.3.4}$$

Taking $v = 5\times10^{-2}$ m/s (mean observed speed of the undercurrent, see Section 5.1), $H = 50$ m, and $L = 5\times10^6$ m, I estimate K_v to be approximately 1.25×10^{-5} m^2/s. This value agrees well with most estimates by other authors; e.g. Yamazaki and Lueck (1987) estimated K_v to be 1.8×10^{-5} m^2/s in the depth range 150-250 m off southern California using measurements of the vertical microstructure of currents and water properties while Ledwell *et al.* (1998) estimated K_v at 1.2×10^{-5} m^2/s for pycnocline depths based on the results of a tracer release experiment in the North Atlantic.

It is possible to estimate the horizontal eddy diffusivity, K_h, in the manner used to derive (4.3.4). I assume that the cross-shore distribution of PEW concentration is described by a model similar to (4.3.2), with H replaced by W_c, the characteristic horizontal half-width of the undercurrent, and z replaced by x. Then, ignoring both vertical mixing and along-shore mixing (the latter based on the fact that the along-shore scale is much larger than the cross-shore scale), I find

$$K_h=\frac{1}{2}\frac{vW_c^2}{L}. \tag{4.3.5}$$

Taking $W_c = 2\times10^4$ m (based on the cross-shore structure of the undercurrent obtained in Section 5.1), I estimate K_h to be approximately 2 m^2/s. Horizontal eddy diffusivity estimates by different authors vary by several orders of magnitude (from 1 to 10^5 m^2/s) for different conditions and spatial scales. In the absence of consistent estimates for the horizontal eddy diffusivity, it is difficult to comment on plausibility of my estimate for K_h. I only note that, based on the tracer release experiment mentioned before, Ledwell *et al.* (1998) also estimated K_h to be 2 m^2/s for spatial scales of 1 – 10 km. Although my estimates of K_v and K_h are approximate and can not be used to determine the importance of horizontal and vertical mixing in the undercurrent relative to the other parts in the ocean, it is likely that horizontal mixing plays an important role in the spreading of the Equatorial water from the core of the undercurrent. Indeed, the region is known for its intensive

Figure 4.3.5. Maximum and average content of PEW on the hydrographic lines off the west coast of Vancouver Island in the zone which extends 60 km offshore from the shelf break and from 100 m depth to the bottom. The data for each line are seasonal averages for the period from 1979 to 2005. Winter data for Line T (dotted lines) involves no statistical averaging as the line was sampled only once in winter. Maximum corresponds to values in the core of the undercurrent.

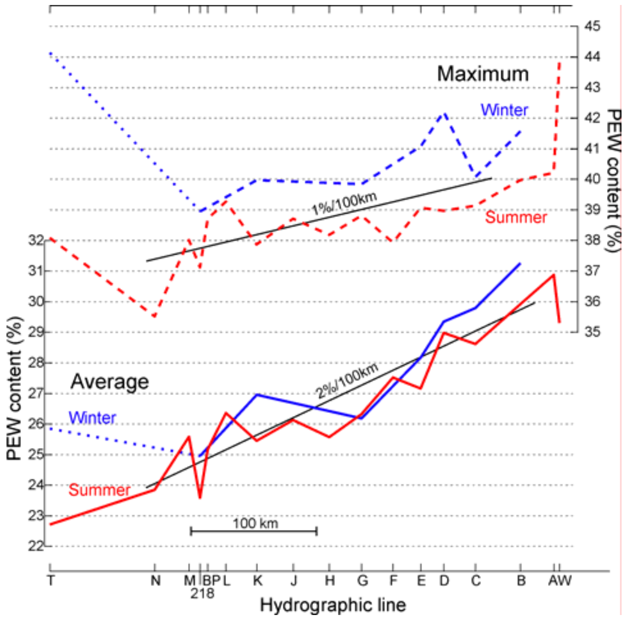

mesoscale activity arising from instability of the California Undercurrent (Section 2.2.2). The tongue of elevated PEW concentration extending far seaward from the area of the poleward flow (compare Figures 4.3.3 and 5.1.4) also supports the conclusion about the importance of horizontal mixing.

5. Characteristic features of the California Undercurrent

5.1. Geostrophic velocity along the outer shelf and upper slope off Vancouver Island

Purpose

Hydrographic data collected over the continental shelf and slope along the west coast of Vancouver Island have been used to investigate the geostrophic along-shore flow in the region. The calculations allow examination of the cross-slope and along-slope structure of the flow over the upper slope. Results are compared to the current meter data to validate the method of current velocity estimates using CTD data and to examine how the calculated baroclinic currents relate to the total directly measured currents.

Theoretical background

Stewart (2003) discusses the theoretical background behind the method of estimating ocean currents using hydrographic data. The method, called the "Dynamic Method", was initially derived by Sandström and Helland-Hansen (1903) based on Bjerknes' Circulation Theorem. Calculations are based on the geostrophic approximation (hence the name, "geostrophic currents") of the equations of motion in a rotated frame with friction neglected, specifically,

$$\frac{\partial u}{\partial t}+u\frac{\partial u}{\partial x}+v\frac{\partial u}{\partial y}+w\frac{\partial u}{\partial z}=-\frac{1}{\rho}\frac{\partial p}{\partial x}+fv \qquad (5.1.1)$$

$$\frac{\partial v}{\partial t}+u\frac{\partial v}{\partial x}+v\frac{\partial v}{\partial y}+w\frac{\partial v}{\partial z}=-\frac{1}{\rho}\frac{\partial p}{\partial y}-fu \qquad (5.1.2)$$

$$\frac{\partial w}{\partial t}+u\frac{\partial w}{\partial x}+v\frac{\partial w}{\partial y}+w\frac{\partial w}{\partial z}=-\frac{1}{\rho}\frac{\partial p}{\partial z}-g\,, \qquad (5.1.3)$$

where (u,v,w) are the components of current velocity along the axes (x,y,z) of a Cartesian coordinate system, t is time, ρ is water density, p is pressure, g is gravitational acceleration, and $f=2\Omega\sin\varphi$ is the Coriolis parameter for Earth's angular velocity Ω and latitude φ. Scaling the above equations for horizontal distances L with typical values of 100 – 1000 km, horizontal velocity $U \sim 10^{-1}$ m/s, time scale $T=L/U \sim 10^{6}$-10^{7}s, water depth $H \sim 500-1000$ m, $f \sim 10^{-4}\,\text{s}^{-1}$ for mid-latitude, $\rho \sim 10^{3}\,\text{kg/m}^{3}$, and $g \sim 10^{1}\,\text{m/s}^{2}$ leaves the vertical pressure gradient force and the gravity force the only important forces (to 10^{-6}) in the vertical (the hydrostatic balance), such that,

$$\frac{\partial p}{\partial z}=-\rho g\,. \qquad (5.1.4)$$

In the horizontal, only the pressure gradient force and the Coriolis force are considered important (to $10^{-2}-10^{-3}$), whereby

$$\frac{1}{\rho}\frac{\partial p}{\partial x}=fv \qquad (5.1.5)$$

$$\frac{1}{\rho}\frac{\partial p}{\partial y}=-fu\,. \qquad (5.1.6)$$

Equations 5.1.5 and 5.1.6 represent the geostrophic balance, relating the slope of the isobaric surfaces to the horizontal velocity.

Differentiating (5.1.5) and (5.1.6) with respect to depth, changing the order of differentiation on the left hand side, and ignoring terms with $\partial\rho/\partial z$ unless they are multiplied by g (the Boussinesq approximation, e.g. Kundu, 1990) we get

$$\frac{1}{\rho_0}\frac{\partial}{\partial x}\left(\frac{\partial p}{\partial z}\right)=f\frac{\partial v}{\partial z} \qquad (5.1.7)$$

$$\frac{1}{\rho_0}\frac{\partial}{\partial y}\left(\frac{\partial p}{\partial z}\right)=-f\frac{\partial u}{\partial z}\,. \qquad (5.1.8)$$

Figure 5.1.1. Schematic diagram illustrating calculation of geostrophic velocity from a pair of hydrographic stations A and B.

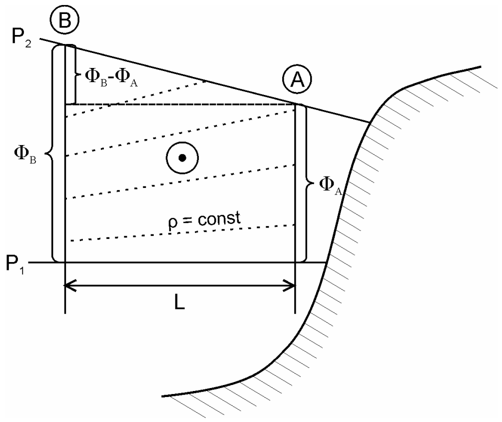

Figure 5.1.2. Hydrographic lines occupied by the Institute of Ocean Sciences for which geostrophic velocity was calculated. Red lines are those for which average seasonal geostrophic velocity is shown in Figure 5.1.4. Circles on the lines show standard location of hydrographic stations. Blue asterisks are the locations of time series of hydrographic casts. The black triangle is the location of the current meter Station A1.

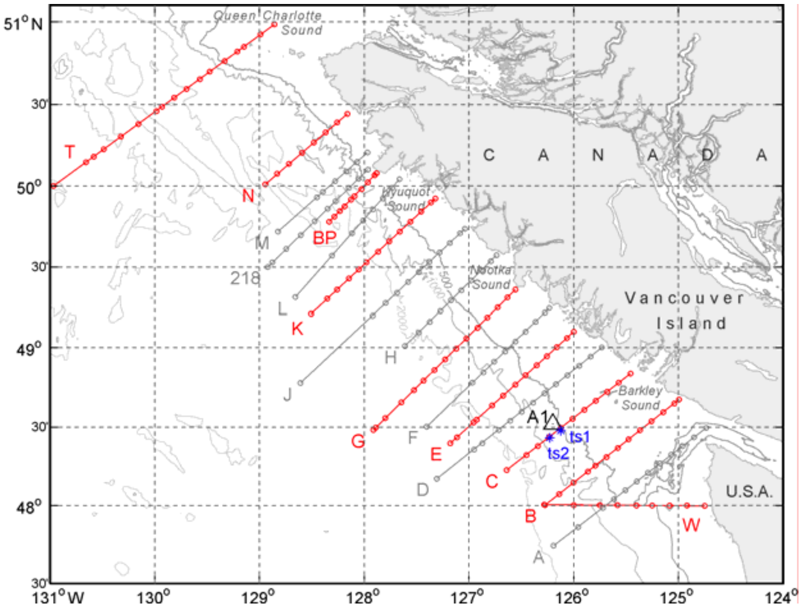

Substituting ∂p/∂z from (5.1.4) to (5.1.7) and (5.1.8) we obtain the so-called "thermal wind" equations which relate the vertical velocity shear to the horizontal density gradient in the cross-flow direction:

$$-\frac{g}{\rho_0}\frac{\partial \rho}{\partial x} = f\frac{\partial v}{\partial z} \qquad (5.1.9)$$

$$-\frac{g}{\rho_0}\frac{\partial \rho}{\partial y} = -f\frac{\partial u}{\partial z}\,. \qquad (5.1.10)$$

The slope of isobaric surfaces can be supported by a sloping sea level which produces a barotropic flow, and also by variations in density within the water column which produce a baroclinic flow. Hydrographic casts made from a ship provide information only on the internal density structure. Therefore, the Dynamic Method can be used to estimate only the baroclinic component of the flow.

According to (5.1.5) and (5.1.6), it is possible to use the slope of the isobaric surfaces, $\partial\zeta/\partial x$, where $\zeta(p,x)$ is an isobaric surface, between pairs of hydrographic profiles in a cross-section to estimate the velocity component normal to the cross-section. Precise direct measurements of isobaric surface slopes in the ocean are not feasible. In practice, the slope is calculated from differences in geopotential anomaly between pairs of stations; using temperature and salinity profile records, the properties that can be measured with sufficient precision, for geopotential analysis. The geopotential is defined as

$$\Phi \equiv \int_0^z g\,dz\,. \qquad (5.1.11)$$

From the hydrostatic equation (5.1.4) we can write

$$\frac{\delta p}{\rho} = -g\delta z\,, \qquad (5.1.12)$$

and using definition of Φ (5.1.11)

Figure 5.1.3 (a) Isopycnal excursions at time series stations TS1 (red lines) and TS2 (blue lines). (b) Geostrophic velocity calculated between Stations TS1 and TS2 as a function of the time interval between samples at these two stations.

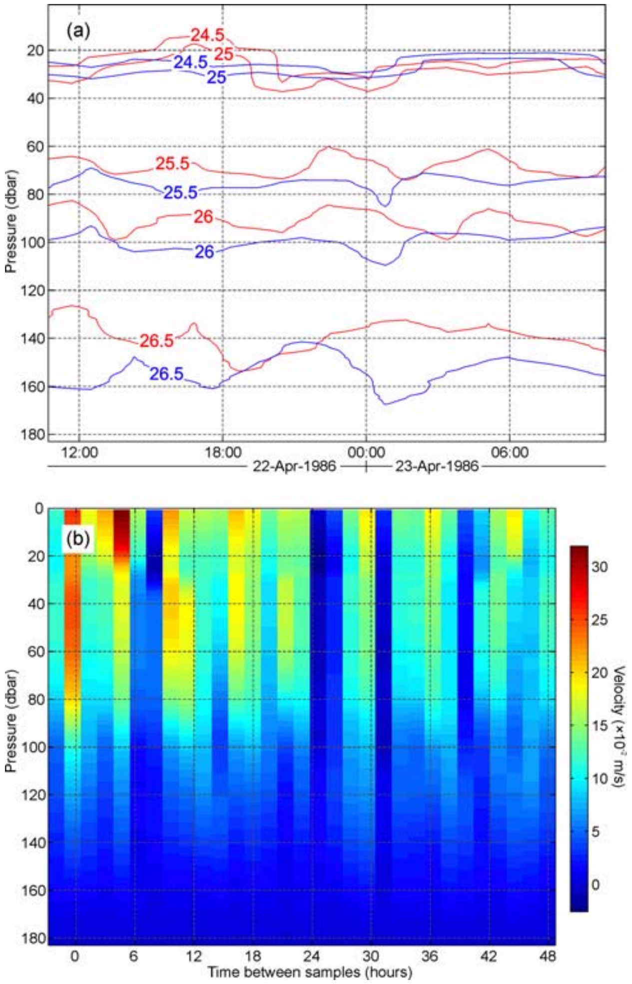

Figure 5.1.4. Winter (November to March) and summer (April to October) averages of geostrophic velocity referenced to 1000 dbar level and σ_t-contours at standard hydrographic cross-sections off Vancouver Island. Standard hydrographic stations are marked with vertical blue lines. The number of geostrophic velocity profiles averaged is shown in white rectangles at the bottom of each plot. The winter plots are absent for the hydrographic lines with missing winter data, such as for Line W below.

(a) Line W

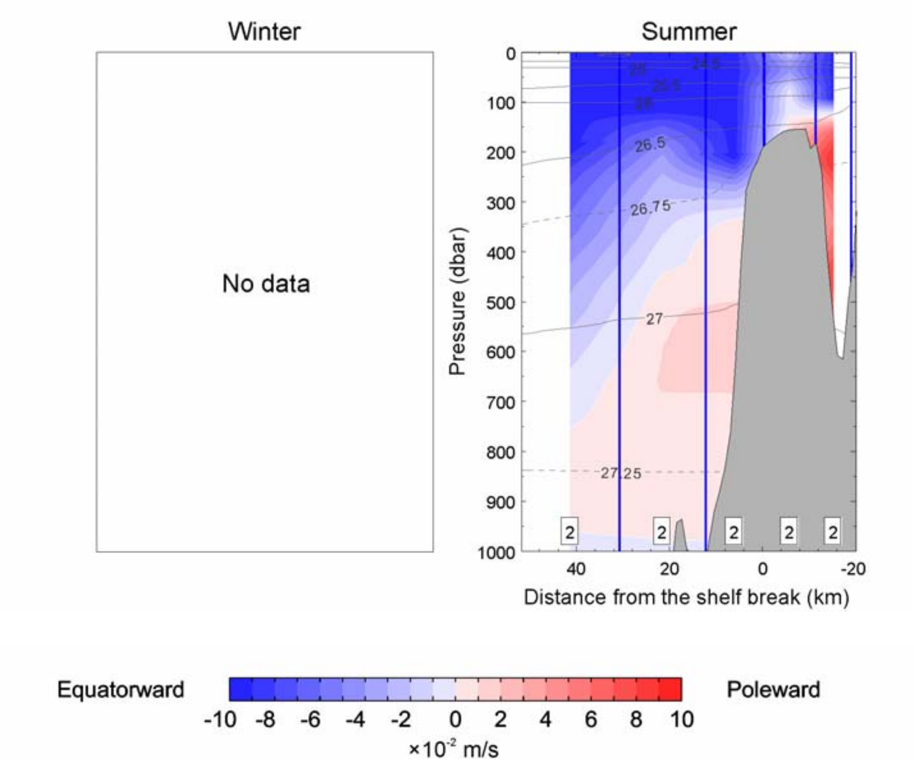

$$\frac{\delta p}{\rho} = \delta\Phi \,, \tag{5.1.13}$$

then the geostrophic balance for v (5.1.5) becomes

$$\frac{\partial\Phi}{\partial x} = fv \tag{5.1.14}$$

The geopotential anomaly, $\Delta\Phi$, between two constant pressure surfaces P_1 and P_2 is a difference between the actual and standard (with temperature T = 0°C and salinity S=35 psu) geopotential between these surfaces. The geopotential anomaly calculated from (5.1.13) as follows:

$$\Delta\Phi = \int_{P_1}^{P_2} \delta dp \,, \tag{5.1.15}$$

where $\delta=\alpha(S,t,p)-\alpha(35,0,p)$ is the specific volume anomaly, which is the difference between the specific volume $\alpha(S,t,p)$ of the water in situ and the specific volume of standard sea water $\alpha(35,0,p)$ (with temperature T=0°C and salinity S=35 psu) at the same pressure. Specific volume $\alpha=1/\rho$ is the inverse of density and is calculated using an empirical *equation of state* for sea water (Millero and Poisson, 1981). The slope of the isobaric surface between stations A and B is then $(\Delta\Phi A-\Delta\Phi B)/L$, where L is the distance between the stations (Figure 5.1.1). The geostrophic velocity is given by (5.1.14) as

$$V = \frac{\Delta\Phi_B - \Delta\Phi_A}{2\Omega L \sin\varphi} \,. \tag{5.1.16}$$

Here, V is a velocity at the surface P_2 relative to the velocity at P_1, or the velocity shear between P_1 and P_2. To obtain an estimate of the absolute velocity it is necessary to calculate velocity relative to some reference level at which the velocity is known. The reference level can be the sea surface where the geostrophic currents are calculated based on satellite altimetry. The calculated velocity profile can also be referenced to a directly measured velocity. Another commonly used approach is to select the reference level deep enough so that the flow can be assumed zero at that depth, commonly referred to as the "depth of no motion" (DNM).

The assumptions outlined above imply that the geostrophic approximation can be used to calculate currents outside the bottom and surface boundary layers (to satisfy the assumption of no friction), for horizontal distances between stations on the order of 10 km, and for time scales of several days. These conditions are satisfied for the general circulation features in the open ocean. The method has also been successfully used to investigate circulation over the region of the continental slope (cf., Helland-Hansen, 1934; Montgomery, 1941; Sturges, 1967; Reid and Mantyla, 1976).

Table 5.1.1. Approximate half-width of the 95%-confidence interval for the mean of a sinusoidal signal inferred from N randomly sampled values.

Depth (m)	Signal amplitude	N		
		20	30	50
50	10	3.16	2.58	2.00
100	5	1.58	1.29	1.00

(b) Line B

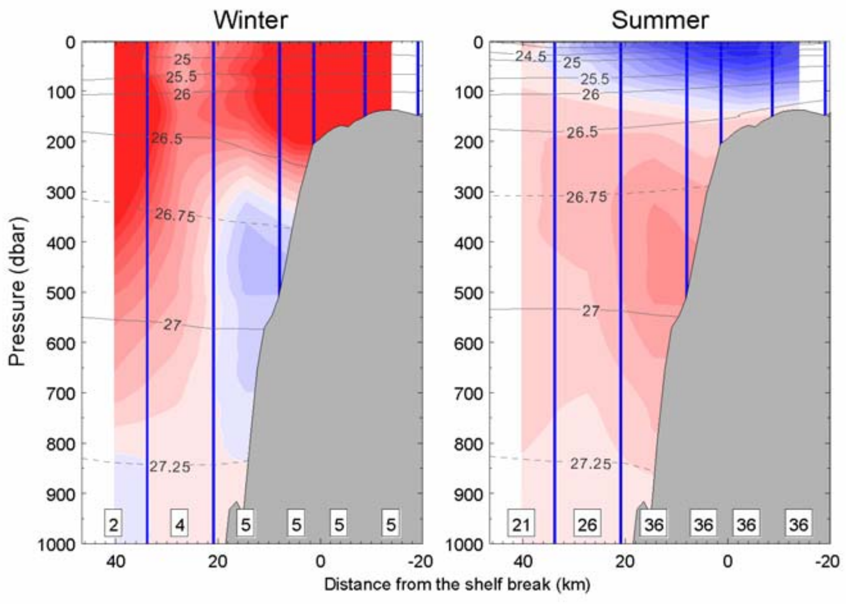

(c) Line C

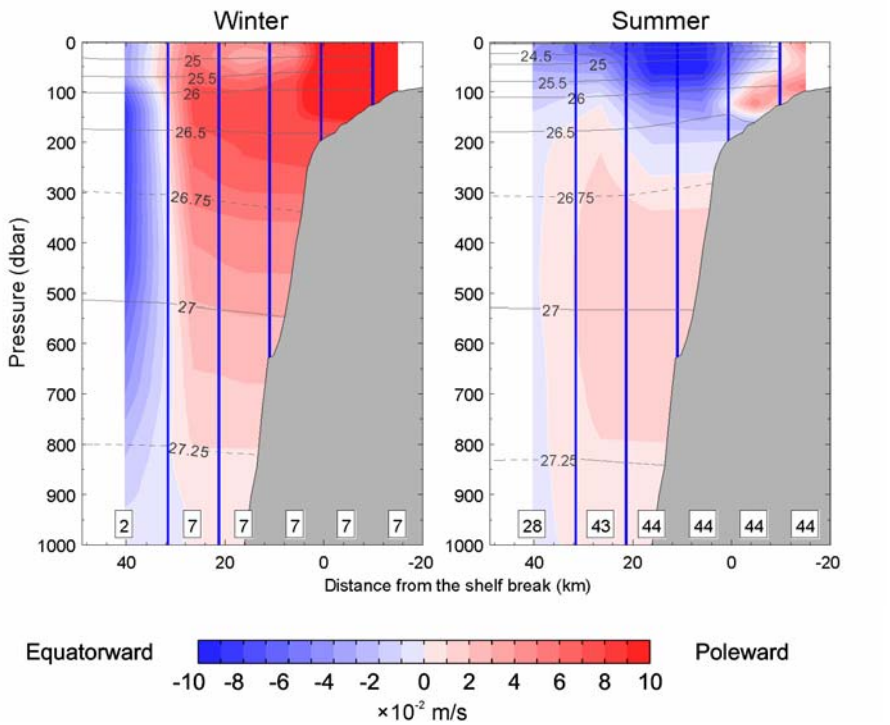

Selection of the reference level and extrapolation onto the shelf

Practical considerations and availability of data make the DNM the most convenient choice for a reference level. It is difficult (if at all possible) to find a uniform and constant level with no current for the dynamically active area over the shelf and slope. However, below approximately 600 m depth, the measured velocities are usually small (Thomson and Gower, 1998) and using a level below this depth as the DNM seems to be a reasonable approximation since the calculated velocities in the upper part of the water column are expected to be much higher than the usual velocities at the assumed DNM.

In this study, I set the reference level at 1000 dbar. The choice was dictated primarily by the availability of data (the data used in this study are described later): there are few sections that extend much below this depth. Also, setting the DNM deeper would require a considerable onshore extrapolation from the deeper parts which would introduce higher uncertainty of the estimates for the upper slope region. The choice is justified by the isopycnal structure of the examined cross-sections: below 1000 dbar, the isopycnals have much more gradual slope in comparison to the density structure above. To examine the sensitivity of the calculations on the choice of the DNM, I calculated currents assuming the DNM to be at the 500 dbar level and at the 2000 dbar level for those few sections where it was possible. Except for slightly higher velocities, calculations with respect to the 2000 dbar reference level show little difference in the vertical and horizontal structure of the flow compared to flow estimated using a 1000 dbar level. This indicates that small velocity shear usually exists below the 1000 dbar surface, but it is largely uniform in the onshore direction, and therefore does not distort the horizontal picture of the derived flow. On the other hand, calculations with respect to a 500 dbar reference level produce a highly distorted flow structure compared with that

(d) Line E

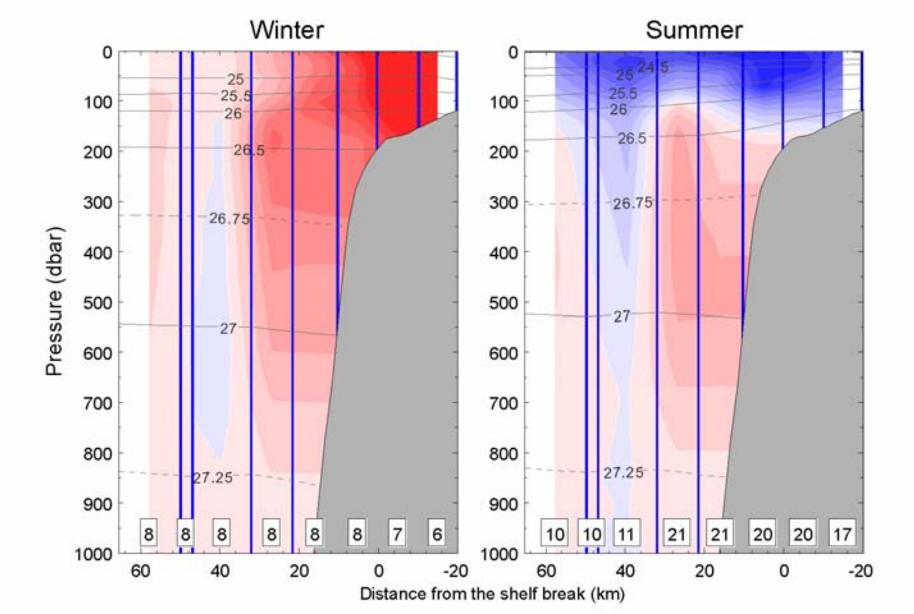

(e) Line G

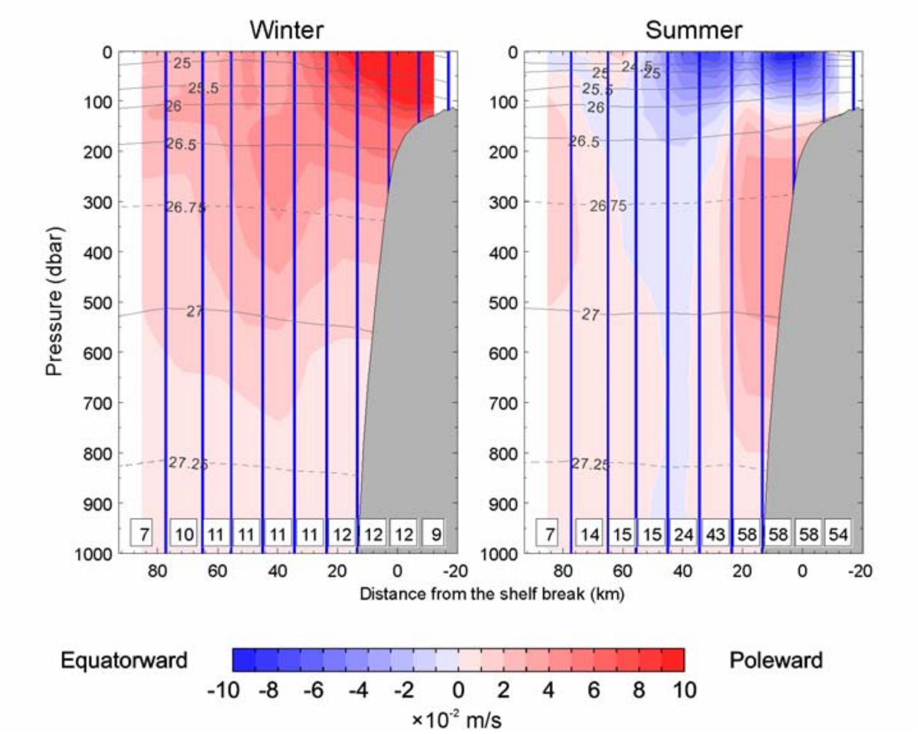

referenced to the 1000 dbar level. This test shows that the 1000 dbar surface is a reasonable choice for the reference level for this area, although it may slightly underestimate the alongshore velocities. In addition, the good correspondence with the current meter data (discussed below in more detail) indicates that the errors associated with the choice of the DNM are not large in most cases. Other researchers have also found a good correspondence of calculated and observed velocities when using 1000 dbar as a reference level for the region off the west coast of North America (Sturges, 1967; Reid and Mantyla, 1976).

To extrapolate geostrophic velocity to regions where the water depth is less than the DNM, it was necessary to extrapolate the density structure onshore. Two simple methods have been widely used for the onshore extrapolation (Helland-Hansen, 1934; Montgomery, 1941). Helland-Hansen (1934) assumed a horizontally uniform density distribution in the missing parts of the section (isopycnals are extrapolated as horizontal lines), which implies zero vertical shear below the bottom and, therefore, zero geostrophic velocity at the bottom. Montgomery (1941) allowed a horizontal density gradient in the extrapolated part. He assumed the isopycnal slope to be the same as at the nearest available pair of stations. The method was subsequently validated by comparison of the calculated steric height with the coastal sea level observations for the west coast of North America by Sturges (1967). The method was used in a number of other studies (e.g. Reid and Mantyla, 1976; Hickey, 1989b). Reid and Mantyla (1976) found the results obtained with Montgomery's method in better agreement with direct current measurements and sea level observations than those obtained with Helland-Hansen's method. They essentially used Montgomery's method, but extrapolated the density structure based on the horizontal density gradient rather than the isopycnal slope, which is equivalent to an assumption of a horizontally uniform distribution of velocity in the extrapolated part as

(f) Line K

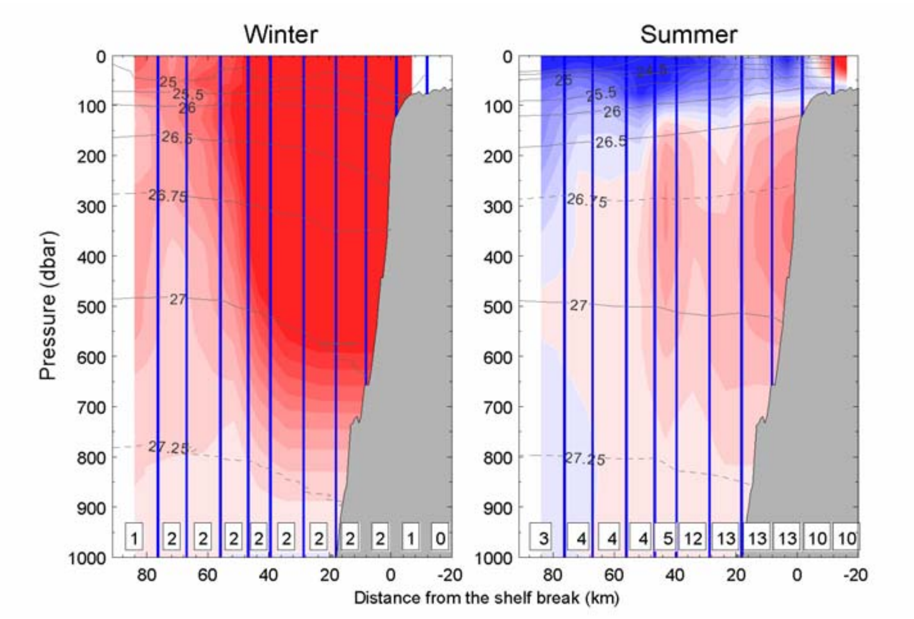

(g) Line BP

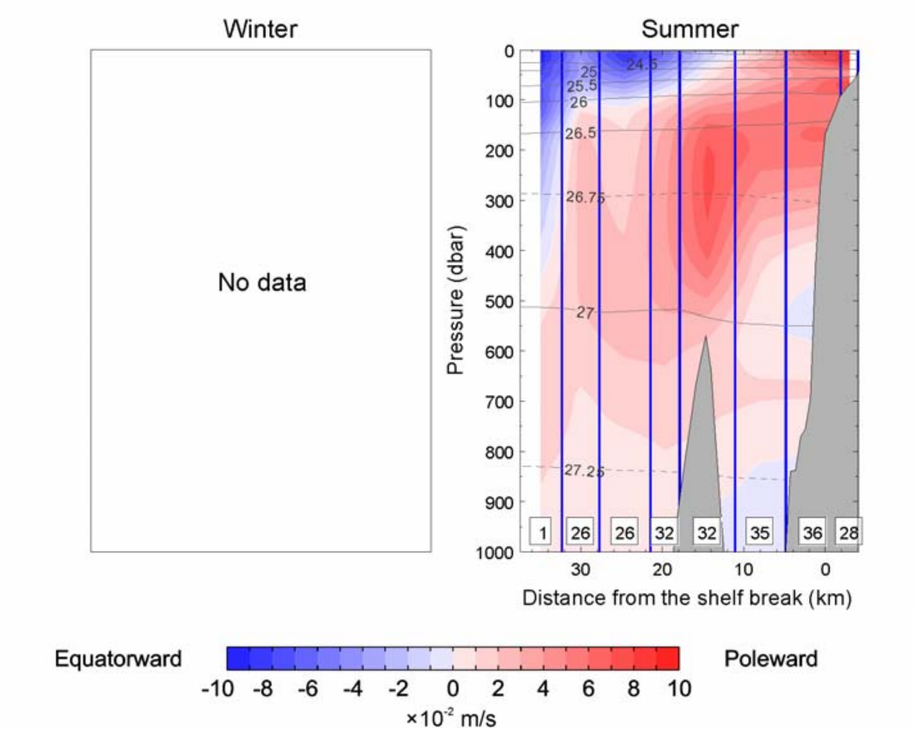

opposed to the horizontally uniform distribution of density assumed by Helland-Hansen. In this study I use the method adopted by Reid and Mantyla (1976).

Bennett (1959) proposed a method to extend shallow profiles to the desirable depth assuming the density in the deep parts of all profiles should be the same. He used a linear interpolation between the deepest part of the shallower profile and the deepest part of the deeper profile in ρ-z coordinates with logarithmic z axis. This approach works only for sufficiently deep profiles. The shape of the extrapolated part depends largely on the depth of the profile thus producing excessively large horizontal gradients between pairs of profiles with significantly different depths which leads to unrealistically strong currents. Therefore, the method is not applicable for the shelf-slope region. There have also been attempts to use empirical orthogonal functions of horizontal density at different depths to formulate the onshore extrapolation (Pedder and Gomis, 1997), but this method requires highly temporally and spatially resolved hydrographic measurements, i.e. suitable only for extensive hydrographic surveys of specific areas. I will not consider this approach in this study.

The data

The hydrographic dataset introduced in the previous section (Figure 4.3.3) was used to calculate the along-shore geostrophic velocity. According to the onshore density extrapolation scheme described above, at least two profiles in a section have to be sampled down to the depth of the prescribed DNM. Sections that did not meet this requirement were ignored. For example, Line A had been extensively sampled but mostly to a depth of about 900 m (Station LA10) with the next deepest station being in 350 m of water depth. Only once did Line A have two profiles sampled deeper than 1000 m and, therefore, only one section of geostrophic velocity was calculated for this line. To get the most

(h) Line N

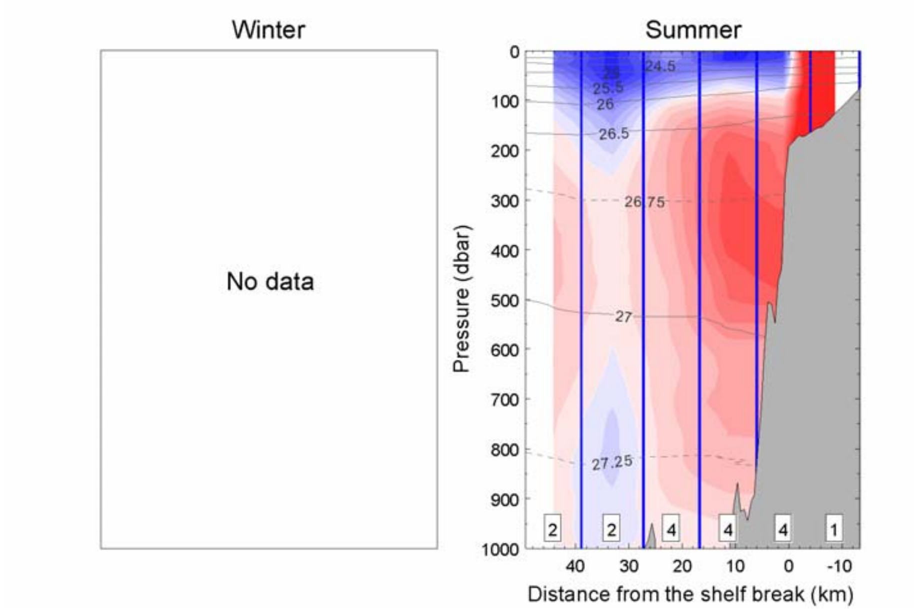

(i) Line T

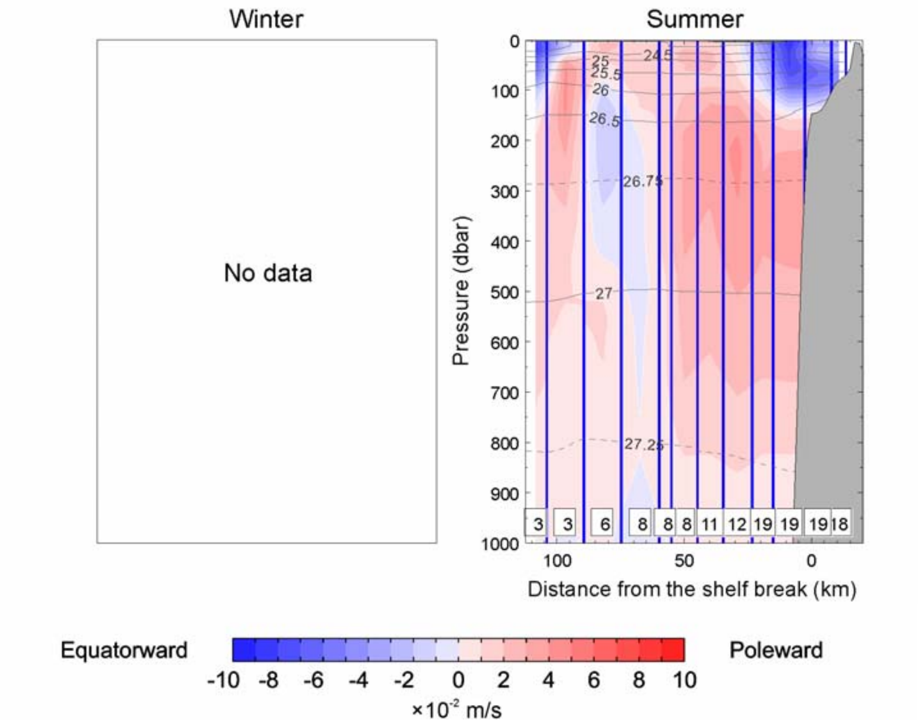

information out of the available data, the profiles which extended to within 200 m of the DNM were linearly extrapolated to the DNM based on the overlying shape of the profile. Since the vertical variations of density are not abrupt and well predictable below 800 m depth, such a vertical extrapolation approach seems justified. In total, 293 individual velocity cross-sections were obtained. All data used for calculations were collected between 1979 and 2005.

Influence of internal tides

Vertical displacements due to internal tides are strong in the region of the continental slope off Vancouver Island, particularly in summer due to increased stratification (Section 4.1). As a result, the instantaneous cross-shore density distribution can differ considerably from the average seasonal picture. The geostrophic velocity estimated for one particular cross-section, therefore, can have a considerable component arising from the presence of internal waves superimposed on the average flow. The situation is further complicated because the sampling of a hydrographic section is not performed instantaneously. For those cross-sections examined, the time interval between measurements at adjacent stations is usually the order of an hour. The entire section, therefore, is sampled in approximately 6 to 12 hours, the time interval comparable to the period of internal wave displacements at semidiurnal frequency. Therefore, to estimate an average seasonal density structure and corresponding geostrophic velocity a sufficiently large number of cross-sections sampled throughout the season (particularly for the summer season) should be averaged.

To examine the dependence of calculated geostrophic velocity on the time interval between measurements at two stations and the amplitude of isopycnal excursions at diurnal and higher frequencies, I used time series of hydrographic profiles sampled at 1.5 – 2.5 hour intervals at two locations on Line C on

Figure 5.1.5. Schematic cross-shore sections summarizing seasonal circulation features on the continental slope off Vancouver Island. The average seasonal isopycnal structure is shown with grey lines. Poleward and equatorward flows are shaded with red and blue, respectively. The main features shown are the seasonally reversing Shelf-break Current/Davidson Current (DC) or Northeast Pacific Coastal Current and the California Undercurrent (CUC). Average seasonal core velocities as determined by geostrophic velocity calculations are also shown. Blue stripes show possible winter reversal of the Undercurrent to the equatorward direction at depths below 350 m.

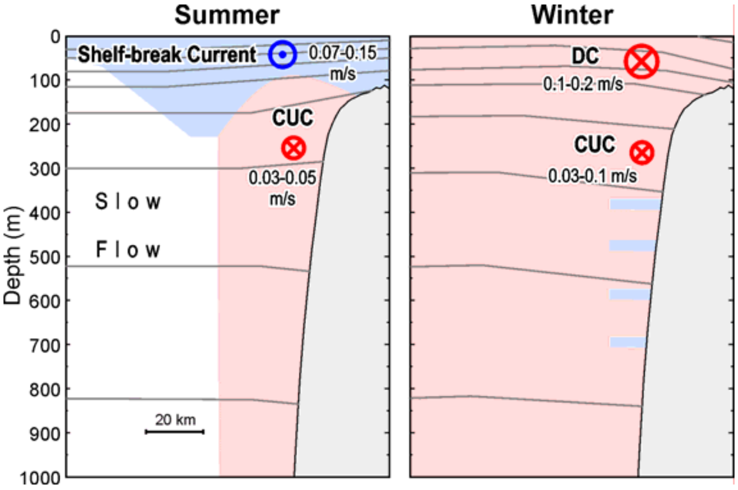

April 22 – 24, 1986. One of the stations was located at the shelf break in a water depth of 200 m, the other 10 km seaward on the slope in a water depth of 600 m. Six-hourly oscillations are the most pronounced feature of the density anomaly, σ_t, in a time-depth plot (Figure 5.1.3a). The vertical excursions of the isopycnal surfaces are maximum (around 20 m) at 60-100 m depth, the depth range of greatest mean vertical density gradient (the pycnocline). The density changes by 0.4 kg/m^3 during six hours between the extrema of the six-hourly cycle. Geostrophic velocity calculated between the two stations for different time lag between the observations at the two hydrographic stations shows considerable variability in the upper 100 m of the water column (Figure 5.1.3b). The strongest is the six-hourly cycle with extreme variations of velocity of the order of 0.1 m/s at 50 m depth and 0.05 m/s at 100 m depth. Below the pycnocline, the variations are much smaller (around 0.01 m/s at 175 m depth). The above estimates of variability give an estimate of the largest deviations at tidal frequencies. Stations S1 and S2 are close to the shelf break, where the internal tides should be the strongest, therefore the variance at other locations, further offshore should be lower. Table 5.1.1 gives approximate 95% confidence intervals for the mean of a sinusoidal signal with amplitudes 0.05 and 0.1 m/s, characteristic of the variability of the velocity estimates at 100 and 50 m depths, respectively, sampled at N random moments in time. The confidence intervals from the table should give an estimate of the accuracy of mean summer velocity values obtained for the hydrographic cross-sections off Vancouver Island. As noted earlier, the confidence intervals should be smaller for the stations away from the shelf break and in winter.

Features

Seasonal differences in the circulation off Vancouver Island are well documented (e.g. Thomson and Ware, 1996). To allow for this, the hydrographic data were divided into summer and winter seasons separated approximately by the time of the spring and fall oceanic transitions (Section 5.2). The data collected from April through October and from November through March were used to determine the summer and winter seasonal values, respectively.

All sections show distinct summer and winter pictures in the mean density structure above the continental slope. In summer, the isopycnals tilt upward in the shoreward direction in the surface layer and downward in the lower layer. In winter, the isopycnals are tilted downward in the shoreward direction at all depths. Such seasonal mean isopycnal structure would support a summer poleward geostrophic flow just seaward of the shelf break with a subsurface maximum at 150-400 m depth and winter poleward geostrophic flow from surface to bottom with the maximum at the surface independent of the choice of the reference level. Also, vertical extrema of the velocity profile would be preserved if a barotropic (vertically uniform) flow were superimposed on the baroclinic flow. Both the winter and summer density structures are consistent from one section to another along the entire coast of Vancouver Island.

In accordance with the seasonal mean density distribution, the calculated geostrophic currents show distinct summer and winter flow regimes. All averaged winter sections show a poleward flow at all depths that is horizontally uniform above the slope (Figure 5.1.4, left-hand plots). Strongest winter flow is at the surface and there is either no detectable subsurface maximum or only a very weak secondary maximum between 100 and 300 m depth. This surface-intensified poleward flow can be considered an extension of the Davidson Current formed in winter over the continental slope from northern California to southern British Columbia (Hickey, 1979) and a part of the Northeast Pacific Coastal Current (Thomson and Gower, 1998). Winter data are absent north of Line K off Kyuquot Sound. Two hydrographic lines (Lines B and D) indicate a reversal of the undercurrent (found in summer transects and discussed below) in the average winter flow. Line B (Figure 5.1.4b) and Line D (not shown because of few winter samples) show an equatorward undercurrent adjacent to the slope at depths of 300-800 m with the core around 450 m depth and maximum equatorward velocity > 0.02 m/s. However, winter data are scarce (only five sections were available for Line B and two sections for Line D) and the existence of this feature cannot be reliably established from the available data.

The main features of the summer velocity transects include a subsurface poleward undercurrent strongest during summer - early spring and a surface-intensified equatorward flow within the upper 100-200 m above the slope and also at greater depths further seaward of the shelf break (Figure 5.1.4, right-hand plots). The averaged sections indicate the presence of an undercurrent at all hydrographic lines along the coast of Vancouver Island. The vertical and cross-shore location of the undercurrent indicates

Figure 5.1.6. Along-shore current velocity calculated using hydrographic data (V_{gv}) versus measured velocity (V_{cm}). Summer and winter values are denoted with red and blue circles, respectively. The coefficient of determination (r^2) and the principal component axis and its slope are also shown.

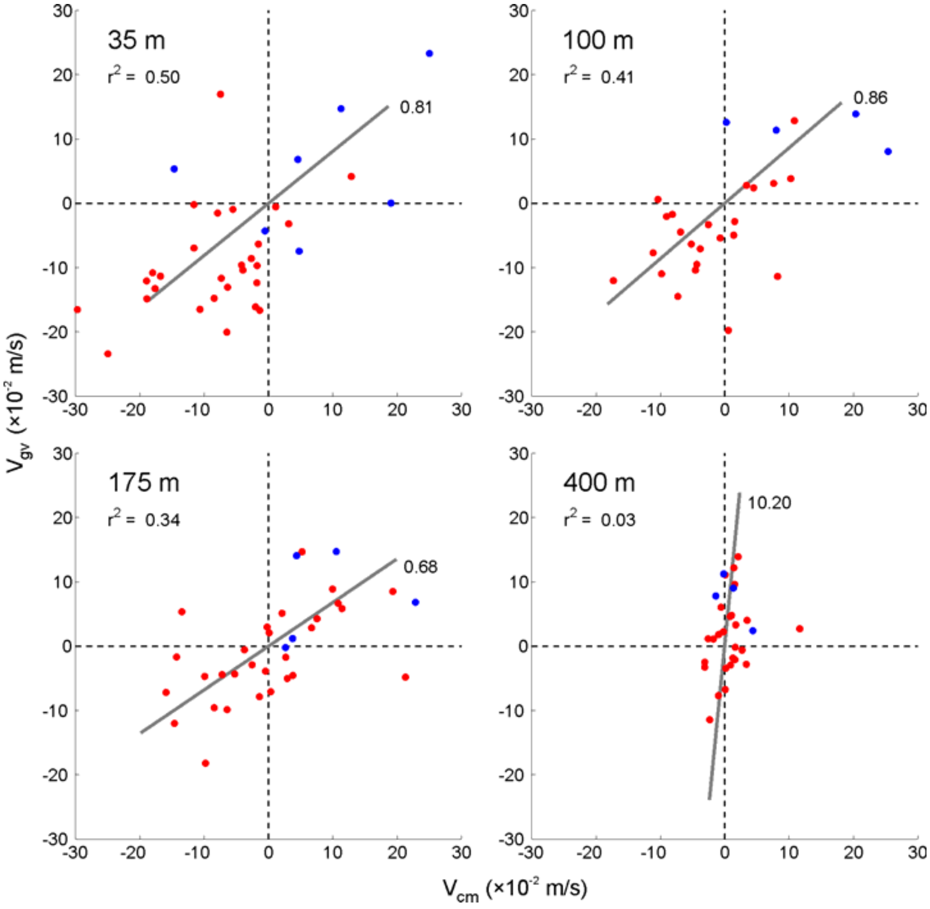

that it is an extension of the California Undercurrent with an equatorward shelf-break current in the upper layer and California Current further offshore. In the cross-shore direction, the core of the Undercurrent is observed over the slope roughly 20-30 km seaward of the shelf break (cf., Hickey *et al.*, 1991). Off southern Vancouver Island, the maximum poleward velocity is near 500 m depth (Lines B and C in Figure 5.1.4). The core shoals further to the north with maximum poleward velocity at 200 m depth at Line T. The data suggest that the poleward Undercurrent intensifies to the north, average core velocities being 0.02 to 0.05 m/s at Lines B, C, E, and G, and 0.05 to 0.07 m/s at Lines K, BP, and N. At the northernmost of the examined hydrographic lines, Line T, the poleward flow has weakened. The sections off northern Vancouver Island also indicate surfacing of the summer poleward flow. At Lines BP, M, and T the flow either extends to the surface or is present at depths as shallow as 50-100 m. Along-shore changes in the isopycnal structure and corresponding baroclinic flow are apparently connected to the strength of the upwelling winds, which become weaker to the north, closer to the point where prevailing summer winds transition from

Table 5.2.1. Fourier analysis of the mean annual cycle of alongshore current at Station A1. Shown is the percentage of variance explained (var %), the amplitude (A, $\times 10^{-2}$ m/s), and the phase lead of the peak positive value relative to 0000 UTC on January 1st (φ, in degrees) for each Fourier constituent. The 0th component is the mean flow (positive is the poleward direction). HF denotes all constituents with frequencies higher than 6 cycles per year (cpy).

Frequency (cpy)	35 m			100 m			175 m			400 m		
	var %	A	φ	var %	A	φ	var %	A	φ	var %	A	φ
0		-1.0			2.3			3.5			0.6	
1	90.6	14.1	-10	84.4	9.8	15	44.3	5.8	45	19.1	0.8	127
2	2.5	2.3	-46	2.8	1.8	-38	3.9	1.7	35	2.9	0.3	-15
3	1.4	1.8	-54	1.5	1.3	-72	0.5	0.6	61	0.6	0.1	-81
4	0.1	0.5	112	0.4	0.7	-165	7.1	2.3	-95	4.3	0.4	125
5	0.2	0.6	17	0.8	0.9	61	2.8	1.5	99	0.3	0.1	7
6	0.1	0.5	55	0.1	0.2	128	0.4	0.6	-99	4.5	0.4	-19
HF	5.1			10.0			41.0			68.2		

Figure 5.2.1. Mean annual cycle of (a) the alongshore wind, (b) the alongshore component of flow at different depths at Station A1, and (c) the mean-removed sea level at Tofino adjusted for the inverse barometer effect.

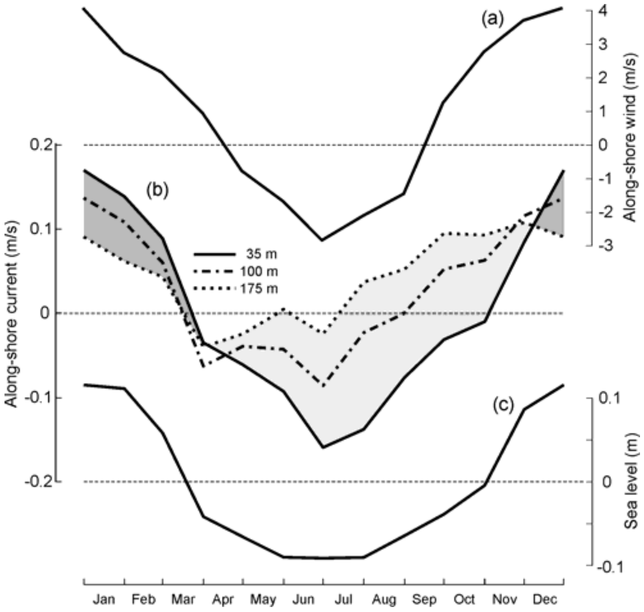

predominantly equatorward to predominantly poleward (see Section 2.1 and Figure 2.1.2).

The along-shore geostrophic velocities estimated for individual cross-sections can deviate considerably from the seasonal means. Nevertheless, there is a remarkable consistency in the main features of the seasonally averaged velocity field from one line to another along the coast (even for winter, when the data are much scarcer than in summer), indicating that these are real features. This circulation pattern is also supported by the mean isopycnal structure regardless of the choice of the reference level. The above seasonal features are summarized in schematic cross-sections in Figure 5.1.5.

Comparison to the current meter data

The geostrophic velocity at Line C (closest to Station A1) was compared to the measured current velocity at Station A1. Figure 5.1.6 shows daily (de-tided) values of alongshore (335° clockwise from true north) current velocity at the time of hydrographic measurements at Line C versus geostrophic velocity at Line C at the same bottom depth (500 m) as current meter deployment. For all instruments except the one at 400 m depth the correlation, *r*, between measured and calculated current is significant at the 99% confidence level. The correlation at 400 m depth is significant only at 64%. As discussed in Section 3.1, currents at the 400 m instrument at Station A1 were affected by an underwater canyon causing along-shore flow to be highly attenuated and distorted in comparison with the flow outside of the canyon where Line C is located. The coefficient of determination, r^2, shows that from 34 to 50% of the total variance in the currents measured by the upper three instruments is explained by calculated (baroclinic) currents. In about half of all cases, the geostrophic velocity departs equally at all depths from the measured currents. In such cases, the discrepancy can be attributed to barotropic flow sensed by current meters or to a non-zero baroclinic flow at the DNM (note that the current meter measures both the baroclinic and barotropic flow while the geostrophic velocity is strictly baroclinic). In cases when the departures vary with depth, the errors may have resulted from internal waves distorting the geostrophic velocity profile and differences in the flow above 500 m isobath at Station A1 and Line C.

Summary

The hydrographic data provide clear evidence that the poleward California Undercurrent extension formed above the upper slope is continuous along the entire west coast of Vancouver Island in summer. In winter, the flow forms a part of the Davidson Current (Northeast Pacific Coastal Current) and is poleward at all depths. The main cross-shore structure features of the seasonally averaged geostrophic currents are preserved along the entire length of Vancouver Island, with the core of the subsurface poleward flow either adjacent to the continental slope or located within 20 km of the shelf break and extending 20 to 50 km off the shelf break. Above the Undercurrent, the flow in the offshore region is equatorward as part of the Shelf-break Current. The core maximum of the poleward velocity (0.03 – 0.07 m/s) in the Undercurrent in summer is at 175 – 400 m depth. For several hydrographic lines off Vancouver Island (particularly for those closer to the southern boundary of the study region), the core is found deeper than the Undercurrent core depth reported for the Washington coast by Hickey (1979). The deepening of the Undercurrent off southern Vancouver Island may be due to modification of the poleward flow by Juan de Fuca Canyon. The velocity changes sign at 100 – 150 m depth. The core depth of the poleward undercurrent as obtained from hydrographic data is determined by the cross-shore isopycnal structure. The cross-shore isopycnal gradient in the upper part of the water column in summer is, in turn, largely determined by the strength of upwelling which may be forced both by both local and remote winds (Hickey *et al.*, 2006). Thus, the depth of the maximum of the baroclinic poleward flow in summer depends on the intensity of the upwelling (on the seasonal time scale rather than on the event scale; Halpern, 1976). The calculated currents agree well with the measured currents indicating the validity of the method of geostrophic velocity calculations. This agreement also confirms that the upper slope currents are largely in geostrophic balance.

5.2. Mean annual cycle

As indicated by the broad-band spectra in Section 4.2 (Figure 4.2.6), the annual cycle is the most energetic component of the current variability at Station A1 down to a depth of at least 175 m. In this section, I explore more closely the characteristics of the annual fluctuations by (1) calculating the mean annual

Figure 5.2.2. Variance of the mean annual cycle and residual (non-seasonal) flow for each depth for the alongshore (left-hand bars) and cross-shore (right-hand bars) components of monthly values of the current at Station A1. The percentage of the variance associated with the alongshore component of the annual cycle is indicated on the corresponding bars. For the cross-shore direction it is around 20% at all depths.

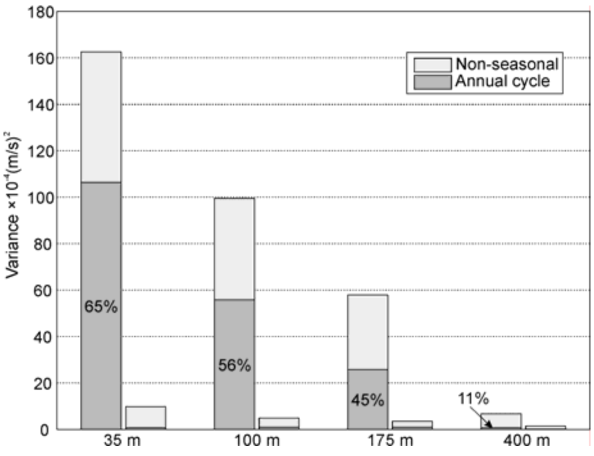

Figure 5.2.3. Monthly values of current components at Station A1, reanalysis wind, and mean-removed sea level at Tofino. Positive values are toward the pole and the shore. The long term monthly mean and standard deviation are shown at the bottom of each plot. Multivariate El Niño Index anomalies (MEI) are shown on the right side for the along-shore velocity component only.

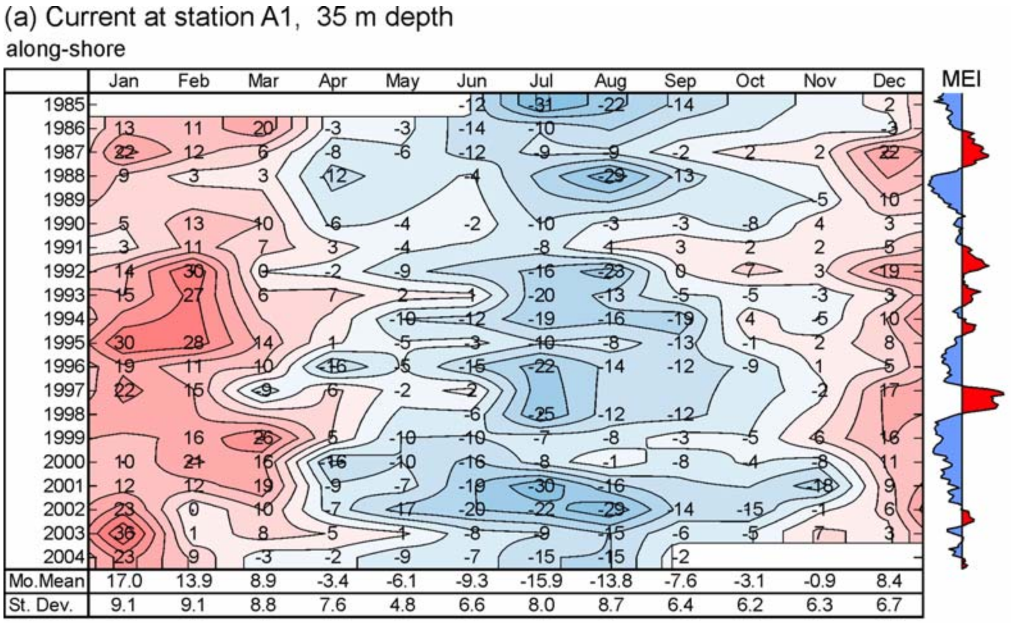

(a) Current at station A1, 35 m depth

along-shore

cross-shore

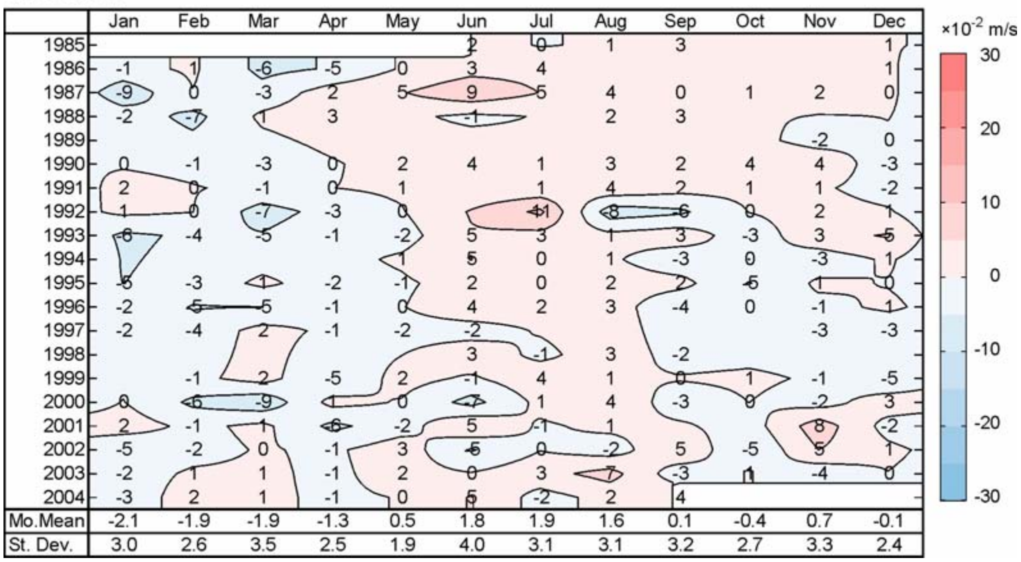

cycle based on monthly values of the A1 currents, the sea level at Tofino, and the wind linearly interpolated between two grid points at 47.5°N and 125.0°W and at 50°N and 127.5°W (Reanalysis data); (2) evaluating the contribution of the annual cycle to the total variance of monthly values of alongshore (335°T) and cross-shore components of the A1 currents; (3) performing a harmonic analysis of the mean annual cycle; and (4) exploring interannual variability of the annual cycle.

Mean annual cycle of wind, sea level, and current

The mean annual cycles (long-term average monthly values) for the alongshore component of the A1 currents at the three upper nominal depths, as well as for the sea level and alongshore wind, are shown in Figure 5.2.1. The monthly series were obtained from the daily series (Section 4.1) by low-pass filtering with a 40-day cutoff with subsequent decimation to monthly values. The annual cycle of the wind has winter and summer extrema with the strongest poleward wind in February and the strongest equatorward wind in July. Changes in the prevailing wind directions occur in April and September. The alongshore current undergoes seasonal changes similar to the wind, although during the spring transition (corresponding to a change in prevailing current direction), the current changes sign about one month earlier than the wind (in March – April at all depths). A similar lead of the current with respect to the wind is observed along the entire North American west coast from southern California to southern British Columbia (Strub *et al.*, 1987b). However, the return to poleward flow occurs at different times for different depths because the mean current changes with depth. Based on the observations at 35 m depth, the fall transition occurs in November; at 100 m depth, it occurs in September; and at 175 m depth, the current changes direction in July. Figure 5.2.3 indicates, however, that for individual years, the fall transition can lead or lag the above long-term averages by as much as three

Figure 5.2.3. (continued)

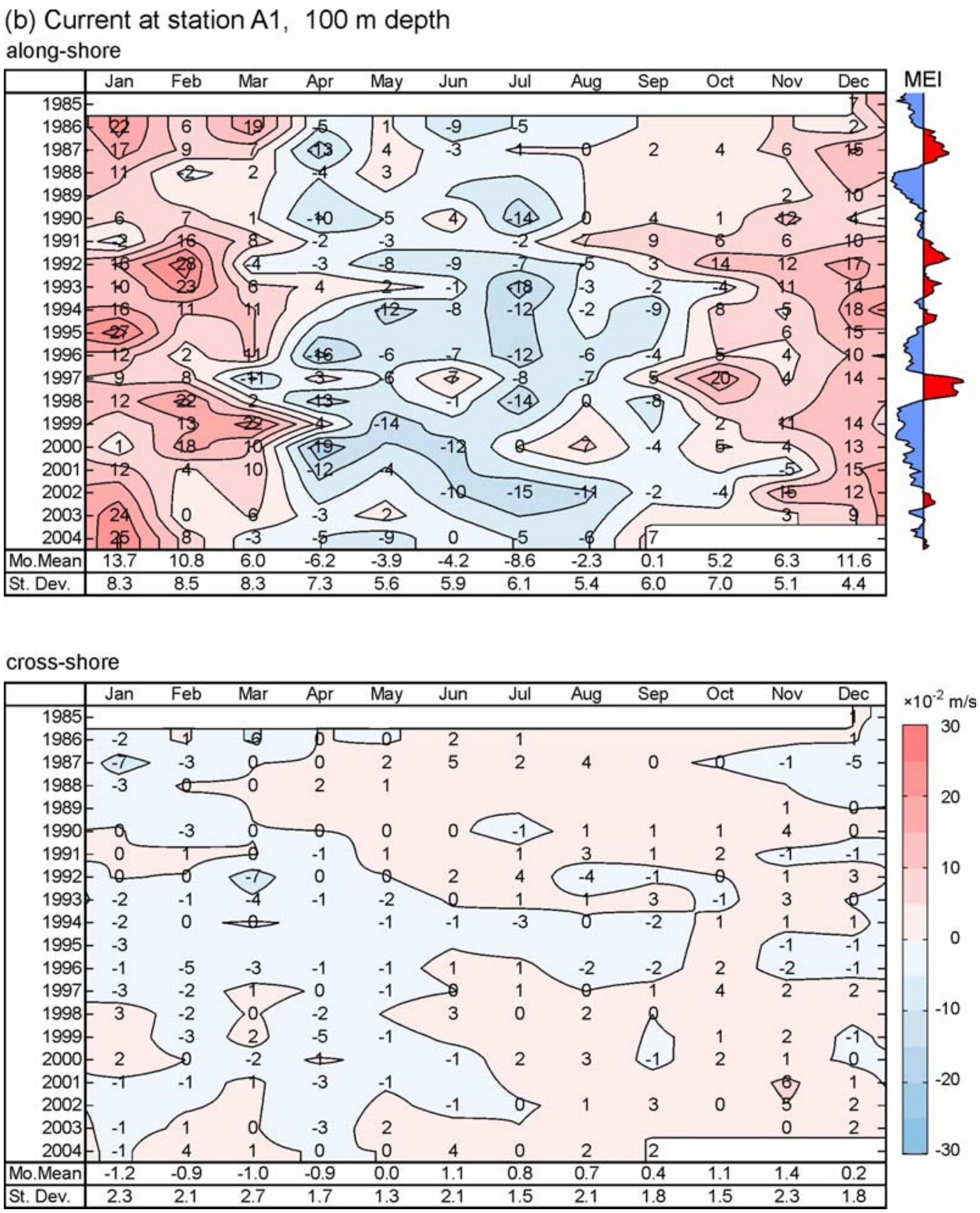

months, while the flow at 175 m can be poleward throughout the year with the exception of one month in late spring (e.g. 1987 and 1995). During most of the year, the vertical shear, dv/dz, of the alongshore flow is negative (deeper layers have a stronger poleward component than the overlying layer), which is typical of flow in the CUC (e.g. Hickey, 1979). The vertical shear is negative from March (the time of the spring transition) to December with a maximum in July – August. In winter, the vertical shear is positive apparently due to the stronger response of the upper layers than lower layers to the seasonally changing winds, which blow in the poleward direction during winter months. In July – October, the current at 175 m is in the opposite direction to the current at 35 m, and in July – August, the 100 m flow is opposite to the 35 m flow. The main maximum in the poleward flow at all depths is in December – January and is likely due to two factors. In the upper layer, the wind directly forces the current alongshore in the direction of the wind. In the deeper layers, the onshore Ekman transport associated with the poleward wind leads to downwelling, downward tilt of the isopycnals in the shoreward direction, and, by geostrophy, intensification of the poleward flow in the subsurface portion of the water column.

There is a weak secondary peak in the CUC in May – June. It can be seen in deep layers but not in the near-surface layer. This summer peak in the CUC can be traced along the entire West Coast of North America from Baja California to Vancouver Island. As suggested by Hickey (1979), this summer peak decreases to the north. McLain and Thomas (1983) explain the existence of the summer maximum by propagation of the depression of the thermal structure from the Eastern Tropical Pacific along the coast via coastally trapped Kelvin and Rossby waves. Dissipation of these waves along their path would also explain the decrease in amplitude of the summer maximum with latitude.

The contribution of the mean annual cycle to the total variance of monthly values at different depths is presented in Figure 5.2.2. The annual cycle is significant only for the alongshore component. Both the amplitude of the annual cycle

Figure 5.2.3. (continued)

(c) Current at station A1, 175 m depth

along-shore

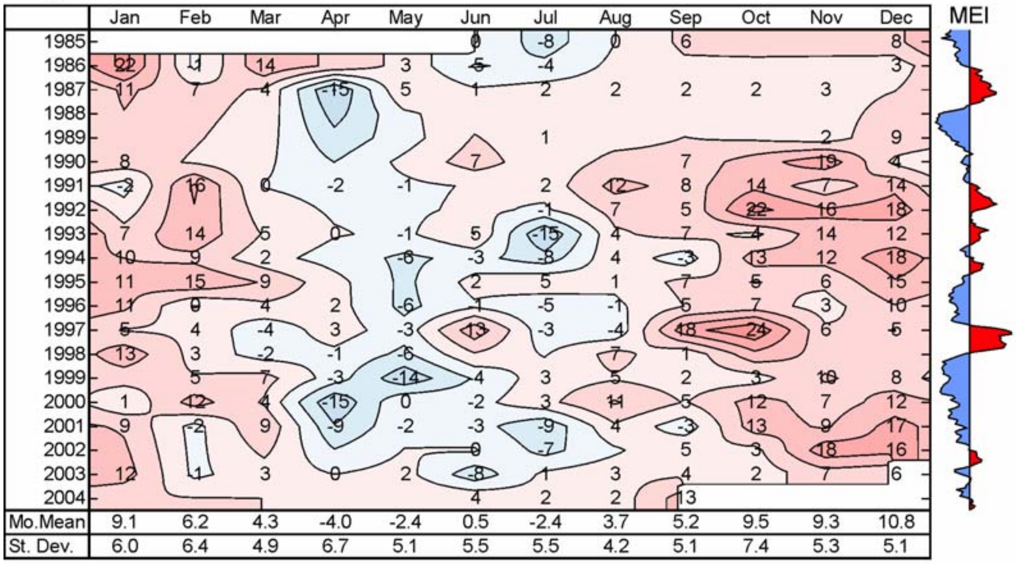

cross-shore

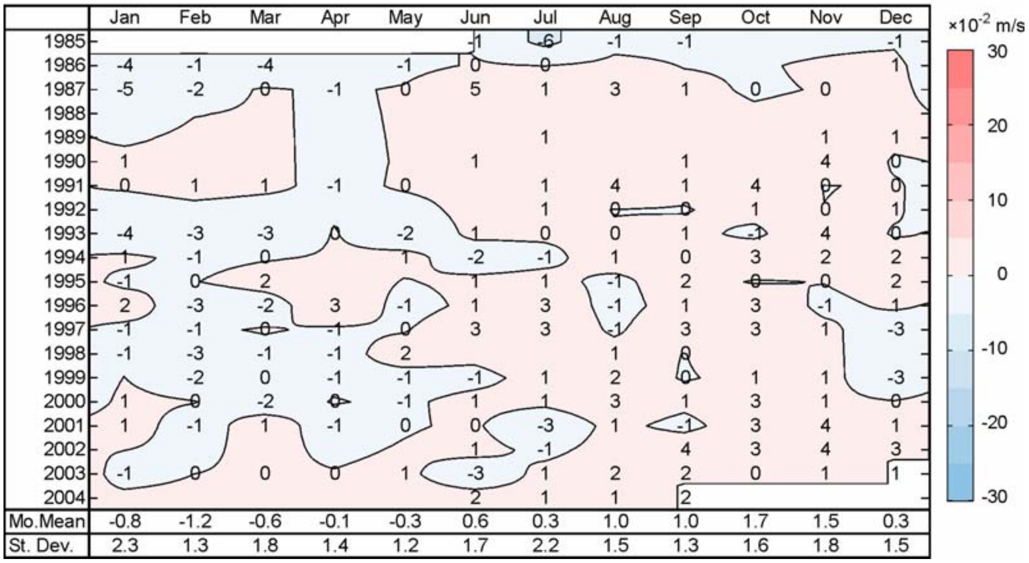

and its contribution to the total variance rapidly decrease with depth (specifically, the absolute variance of the annual cycle decreases roughly by 50% every 70 m while its contribution to the total variance decreases by 10% every 70 m), while the residual variance experiences more gradual decrease with depth. The contribution of the annual cycle to the total variance for the cross-shore direction is around 20% at all depths.

Monthly sea level values, together with the surface geostrophic velocity estimated from the hydrographic data, allow estimation of the characteristic width scale of the alongshore currents. The surface alongshore geostrophic velocity depends on the surface slope as

$$v = \frac{g}{f}\frac{\partial \zeta}{\partial x} \approx \frac{g}{f}\frac{\Delta \zeta}{W}, \qquad (5.2.1)$$

where ζ is the height of the sea surface above a surface of constant gravitational potential, x is the coordinate across the shore, and W is the characteristic width scale of the alongshore current (e. g. Stewart, 2003). Solving (5.2.1) yields

$$W \approx \frac{g}{f}\frac{\Delta \zeta}{v}. \qquad (5.2.2)$$

Assuming the offshore sea level changes very little at seasonal time scales (due to the steric effect only and this effect is small), $\Delta\zeta$ is represented by the amplitude of the seasonal variation in the sea level near the shore. Taking $\Delta\zeta$=-0.1 m for the summer and 0.1 m for the winter (extreme monthly values of the sea level at Tofino) and an along-shore geostrophic velocity of 0.07-0.15 m/s in summer and 0.1-0.2 m/s in winter, I estimate W to be about 100-150 km in summer and 50-100 km in winter. Taking the steric effect into account yields larger characteristic widths since steric setup due to warming and freshening of the surface oceanic layer in summer and cooling and increased salinity in winter gives rise to larger amplitude of the sea level change due to the dynamic effect. Seasonal variations in the upper ocean water

Figure 5.2.3. (continued)

(d) Current at station A1, 400 m depth

along-shore

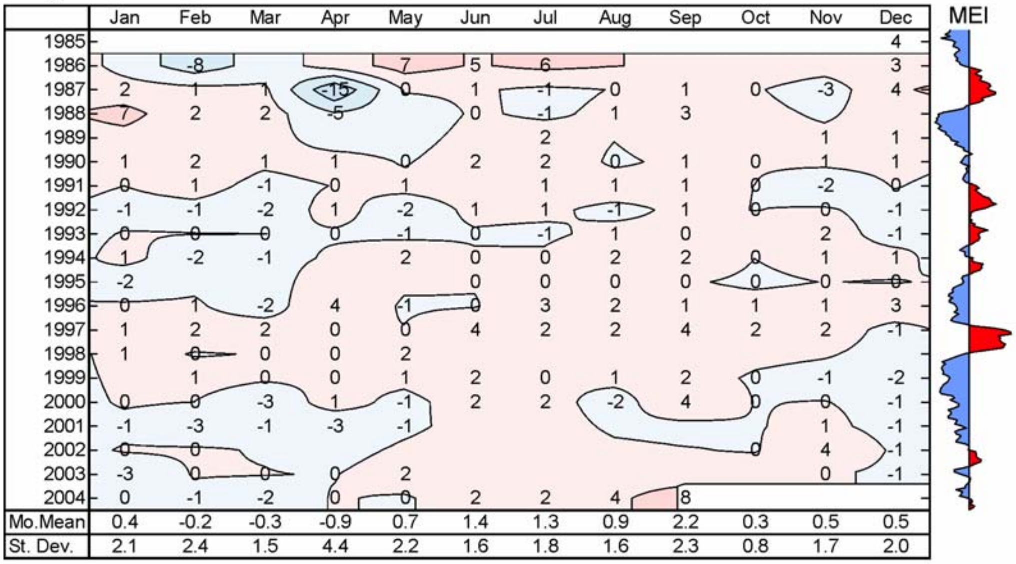

	Jan	Feb	Mar	Apr	May	Jun	Jul	Aug	Sep	Oct	Nov	Dec
1985												4
1986		-8			7	5	6					3
1987	2	1	1	-15	0	1	-1	0	1	0	-3	4
1988	7	2	2	-5		0	-1	1	3			
1989							2				1	1
1990	1	2	1	1	0	2	2	0	1	0	1	1
1991	0	1	-1	0	1		1	1	1	0	-2	0
1992	-1	-1	-2	1	-2	1	1	-1	1	0	0	-1
1993	0	0	0	0	-1	0	-1	1	0		2	-1
1994	1	-2	-1		2	0	0	2	2	0	1	1
1995	-2					0	0	0	0	0	0	0
1996	0	1	-2	4	-1	0	3	2	1	1	1	3
1997	1	2	2	0	0	4	2	2	4	2	2	-1
1998	1	0	0	0	2							
1999		1	0	0	1	2	0	1	2	0	-1	-2
2000	0	0	-3	1	-1	2	2	-2	4	0	0	-1
2001	-1	-3	-1	-3	-1						1	-1
2002	0	0								0	4	-1
2003	-3	0	0	0	2						0	-1
2004	0	-1	-2	0	0	2	2	4	8			
Mo.Mean	0.4	-0.2	-0.3	-0.9	0.7	1.4	1.3	0.9	2.2	0.3	0.5	0.5
St. Dev.	2.1	2.4	1.5	4.4	2.2	1.6	1.8	1.6	2.3	0.8	1.7	2.0

cross-shore

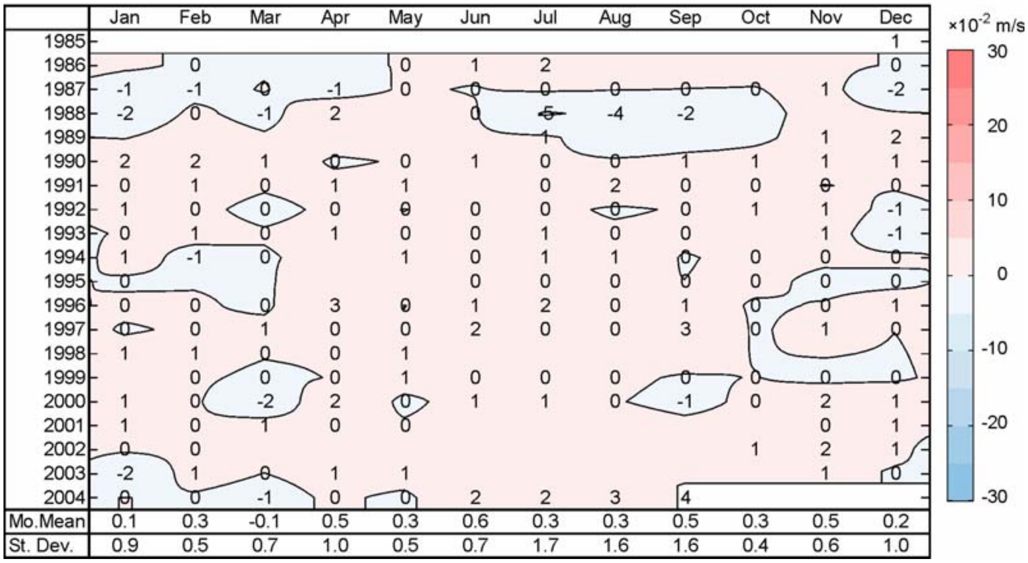

	Jan	Feb	Mar	Apr	May	Jun	Jul	Aug	Sep	Oct	Nov	Dec
1985												1
1986		0			0	1	2					0
1987	-1	-1	0	-1	0	0	0	0	0	0	1	-2
1988	-2	0	-1	2		0	-5	-4	-2			
1989							1				1	2
1990	2	2	1	0	0	1	0	0	1	1	1	1
1991	0	1	0	1	1		0	2	0	0	0	0
1992	1	0	0	0	0	0	0	0	0	1	1	-1
1993	0	1	0	1	0	0	1	0	0		1	-1
1994	1	-1	0		1	0	1	1	0	0	0	0
1995	0					0	0	0	0	0	0	0
1996	0	0	0	3	0	1	2	0	1	0	0	1
1997	0	0	1	0	0	2	0	0	3	0	1	0
1998	1	1	0	0	1							
1999		0	0	0	1	0	0	0	0	0	0	0
2000	1	0	-2	2	0	1	1	0	-1	0	2	1
2001	1	0	1	0	0						0	1
2002	0	0								1	2	1
2003	-2	1	0	1	1						1	0
2004	0	0	-1	0	0	2	2	3	4			
Mo.Mean	0.1	0.3	-0.1	0.5	0.3	0.6	0.3	0.3	0.5	0.3	0.5	0.2
St. Dev.	0.9	0.5	0.7	1.0	0.5	0.7	1.7	1.6	1.6	0.4	0.6	1.0

properties in the region are largely confined to the upper 30 metres. Temperature in this layer typically changes from 9°C in winter to 15°C in summer and salinity typically changes from 32.5 psu in winter to 32 psu in summer. Combined temperature and salinity seasonal steric height difference of the surface layer is then approximately 4.5 cm, temperature variations being responsible for about 75% of the total effect. This adds roughly 20% to $\Delta\zeta$ in (5.2.2) and, therefore, to the characteristic width of the alongshore currents.

Fourier analysis of the mean annual cycle

To investigate the amplitude and phase relationships of the annual cycle at different depths, I performed Fourier analysis of the mean annual cycle calculated based on long-term average daily values. Amplitudes and phases of the Fourier components of the mean annual cycle are presented in Table 5.2.1. The fundamental component (the annual cycle) is dominant near the surface (explaining at least 84% of the variance of the mean annual cycle down to 100 m depth) and quickly diminishes below 100 m depth, where high-frequency noise inputs increasingly large relative amount of energy. The phase shift between 35 and 100 m depth is +25° and between 100 and 175 m depth is +30°, the deeper layers leading the shallower layers. Amplitudes of the first three Fourier components decrease with depth.

Interannual variability of the annual cycle

Tables of monthly values and the mean annual cycle are presented in Figure 5.2.3. The monthly values are organized in tables with one month per column, and contoured to allow exploration of interannual changes in the annual cycle. The annual cycle is the dominant variability pattern in the near-surface layer (35 m depth), while at 175 m depth, interannual variations are also at least as strong as the annual cycle. Two- to six-year variations are clearly identifiable in the alongshore flow down to 175 m depth. Two seasons of strong interannual variations can be defined: late winter – early spring and late fall. The former is more pronounced in the near-surface layer and the latter is strongest at 175 m. Interannual variations at 175 m depth seem to be influenced by the ENSO cycle (Figure 5.2.3c). Stronger poleward flow in summer and fall was observed during

Figure 5.2.3. (continued)

(e) Reanalysis wind

along-shore

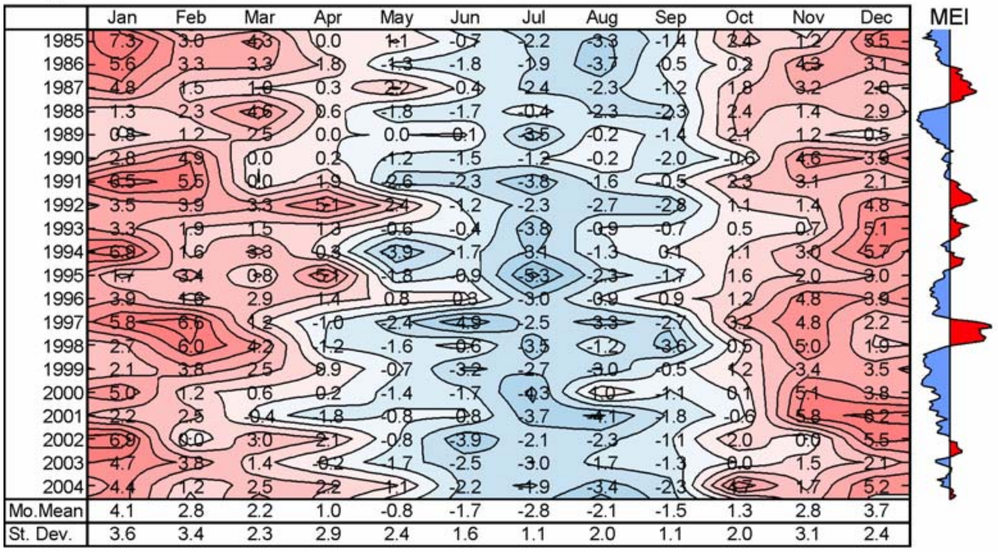

cross-shore

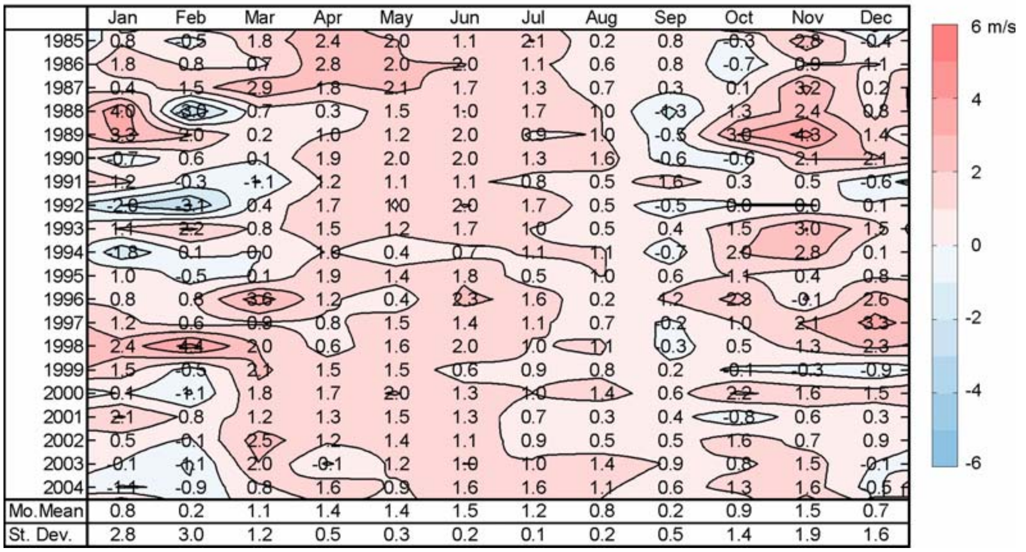

periods of positive Multivariate El Niño Index (MEI) anomalies, i.e. during El Niño events, while stronger equatorward flow was observed during negative MEI anomalies (La Niña events). A similar correspondence between El Niño anomalies and the surface geostrophic flow relative to the 500 dbar pressure surface in the region off Baja California and California had been observed by Chelton *et al.* (1982). The near-surface flow at Station A1 is less correlated with the ENSO signal than the flow at 175 m depth. The variability at 100 m depth represents a transition between the near-surface and subsurface patterns. The cross-shore flow is weak at all depths. However, an annual cycle can be seen, with onshore flow in summer and fall (period of upwelling winds) and offshore flow in winter and spring (period of downwelling winds). Interannual changes decrease in amplitude with depth. Anomalies of the cross-shore flow are not consistent between layers. At 400 m depth, both the alongshore and cross-shore flow are weak with no apparent annual or interannual pattern. The coastal wind has relatively high-frequency interannual variations with anomalies lasting mostly one to two years (Figure 5.2.3e). The annual cycle is strong, although the timing of spring transition in wind differs considerably from year to year. The sea level at Tofino undergoes distinct interannual variations on a scale of 5 to 6 years. Interannual changes in sea level apparently have strong connection to the ENSO cycle (Figure 5.2.3f) and associated with poleward propagation of Kelvin waves generated in the equatorial region (Clarke and Van Gorder, 1994). Winter months have greater interannual variability in sea level than summer months with maximum variability in February.

Summary

The above analysis shows that the alongshore wind and current down to 175 m depth, as well as the sea level, undergo a significant seasonal change with distinct winter and summer regimes and spring and fall transitions. The strength and relative importance of the annual cycle in the alongshore flow decrease with depth. Both the amplitude and the phase of the annual cycle are subject to strong interannual variations on the scale of one to six years. The subsurface alongshore current and sea level appear to have higher correlation with the ENSO cycle than the near-

Figure 5.2.3. (continued)

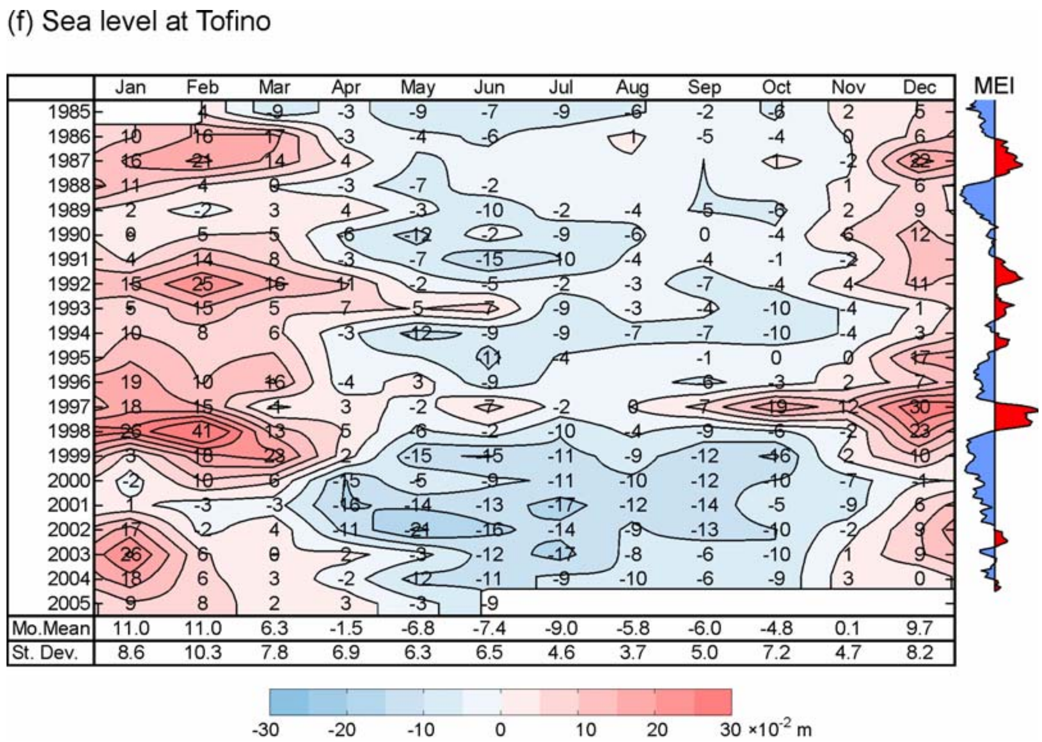

(f) Sea level at Tofino

surface current and the wind. In the next section, the relation between anomalies (non-seasonal part) of the wind, sea level, current, and major climate indices will be examined in more detail.

5.3. Forcing and modification of the slope currents off Vancouver Island

Forcing

In Section 2.3, I reviewed the physical processes which may be responsible for driving and modifying the CUC. In this section, I derive time series representing those forcing factors and establish relationship between the current and the proposed driving factors.

The current variability has been divided into an annual cycle and three broad frequency bands. The annual cycle was determined as the record average value for each day or month of the year. The three non-annual frequency bands are the "high-frequency" band with periods of up to 32 hours, the "synoptic" band with periods between 32 hours and 35 days, and the "low-frequency" band with periods longer than 35 days. Oscillations in these spectral bands are based on 30-minute, daily, and monthly data, respectively.

Table 5.3.1 shows the breakdown of the total current variance for the period 1985 to 2004 as functions of forcing factor and depth. The table also shows the overall variance attributed to the known forcing factors and the residual (unexplained) variance. The annual cycle was established statistically and removed from all series prior to spectral analysis. Section 5.2 was devoted to detailed analysis of the mean annual cycle, and the results are not repeated here. As indicated by Table 5.3.1, the annual cycle dominates the variability near the surface, but becomes less important in the intermediate layers. Variability in the high-frequency spectral band is dominated by tides and inertial oscillations which are responsible for roughly 75% of the variance in this band. These types of motions were analysed in detail in Sections 4.1 and 4.2. I only note here that while the overall energy in this band decreases with depth, the energy of the semidiurnal tidal motions has a maximum at 175 m depth which is likely determined by highly coherent semidiurnal tidal currents at this depth. The increase in semidiurnal kinetic energy at mid-depth is then a result of the modal structure of the internal tide in the area (cf. Torgrimson and Hickey, 1979; Drakopoulos and Marsden, 1993; Cummins and Oey, 1997).

For the synoptic and low-frequency bands, the current meter series were regressed against available series representing different forcing mechanisms. Each forcing series (also called a predictor) was examined, in general, with multiple lags, to find the lags at which the forcing was significantly correlated with the current. To keep the number of selected lags reasonably low, a very tight significance criterion was initially selected. Then, the threshold was lowered as necessary so that the correlation for at least one lag value passed the significance threshold. The significance threshold was never lowered below the 90% confidence level. For the synoptic band, the number of lags for which there is significant correlation varied from 6 to 17, which reflects the time scales of dominant synoptic events. For the current meter depths of 35, 100, 175 m, the highest correlation was achieved when the current lagged the along-shore component of wind stress by two days, the cross-shore component of wind stress by one day, and the sea level gradient by zero to one day. For the low-frequency band, usually one or two lag values were needed for each factor. This indicates that the low-frequency processes exert their strongest forcing on the currents typically for one to two months.

Table 5.3.1 shows both the *partial* and *individual* part of the variance explained by each forcing factor. The individual part is the amount of variance that a particular factor explains by itself, in the absence of the other factors. The partial part is the amount of variance that the factor explains when included in a multiple regression analysis with all the other factors. The difference between the individual and the partial parts is due to the mutual correlation among the different factors. If the various factors were statistically independent, the two characteristics would be the same.

For the synoptic band, the local along-shore wind stress and the along-shore sea level gradient are expected to force variations in the currents. The wind stress is a direct forcing mechanism

Table 5.3.1. Variance ($\times 10^{-4}$ m^2s^{-2}) of the along-shore current at Station A1 allocated to specific frequency bands and to different forcing factors (τ_a and τ_c denote the alongshore and cross-shore components of the wind stress, respectively, and $\Delta\zeta = \zeta_{WINTER\ HARBOUR} - \zeta_{NEAH\ BAY}$ the along-shore sea level gradient). The original 30-minute data were used for the analysis in the high-frequency spectral band, daily data were used for the MF band, and monthly data were used for the LF band. Percentage from the total variance at each depth is given in parenthesis. Both partial and individual variance explained by each factor is given (see the text).

			35 m		100 m		175 m		400 m	
Total variance			**280.17**		**208.16**		**154.09**		**35.80**	
Mean annual cycle			**104.93**	**(37%)**	**55.85**	**(27%)**	**25.81**	**(17%)**	**0.75**	**(2%)**
HF (24cpd to 0.75cpd)	Total HF		**61.03**	**(22%)**	**39.85**	**(19%)**	**27.74**	**(18%)**	**12.23**	**(34%)**
	Explained		*45.47*		*30.08*		*22.88*		*7.87*	
	Tides	Semidiurnal	9.88		9.69		13.63		4.08	
		Diurnal	11.92		7.30		4.47		2.91	
	Inertial		23.67		13.08		4.79		0.88	
	Residual		*15.56*		*9.77*		*4.86*		*4.36*	
MF (0.75cpd to 0.028cpd)	Total MF		**56.46**	**(20%)**	**68.85**	**(33%)**	**68.48**	**(44%)**	**16.78**	**(47%)**
	Explained by regression		*14.65*		*28.48*		*26.35*		*0.29*	
			partial	ind	partial	ind	partial	ind	partial	ind
	Factors	τ_a	6.09	8.85	11.73	17.18	10.34	15.55	0.04	0.04
		τ_c	0.26	3.47	0.73	7.63	1.05	7.96	0.16	0.23
		$\Delta\zeta$	4.01	7.84	7.33	14.84	6.41	13.71	0.02	0.09
	Residual		*41.81*		*40.37*		*42.13*		*16.49*	
LF (0.028cpd to 0.0002cpd)	Total LF		**57.75**	**(21%)**	**43.61**	**(21%)**	**32.06**	**(21%)**	**6.04**	**(17%)**
	Explained by regression		*15.08*		*12.98*		*7.27*		*0.72*	
			partial	ind	partial	ind	partial	ind	partial	ind
	Factors	τ_a	6.11	8.00	8.03	10.10	1.55	2.60	0.10	0.10
		τ_c	2.73	2.65	0.65	0.59	1.38	2.43	0.01	0.02
		$\Delta\zeta$	2.88	3.81	1.15	2.62	1.23	1.67	0.16	0.23
		PDO	0.84	1.04	0.01	0.40	0.71	0.86	0.02	0.08
		NPI	0.15	1.27	0.77	0.90	0.89	0.98	0.00	0.00
		NIÑO1+2	0.25	0.30	0.05	0.52	0.03	0.71	0.18	0.38
		NIÑO3	0.31	0.03	0.23	0.63	0.01	0.95	0.02	0.19
	Residual		*42.67*		*30.63*		*24.79*		*5.32*	
Total Explained			**180.14**	**(64%)**	**127.39**	**(61%)**	**82.31**	**(53%)**	**9.63**	**(27%)**
Total Residual			**100.03**	**(36%)**	**80.77**	**(39%)**	**71.78**	**(47%)**	**26.18**	**(73%)**

(e.g. McCreary, 1981). The wind stress series were obtained from Reanalysis datasets (Reanalysis data website). Reanalysis data were favoured over the local measured wind at meteorological buoys 46204, 46206, and 46207, because of the former's lower level of high frequency noise and absence of gaps in the series. At periods longer than several days, the Reanalysis and the buoy wind data are highly correlated.

Variations in the along-shore sea level gradient should be indicative of propagating coastal-trapped waves. As shown by Hickey *et al.* (1991) and Battisti and Hickey (1984), much of the variance in the currents in the zone of the continental shelf and slope off Vancouver Island, Washington, and Oregon is explained by the presence of coastal-trapped waves. Four tide gauges along the coast from British Columbia to Oregon have records of sufficient length and quality, together with the accompanying atmospheric pressure records, to account for the inverse barometer effects for determination of the gradient; these are Winter Harbour, Tofino, Neah Bay, and South Beach. The gradient between Winter Harbour and Neah Bay (with a separation of 344 km) shows the highest correlation with the currents and was selected for the final analysis.

The multiple regression model explains from 26 to 41% of the variance in the synoptic band for currents observed in the depth range from 35 to 175 m. Of all factors considered in the synoptic band, the along-shore wind stress explains the largest part of the variance at depths from 35 to 175 m (particularly at 100 and 175 m depth). The sea level gradient contributes significantly to the explained variance in the synoptic band, with the largest contribution at 100 m depth. The residual variance is approximately the same for all depths in the range from 35 to175 m. The current at 400 m depth possesses very low correlation with all factors. The flow at that depth appears to be strongly modified by the bottom topography, so that it loses direct correspondence to the initial forcing. The cross-shore wind stress explains very little of the total variance.

Monthly values of the wind stress and sea level gradient were used for the regression analysis in the low-frequency band. Monthly time series of major climate indices, the Pacific Decadal Oscillation (PDO), North Pacific Index (NPI), NIÑO1+2, and NIÑO3, were added to the regression model. The PDO is based on basin-scale sea surface temperature (SST) anomalies in the northeast Pacific (Mantua *et al.*, 1997). The NPI is the area-weighted sea level pressure over the region 30-65°N, 160E-140W, reflecting basin-scale anomalies in the strength of atmospheric systems in the North Pacific (NP Index website). NIÑO1+2 and NIÑO3 reflect SST anomalies in two characteristic regions of the equatorial Pacific. NIÑO1+2 is the average SST in the region bounded by 0-10°S and 80-90°W, the region closest to the American continent. This region usually responds first to a developing El Niño. NIÑO3 (SST averaged over 5°S-5°N and 150-90°W) has the largest variability in SST on El Niño time scales (IRI website). Thus, the PDO represents decadal variations in the North Pacific, the NPI represents large-scale atmospheric forcing in the North Pacific, and the NIÑO indices represent the influence of equatorial processes.

In the low-frequency spectral band, regression analysis explains 26, 30, and 23% of the current variance at 35, 100, and 175 m, respectively. The along-shore wind stress has maximum

Table 5.3.2. Contribution of different forcing factors to the alongshore current at Station A1 at different depths in m/s per unit forcing. Each forcing factor is considered individually, without account for mutual correlation with other forcing factors.

		35 m	100 m	175 m	400 m
MF (0.75cpd to 0.028cpd)	τ_a	1.5E-01	1.8E-01	1.6E-01	4.2E-02
	τ_c	1.6E-01	1.9E-01	1.8E-01	-5.8E-02
	$\Delta\zeta$	-2.8E-04	-3.8E-04	-3.5E-04	4.0E-05
LF (0.028cpd to 0.0002cpd)	τ_a	7.9E-01	7.5E-01	4.8E-01	1.1E-01
	τ_c	-5.7E-01	4.4E-01	3.9E-01	2.1E-01
	$\Delta\zeta$	-5.5E-04	-4.8E-04	-3.6E-04	-9.2E-05
	PDO	1.3E-02	6.0E-03	8.8E-03	4.3E-03
	NPI	5.5E-03	4.0E-03	-3.8E-03	-2.0E-03
	NIÑO1+2	1.1E-02	-1.0E-02	-5.8E-03	-2.9E-03
	NIÑO3	2.1E-03	1.8E-02	8.7E-03	-2.6E-03

influence on the currents at depths from 35 to 175 m, and particularly at 100 m depth, where it is by far the strongest factor. Over these depths, the highest correlations with the along-shore wind stress occur at zero lag. The cross-shore wind stress, although much less important than the along-shore wind stress, adds to the explained variance in the currents at 35 and 175 m depths. This addition, however, does not necessarily stress the importance of the cross-shore component of the wind stress, but may well arise from the fact that the effective axis (the axis of maximum influence of the wind stress on the current, cf. Shevchenko *et al*., 2004; Rabinovich *et al*., 2007) does not coincide with the principal axis of variance for the wind stress, which has been chosen as the along-shore wind direction. The sea level gradient is the second most important factor in the low-frequency band. As expected from dynamical considerations, the currents at all depths are negatively correlated with the sea level gradient (stronger current occurs when the sea level at Neah Bay is higher than the sea level in Winter Harbour, i.e. the sea level slopes downward in the poleward direction) with peak correlation at current lags of 5 and 9 months at 35 m depth, at 0, 4, and 8 months at 100 m depth and at -4, 0, and 4 months at 175 m depth (negative lag means the current leads the factor). Therefore, four months may present the dominant period of CTWs.

The PDO, as a reflection of sea surface processes, has the highest correlation with the near-surface current with maximum correlation occurring at zero lag. The finding that there is a relatively high correlation of the PDO with the current at 175 m depth but not with the current at 100 m depth may be a statistical artefact. NIÑO1+2 and NIÑO3 attain maximum correlation with currents at 100 and 175 m depth, close to the main thermocline. This agrees with the notion that ENSO signals propagate as a disturbance of the thermocline (Clarke and Van Gorder, 1994). Lagged correlation plots (Figure 5.3.1) for the current at all depths and the NIÑO indices show a wave like structure with positive and negative correlation periods repeating roughly every 18 to 24 months. Both the absolute and relative influence of the NPI and the NIÑO indices on the current increases with depth, while the influence of the wind and PDO decreases substantially below the main thermocline. The NPI, representing large-scale atmospheric forcing, has the highest correlation with the currents closest to the core of the California Undercurrent, the current leading the index by 5 months. The fact that the current (the response) leads the NPI (the assumed forcing) by nearly half a year is hard to explain by direct physical relationship between these two processes. This high correlation between the current and the NPI at 5-month current lead may be a statistical fluke and may indicate that basin-scale atmospheric processes have little direct influence on the Undercurrent in the region. Instead, this finding together with significant individual correlation of both the NPI and the Undercurrent with the NIÑO indices supports the idea that both the Undercurrent and atmospheric systems in the northeast Pacific experience the influence of the same remote forcing communicated from the eastern tropical Pacific to the mid-latitudes via meridionally propagating atmospheric and oceanic Kelvin waves with the oceanic disturbances travelling faster and, therefore, arriving ahead of the atmospheric signal (Chavez *et al*., 2002). Strong Los Niños are positively correlated with the currents, the current leading (in the statistical sense) the index. The "lead" of the current is explained in Figure 5.3.2. Statistically, the highest correlation between the current and the El Niño index is achieved when the strongest current corresponds to the peak of the El Niño conditions. When we consider the onset of an El Niño event, instead of its maximum intensity, the El Niño event leads the current by about two to three months (see Figure 5.3.2).

The relative contribution to the alongshore current at Station A1 from different forcing factors in the synoptic and low-frequency bands is given in Table 5.3.2. The values represent regression coefficients of the current for each forcing factor individually, without taking into account other factors. The current is specified at the lag having maximum correlation with the corresponding forcing factor. The forcing factors are the same as those used for the multiple regression analysis.

Modification

In addition to the driving mechanisms discussed above, several physical phenomena (discussed in Sections 2.2 and 2.3) can modify the along-shore currents. Instability of the mean flow can cause significant variability of the along-slope currents (Huyer *et al*., 1984; Thomson, 1984; Lynn and Simpson, 1987, 1990; Kosro *et al*., 1991; Thomson and Gower, 1998; Chereskin *et al*., 2000; Kosro, 2002). Interaction with large-scale coastal irregularities can lead to separation of coastal jets resulting in formation of meanders and filaments (e.g. Bormans and Garrett 1989; Haidvogel *et al*., 1991; McCreary *et al*., 1991; Barth *et al*., 2000; Castelao and Barth, 2006). The rugged continental slope and series of cross-slope canyons off southern Vancouver Island are expected to modify the slope flow (Allen *et al*., 2001). A dramatic modification of flow within a canyon, as discussed in several parts of this text, is clearly seen in the current at 400 m depth. All these types of variability can not be accounted for in the regression analysis.

The mechanism of buoyancy shutdown may be an important factor in the intensification of a stratified flow along a sloping bottom (discussed in 2.3.2.1, MacCready and Rhines, 1993; Garrett *et al*., 1993; Chapman, 2002). This happens if the characteristic buoyancy shutdown time is less than the frictional

Figure 5.3.1.Lagged correlation coefficient among the monthly series of the along-shore current at Station A1 and the alongshore and cross-shore components of the wind stress (τ_a and τ_c, respectively), the sea level gradient ($\Delta\zeta = \zeta_{\mathrm{WINTER\ HARBOUR}} - \zeta_{\mathrm{NEAH\ BAY}}$), and climate indices. Dashed lines mark 95% confidence level.

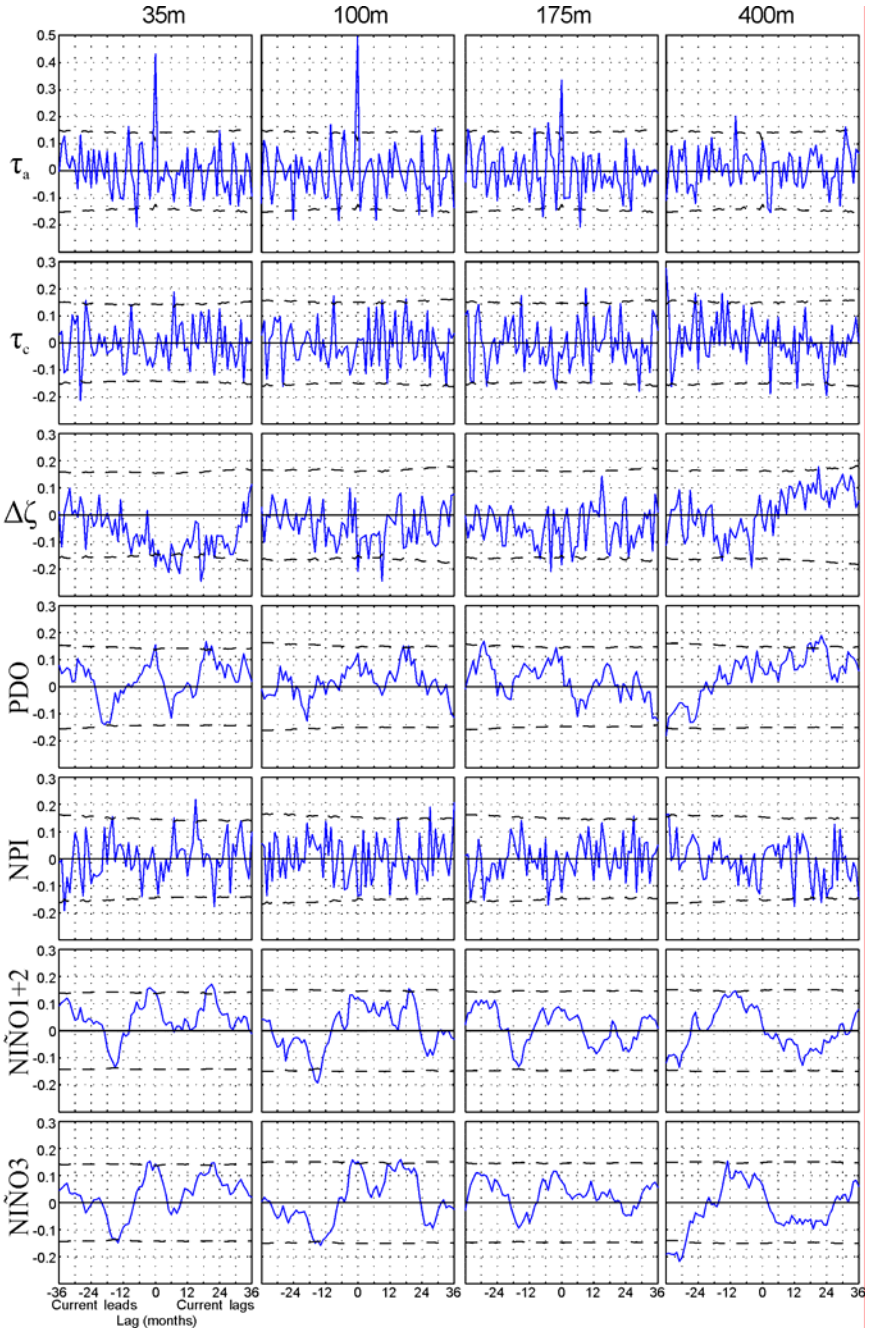

spin-down time. For a quadratic bottom drag, the buoyancy shutdown time for the case of a downwelling alongshore current (the California Undercurrent, poleward for the most of the year, is similar to a downwelling current) is given by

$$T_b = \left(\frac{f}{\alpha N}\right)^3 \frac{1}{C_d N}, \tag{5.3.1}$$

where f is the Coriolis parameter, α is the bottom slope, N is the Brunt-Väisälä (buoyancy) frequency, and C_d is the bottom drag coefficient Garrett *et al.* (1993). The frictional spin-down time can be evaluated as

$$T_f = \frac{H}{C_d U}, \tag{5.3.2}$$

where H is a characteristic water depth and U is a characteristic along-isobath flow. Taking the following values for the parameters from the region of mooring deployment: $H = 500$ m, $U = 0.1$ m/s, $C_d = 2.5\times10^{-3}$, $\alpha = 3.25\times10^{-2}$ rad, $N = 3.2\times10^{-3}$ rad/s, and

$f = 1.09\times10^{-4}$ rad/s, we estimate T_b as 1.7 days and T_f as 19 days. The order of magnitude lower buoyancy shutdown time indicates that for the slope region in the vicinity of Site A1, the process of buoyancy shutdown can play an important role in reduction of frictional deceleration of the along-isobath flow. This conclusion,

Figure 5.3.2. Monthly values of along-shore current at Site A1 at 175 m depth and the NIÑO1+2 index. The plot shows that the onset of El Niño leads the onset of strong currents off Vancouver Island.

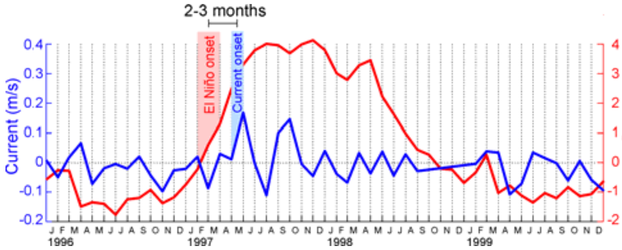

however, should be taken with care. Chapman (2002) points out that such estimates are highly sensitive to the bottom slope and buoyancy frequency, and a slight change in these parameters can significantly alter the estimates of the characteristic timescales. For a fixed position and bottom slope the only parameter which influences the estimate of the buoyancy shutdown time is N. At the hydrographic station LC09 in the water depth of 600 m on the continental slope off Vancouver Island, N typically varies from a minimum of 1×10^{-3} rad/s to a maximum of 5×10^{-3} rad/s near the bottom. With f and α fixed at the above values, this range of N gives T_b varying from 0.28 to 175 days with T_b>19 days (corresponding to N=1.74×10^{-3} rad/s) in about 7% of the total of 92 observations at LC09 for the period from 1985 to 2005. Therefore, the mechanism of buoyancy shutdown seems to be a plausible factor reducing frictional deceleration of the slope currents in the region; however it may not always be active. The thickness of the bottom boundary layer can be evaluated as

$$\delta = \frac{Uf}{\alpha N^2} \qquad (5.3.3)$$

Garrett *et al.* (1993). Taking the above values for the parameters, I estimate δ to be 30 m.

The overall variance explained by the wind stress, the sea level gradient, and the climate indices is unexpectedly low. This may be indicative of the high complexity of the slope current dynamics, including modification of the currents by local conditions. In addition, the series used for the regression analysis may not accurately represent the forcing mechanisms. For example, the series of wind stress for one location may not be representative of the highly non-uniform forcing that is applied to the relatively large area of the sea surface. Similarly, the sea level slope between two fixed coastal gauge stations may not be an accurate proxy variable for coastal-trapped waves with varying wavelengths and periods. In addition, several other processes can create an along-shore sea level gradient. If the wind stress is not uniform along the coast, it can produce a cross-shore Ekman transport of varying strength, thus creating differences in sea level along the coast. Wind stress curl, although usually varying on larger spatial scales than the wind stress, can still be non-uniform along the coast on a scale of 300-400 km (the distance between the Winter Harbour and Neah Bay tide gauges on the west coast) leading to a non-uniform sea level change. Nevertheless, certain conclusions can be drawn from the regression analysis. The high correlation with the local wind stress relative to the other factors indicates that it is likely a major driving factor for the slope currents including the CUC. The high relative correlation with the sea level gradient in the synoptic band indicates the possible importance of CTWs in the slope current variability (Huthnance, 1981; Hickey *et al.*, 1991). The correlation of the low-frequency currents with the sea level gradient, NIÑO1+2, and NIÑO3 may be indicative of the poleward propagation of depressions in the main thermocline that originate from the Eastern Tropical Pacific. Because of the highly non-uniform cross-shore structure of the coastal wind stress field, I was not able to obtain reliable time series of the wind stress curl with sufficient resolution for the narrow shelf-slope region. I am therefore not able to comment on the importance of the wind stress curl to forcing of the CUC. However, according to previous studies (Hickey, 1979; Bretschneider and McLain, 1983; McLain and Thomas, 1983), the local wind stress curl in the nearshore regions of the northeast Pacific is not correlated with the local dynamic topography and the along-shore currents.

6. Summary and conclusions

High quality, long-term current meter measurements and extensive water property data collected by the Institute of Ocean Sciences on the continental slope off the west coast of Vancouver Island have been used to examine the spatial and temporal variability of the California Undercurrent (CUC) off the west coast of British Columbia. Until this study, the poleward extent and associated structure of the Undercurrent have remained largely unexplored.

Studies off the west coast of the United States show that the CUC consists of a slope-intensified, subsurface poleward flow of relatively warm, high salinity, low oxygen, high nutrient water. Results of this study suggest that the CUC also persists for the most of the year off the coast of Vancouver Island (albeit, as a merged flow with the wind-forced poleward Davidson Current in winter) and may extend northward of 51°N along the continental slope bordering Queen Charlotte Sound. The former result is supported by the subsurface maximum in the Pacific Equatorial Water concentration throughout the year. The undercurrent is found from 100 m depth to the bottom, with annual mean poleward currents of around 0.04 m/s at a core depth of around 175 m. Core depths appear to shoal poleward by several tens of meters along the length of Vancouver Island. Within the study region, the undercurrent is found to straddle the Vancouver Island continental slope and, based on water property data (and the thermal wind relationship, which is the foundation of geostrophic velocity calculations), to have a lateral extent of 30 to 40 km and associated baroclinic volume transport of around 0.5 Sv. At the latitude of southern Vancouver Island, the CUC consists of roughly 30% Pacific Equatorial Water (PEW) and 70% Pacific Subarctic Upper Water (PSUW). The concentration of PEW off Vancouver Island is observed to diminish poleward at a rate of 2% per 100 km of coastline. Projecting this rate of change equatorward yields a source region (100% PEW) near 20°N, consistent with the known position of the Pacific Equatorial Water off the coast of North America. The Undercurrent has a remarkably uniform alongshore structure and shows no significant flow reduction along the entire extent of Vancouver Island and southern part of Queen Charlotte Sound. Projecting the above rate of mean PEW content reduction in the Undercurrent poleward along the west coast of the Queen Charlotte Islands, I find that the CUC has a potential to carry PEW to southeast Alaska.

The moored current meter observations show seasonally reversing currents above the main pycnocline (depths < 100 m) and persistent poleward flow below. Temporal variability of the undercurrent between 100 and 300 m depth is also dominated by a strong seasonal cycle, with the phase of the annual cycle varying markedly with depth. At the core depth of around 175 m, the annual cycle reaches a maximum alongshore velocity of 0.1 m/s (poleward) in early winter and a minimum alongshore velocity of –0.03 m/s (equatorward) in early summer. The early summer reversal in the mean flow over the 100 to 300 m depth range may reflect the vertical extent of prevailing northwesterly winds in summer, summer-winter changes in the alongshore baroclinic pressure gradient, or seasonal changes in other forcing mechanisms. Superimposed on the seasonal cycle, is strong variability at other time scales. In addition to tidal and inertial oscillations, the current meter records reveal strong variability within the 20-day period synoptic weather band and 2.1- 2.5-year oscillations of unknown origin. The 20-day oscillations (possibly caused by remotely forced Coastally Trapped Waves, CTWs) mark the transition from the high frequency band (with its depth-independent spectral background characteristics) to the low-frequency band where there is "whitening" of the spectra with depth. Large-scale atmospheric-oceanic interactions influence the CUC off Vancouver Island at interannual time scales, with stronger poleward flow in the CUC occurring during times of El Niño conditions in the equatorial Pacific and a stronger Aleutian Low in the subarctic northeast Pacific.

Because it is forced both locally and remotely in the near-shore area and influenced by basin-scale ocean-atmosphere processes, the CUC has complex dynamics. The primary forcing mechanisms for the CUC include the local alongshore wind stress, the alongshore baroclinic pressure gradient, and the propagation of CTWs. However, based on an analysis of the existing data, no one mechanism proposed by different authors can be singled out as one of the driving mechanisms or ruled out as a possible contributor to the slope undercurrent. The general conclusion is that the CUC is a complicated phenomenon, possibly driven by a number of forcing factors such as alongshore winds and baroclinic density gradients in the adjacent open Pacific Ocean, with subsequent modification by other mechanisms such as CTWs and slope induced upwelling.

Suggestions for future research

The current meter data used in present research span the period up to the fall of 2004. However, Station A1 has continued to be occupied since then with Acoustic Doppler Current Profilers (ADCPs) replacing the current meters. ADCPs provide better vertical resolution and are usually more reliable. Therefore, analysis of the recent records from Station A1 could provide additional insight into the vertical structure and time variability of the currents. Appending the records to the existing series at nominal current meter depths would yield even longer time series allowing improvement in statistical reliability of long-term average estimates and exploration of anomalies in recent years.

The question remains open: how far to the north does the CUC extend? Water property data off Queen Charlotte Sound and Queen Charlotte Islands are available to help address this question. Other long-term current meter series (Stations E3 and BP1 at the continental slope off Estevan Point and Brooks peninsula, albeit shorter than A1 series, but still spanning over a decade) suggest an obvious extension of the project to explore along-shore evolution of the slope flow.

Of more immediate practical importance, is understanding the variability of nutrient supply to the coastal waters of British Columbia in connection with the biological processes in the region. In particular, the CUC supplies nutrient-rich water which enters Juan de Fuca Strait and is both mixed into the upper layer of the strait from where it is then transported to the west coast of Vancouver Island as part of the Vancouver Island Coastal Current. The fraction of intruding CUC water that remains in the lower layer is transported at mid to near bottom depths into the Strait of Georgia. Also, it is possible that the anomalies in the CUC intensity are related to the periods of anoxic conditions observed off the coasts of Oregon, Washington and British Columbia. Clarification of these physical-biological links can have a considerable practical output in the form of better understanding of local processes for the purposes of the fisheries industry on the Pacific coast of Canada.

Bibliography

Aanderaa Instruments. 1983. *RCM4/5 operating manual*. Technical description No. 119.

Allen, J. S. 1973. Upwelling and coastal jets in a continuously stratified ocean. *Journal of Physical Oceanography*, **3**, 245–257.

Allen, S.E. 1996. Topographically generated, subinertial flows within a finite length canyon. *Journal of Physical Oceanography*, **26**, 1608-1632.

Allen, S. E., Vindeirinho, C., Thomson, R. E., Foreman, M. G. G., Mackas, D. L. 2001. Physical and biological processes over a submarine canyon during an upwelling event. *Canadian Journal of Fisheries and Aquatic Sciences*, **58,** 671-684.

Bakun, A., 1990. Global climate change and intensification of coastal ocean upwelling. *Science*, **247**, 198–201.

Barnes, C. A., Duxbury, A. C., Morse, B. A. 1972. Circulation and selected properties of the Columbia River effluent at sea. In: Pruter, A. T. and Alverson, D. L. (Eds.), *The Columbia River estuary and adjacent ocean waters*. University of Washington Press, Seattle, 41-80.

Barth, J. A., Pierce, S. D., Smith, R. L. 2000. A separating coastal upwelling jet at Cape Blanco, Oregon and its connection to the California Current System. *Deep-sea research. Part II - topical studies in oceanography*, **47**(5-6), *783-810.*

Battisti, D. S., Hickey, B. M. 1984. Application of remote wind-forced coastal trapped wave theory to the Oregon and Washington coasts. *Journal of Physical Oceanography*, **14**, 887–903.

Beamish, R. J., Noakes, D. J., McFarlane, G. A., Klyashtorin, L., Ivanov, V. V., Kurashov, V. 1999. The regime concept and natural trends in the production of Pacific salmon. *Canadian Journal of Fisheries and Aquatic Sciences*, **56**, 516–526.

Bennett, E. B. 1959. Some oceanographic features of the northeast Pacific Ocean during August 1955. *Journal of the Fisheries Research Board of Canada*, **16**, 565-633.

Bograd, S. J., Thomson, R. E., Rabinovich, A. B., LeBlond, P. H. 1999. Near-surface circulation of the northeast Pacific Ocean derived from WOCE-SVP satellite-tracked drifters. *Deep-sea research. Part II - topical studies in oceanography*, **46**, 2371-2403.

Bograd, S. J., Lynn, R. J. 2003. Anomalous Subarctic influence in the southern California Current during 2002. *Geophysical Research Letters*, doi:10.1029/2003GL017446.

Bormans, M., Garrett, C. 1989. A simple criterion for gyre formation by the surface outflow from a strait, with application to the Alborean Sea. *Journal of Geophysical Research*, **96**, 12,637–12,644.

Bretschneider, D., McLain, D. R. 1983. Sea level variations at Monterey, CA. *U.S. Department of Commerce, NOAA Technical Report* NMFS SSRF-761, 50 p.

Castelao, R. M., Barth, J. A. 2006. The relative importance of wind strength and along-shelf bathymetric variations on the separation of a coastal upwelling jet. *Journal of Physical Oceanography*, **36**, 412-425.

Castro, C. G., Chavez, F. P., Collins, C. A. 2001. Role of the California Undercurrent in the export of denitrified waters from the eastern tropical North Pacific. *Global Biogeochemical Cycles*, **15**, 819-830.

Chapman, D. C. 2002. Deceleration of a finite-width, stratified current over a sloping bottom: frictional spindown or buoyancy shutdown? *Journal of Physical Oceanography*, **32**, 336–352.

Chavez, F. P., Collins, C. A., Huyer, A., Mackas, D. L. 2002. El Niño along the west coast of North America. *Progress in Oceanography*, **54**(1-4), 1-5.

Chelton, D. B. 1982. Large-scale response of the California Current to forcing by the wind stress curl. *California Cooperative Investigations Progress Report*, **23**, 130–184.

Chelton, D. B., Bernal, P. A., McGowan, J. A. 1982. Large-scale interannual physical and biological interaction in the California Current. *Journal of Marine Research*, **40**, 1095–1125.

Chelton, D. B., deSzoeke, R. A., Schlax, M. G., El Naggar, K., Siwertz, N. 1998. Geographical variability of the first-baroclinic Rossby radius of deformation. *Journal of Physical Oceanography*, **28**, 433 - 460.

Chereskin, T. K., Morris, M. Y., Niiler, P. P., Kosro, P. M., Smith, R. L., Ramp, S. R., Collins, C. A., Musgrave, D. L. 2000. Spatial and temporal characteristics of the mesoscale circulation of the California Current from eddy-resolving moored and shipboard measurements. *Journal of Geophysical Research*, **105**, 1245–1270.

Choboter, P. F., Samelson, R. M., Allen, J. S. 2005. A new solution of a nonlinear model of upwelling. *Journal of Physical Oceanography,* **35**(4), 532-544.

Clarke, A. J., Van Gorder, S. 1994. On ENSO coastal currents and sea levels. *Journal of Physical Oceanography*, **24**, 661–680.

Collins, C. A., Garfield, N., Paquette, R. G., Carter, E. 1996a. Lagrangian measurement of subsurface poleward flow between 38°N and 43°N along the west coast of the United States during summer, 1993. *Geophysical Research Letters*, **23**, 2461–2464.

Collins, C. A., Garfield, N., Paquette, R. G., Carter, E. 1996b. Corrections to "Lagrangian measurement of subsurface poleward flow between 38°N and 43°N along the west coast of the United States during summer, 1993". *Geophysical Research Letters*, **23**(22), 3283-3283.

Collins, C. A., Paquette, R. G., Ramp, S. R. 1996c. Annual variability of ocean currents at 350-m depth over the continental slope off Point Sur, California. *California Cooperative Investigations Progress Report*, **37**, 257–263.

Collins, C. A., Ivanov, L. M., Melnichenko O. V. 2003. Seasonal variability of the California Current System extracted from the RAFOS 1992– 2002. *Marine Hydrophysical Journal*, **2**, 24– 33.

Cox, C. 1962. Internal waves. In M.W. Hill, editor, *The Sea, Vol. 1: Physical Oceanography: Ideas and observations on progress in the study of the sea.* Wiley, New York, pp. 752-763.

Collins, C. A., Ivanov, L. M., Melnichenko O. V., Garfield N. 2004. California Undercurrent variability and eddy transport estimated from RAFOS float observations. *Journal of Geophysical Research*. **109**, C05028, doi:10.1029/2003JC002191.

Crawford, W. R., Dewey, R. K. 1989. Turbulence and mixing: Sources of nutrients on the Vancouver Island continental shelf. *Atmosphere-Oceans*, **27**(2), 428-442.

Crawford, W. R., Thomson, R. E. 1982. Continental shelf waves of diurnal period along Vancouver Island. *Journal of Geophysical Research,* **87,** 9516–9522.

Crawford, W. R., Thomson, R. E. 1984. Diurnal-period continental shelf waves along Vancouver Island: A comparison of observations with theoretical models. *Journal of Physical Oceanography,* **14,** 1629–1646.

Crawford, W. R., Thomson, R. E. 1991. Physical Oceanography of the Western Canadian continental shelf. *Continental Shelf Research*, **11**, 669-683.

Csanady, G. T. 1979. The pressure field along the western margin of the North Atlantic. *Journal of Geophysical Research*, **81**(C8), 4905–4915.

Cummins, P. F., Lagerloef, G. S. E. 2004. Wind-driven interannual variability over the Northeast Pacific. *Deep-Sea Research*, **51**, 2105-2121.

Cummins, P. F., Oey, L. Y. 1997. Simulation of barotropic and baroclinic tides off northern British Columbia. *Journal of Physical Oceanography*, **27**, 762-781.

Cummins, P. F., Masson, D., Foreman, M. G. G. 2000. Stratification and mean flow effects on diurnal currents off Vancouver Island. *Journal of Physical Oceanography*, **30,** 15–30.

Cummins, P. F., Cherniawsky, J. Y., Foreman, M. G. G. 2001. North Pacific internal tides from the Aleutian Ridge: Observations and modelling. *Journal of Marine Research*, **59**, 167–191.

D'Asaro, E. A. 1985. The energy flux from the wind to near-inertial motions in the surface mixed layer. *Journal of Physical Oceanography,* **15,** 1043-1059.

Dewey, R. K., Moum, J. N., Paulson, C. A., Caldwell, D. R., Pierce, S. D. 1991. Structure and dynamics of a coastal filament. *Journal of Geophysical Research*, **96**, 14,885-14,907.

Dias, J. 2006. Internal tide spatial variability off western Portugal detected by current meter observations. *Geophysical Research Letters*, **33**, L06613, doi:10.1029/2005GL024957.

Dobrovol'skii, A. D. 1961. On the determination of water masses. *Okeanologiya,* **1**(1) (in Russian).

Dorman, C. E. 1985. Evidence of Kelvin waves in California's marine layer and related eddy generation. *Monthly Weather Review*, **113**, 827–839.

Dorman, C. E., Winant, C. D. 1995. Buoy observations of the atmosphere along the west coast of the United States, 1981-1990. *Journal of Geophysical Research*, **100**, 16,029-16,044.

Drakopoulos, P. G., Marsden, R. F. 1993.The internal tide off the west coast of Vancouver Island. *Journal of Physical Oceanography,* **23**, 758-775.

Ebbesmeyer, C. C., Cayan, D .R., McLain, D. R., Nichols, F. H., Peterson, D. H., Redmond, K. T. 1991. 1976 step in the Pacific climate: forty environmental changes between 1968–1975 and 1977–1984. In: Betancourt, J. L., Tharp, V. L. (Eds.), *Proceedings of the Seventh Annual Pacific Climate (PACLIM) Workshop, Asilomar, CA*, Vol. **26**. California Department of Water Resources, Interagency Ecological Studies Program Technical Report, 115–126.

Eden, C., Timmerman, A. 2004. The influence of the Galapagos Islands on tropical temperatures, currents and the generation of tropical instability waves. *Geophysical Research Letters,* **31**, L15308 1-4.

Emery, W. J., Meincke, J. 1986. Global water masses: summary and review. *Oceanologica Acta*, **9**, 383-391.

Emery, W. J., Thomson, R. E. 2001. *Data Analysis Methods in Physical Oceanography: 2nd Edition Revised*. Elsevier Science. Amsterdam, 640p.

Eriksen, C. C. 1982. Observations of internal wave reflection off sloping bottoms. *Journal of Geophysical Research,* **87**, 525-538.

Foreman, M. G. G. 1978. Manual for Tidal Currents Analysis and Prediction. *Pacific Marine Science Report 78-6*, Institute of Ocean Sciences, Patricia Bay, Sidney, B.C., 57 pp. (2004 revision).

Foreman, M. G. G., Thomson, R. E. 1997. Three-dimensional model simulations of tides and buoyancy currents along the west coast of Vancouver Island. *Journal of Physical Oceanography,* **27** (7), 1300-1325.

Foreman, M. G. G., Callendar, W., MacFadyen, A., Hickey, B. M., Thomson, R. E., Di Lorenzo, E. 2008. Modeling the generation of the Juan de Fuca Eddy. *Journal of Geophysical Research*, **113**, C03006, doi:10.1029/2006JC004082.

Freeland, H. J., Denman, K. L. 1982. A topographically controlled upwelling center off southern Vancouver Island. *Journal of Marine Research*, **40,** 1069–1093.

Freeland, H. J., Crawford, W. R, Thomson, R. E.1984. Currents along the Pacific coast of Canada. *Atmosphere-Ocean*, **22**(2), 151-172.

Freeland, H. J., Gatien, G., Huyer, A., Smith, R. L. 2003. Cold halocline in the northern California Current: an invasion of subarctic water. *Geophysical Research Letters*, **30**(3), 1141, doi:10.1029/2002GL016663.

Garfield, N., Collins, C. A., Paquette, R. G., Carter E. 1999. Lagrangian exploration of the California Undercurrent, 1992– 95. *Journal of Physical Oceanography*, **29**, 560– 583.

Garfield, N., Maltrud, M. E., Collins, C. A., Rago, T. A., Paquette, R. G. 2001. Lagrangian flow in the California Undercurrent, an observation and model comparison. *Journal of Marine Systems*, **29**(1-4), 201-220.

Garrett, C. J. R., Munk, W. H. 1972. Space-time scales of internal waves. *Geophysical Fluid Dynamics,* **3**, 225–264.

Garrett, C., MacCready, P., Rhines, P. B. 1993. Boundary mixing and arrested Ekman layers: rotating, stratified flow near a sloping boundary. *Annual Review of Fluid Mechanics*, **25**, 291-323.

Gershunov, A., Barnett, T. P. 1998. Interdecadal modulation of ENSO teleconnections*. Bulletin of the American Meteorological Society*, **79**, 2715-2726.

Gill, A. E. 1982. *Atmosphere-Ocean Dynamics*, Academic Press, New York, 662 pp.

Gonella, J. 1972. A rotary component method for analyzing meteorological and oceanographic vector time series. *Deep-Sea Research*, **19**, 833-846.

Graham, N. E., 1994. Decadal-scale climate variability in the tropical and North Pacific during the 1970s and 1980s: observations and model results. *Climate Dynamics*, **10**, 135–162.

Graham, N.E., Diaz, H.F., 2001. Evidence for intensification of North Pacific winter cyclones since 1948. *Bulletin of the American Meteorological Society*, **82**, 1869–1893.

Haidvogel, D. B., Beckman, A., Hedstrom, K. 1991. Dynamical simulation of filament formation and evolution in the coastal transition zone. *Journal of Geophysical Research*, **96,** 15 017–15 040.

Halpern, D. 1976. Structure of a coastal upwelling event observed off Oregon during July 1973. *Deep-Sea Research*, **23**, 495–508.

Hare, S. R., Mantua, N. J. 2000. Empirical evidence for North Pacific regime shifts in 1977 and 1989. *Progress in Oceanography*, **47**, 103-145.

Harrison, D. E., Larkin, N. K. 1998. El Niño-Southern Oscillation sea surface temperature and wind anomalies, 1946–1993. *Review of Geophysics*, **36**, 353–399.

Helland-Hansen, B. 1934. The Sognefjord Section. Oceanographic observations in the northernmost part of the North Sea and the southern part of the Norwegian Sea. In: *James Johnstone Memorial Volume*, University Press, Liverpool, 257–274.

Hermann, A. J., Hickey, B. M., Mass, C. F., Albright, M. D. 1990. Orographically trapped coastal wind events in the Pacific Northwest and their oceanic response. *Journal of Geophysical Research*, **95**(C8), 13,169–13,193.

Hewitt, R. P. 1988. Historical review of the oceanographic approach to fishery research. *California Cooperative Investigations Progress Report*, **29**, 27–41.

Hickey, B. M. 1979. The California Current system-hypotheses and facts. *Progress in Oceanography*, **8**(4), 191-279.

Hickey, B. M. 1989a. Poleward flow near the northern and southern boundaries of the U.S. west coast. In: Neshyba, S. J., Mooers, C. N. K., Smith, R. L., Barber, R. T., (Eds.), *Poleward flows along eastern ocean boundaries*. Springer-Verlag, New York, 160-175.

Hickey, B. M. 1989b. Patterns and processes of circulation over the Washington Continental shelf and slope. In: Landry, M. R., and Hickey, B. M., (Eds.), *Coastal Oceanography of Washington and Oregon*. Elsevier, Amsterdam, 41-115.

Hickey, B. M. 1997. The response of a steep-sided narrow canyon to strong wind forcing. *Journal of Physical Oceanography*, **27,** 697–726.

Hickey, B. M. 1998. Coastal oceanography of western North America from the tip of Baja California to Vancouver Island. In: Robinson, A. R., and Brink, K. H., (Eds.), *The Sea, Vol. 11: The Global Coastal Ocean - Regional Studies and Syntheses.* Wiley, 345–393.

Hickey, B. M., Thomson, R. E., Yih, H, LeBlond, P. H. 1991. Velocity and temperature fluctuations in a buoyancy-driven current off Vancouver Island. *Journal of Geophysical Research*, **96,** 10,507-10,538.

Hickey, B., MacFadyen, A., Cochlan, W., Kudela, R., Bruland, K., Trick, C. 2006. Evolution of chemical, biological, and physical water properties in the northern California Current in 2005: Remote or local wind forcing? *Geophysical Research Letters*, **33**, L22S02, doi:10.1029/2006GL026782.

Hill, A. E., B. M. Hickey, F. A. Shillington, P. T. Strub, K. H. Brink, E. D. Barton, A. C. Thomas. 1998. Eastern ocean boundaries coastal segment (E). In: Robinson, A. R., and Brink, K. H., (Eds.), *The Sea, Vol. 11: The Global Coastal Ocean - Regional Studies and Syntheses*. Wiley, 29-67.

Hsieh, W. W., Ware, D. M., Thomson, R. E. 1995. Wind-induced Upwelling along the west coast of North America, 1899-1988. *Canadian Journal of Fisheries and Aquatic Sciences*, **52**, 325-334.

Huggett, W. S., Crawford, W. R., Thomson, R. E., Woodward, M. V. 1987. Coastal Ocean Dynamics Experiment (CODE), Part 1-5. *Data of current observations, Vol. XIX. Institute of Ocean Sciences*. Part 1: 77p. Part 2; Part 3; Part 4; Part 5.

Huthnance, J. M. 1981. Waves and currents near the continental shelf edge. *Progress in Oceanography*, **10**, 193-226.

Huyer, A. 2003. Preface to special section on enhanced Subarctic influence in the California Current, 2002. *Geophysical Research Letters*, **30**(15), 8019, doi:10.1029/2003GL017724.

Huyer, A., Smith, R. L. 1985. The signature of El Niño off Oregon, 1982-1983. *Journal of Geophysical Research*, **90**, 7133-7142.

Huyer, A., Gagnon, J., Huggett, S. 1976. Observations from current meters moored over the continental shelf off Vancouver Island, 28 November 1974 to 8 April 1975, and related oceanographic and meteorological data. *Technical Report No. 4*, Environment Canada, Fisheries and Marine Service, Ottawa, Ont., 54 pp.

Huyer, A., Smith, R. L., Hickey, B. M. 1984. Observations of a warm-core eddy off Oregon, January to March 1978. *Deep-Sea Research*, **31**, 97–117.

Huyer, A., Kosro, P. M., Lentz, S. J., Beardsley, R. C. 1989. Poleward flow in the California current system. In: Neshyba, S. J., Mooers, C. N. K., Smith, R. L., and Barber, R. T., (Eds.), *Poleward flow along eastern ocean boundaries.* Springer-Verlag, New York, 142–156.

Huyer, A., Smith, R. L., Fleischbein, J. 2002. The coastal ocean off Oregon and Northern California during the 1997–98 El Niño. *Progress in Oceanography*, **54**(1-4), 311-341.

Huyer, A., Wheeler, P. A., Strub, P. T., Smith, R. L., Letelier R., Kosro, P. M. 2007. The Newport line off Oregon – Studies in the North East Pacific. *Progress In Oceanography*, **75**(2), 126-160.

Ingraham, W. J., Jr. 1967. The geostrophic circulation and distribution of water properties off the coasts of Vancouver Island and Washington, spring and fall 1963. *Fishery Bulletin*, **66**(2), 223-250.

Kundu, P. K., 1990. *Fluid Mechanics*. Academic Press, San Diego, 638 pp.

Kosro P. M. 2002. A poleward jet and an equatorward undercurrent observed off Oregon and northern California, during the 1997–98 El Niño. *Progress in Oceanography*, **54**, 343–360.

Kosro, P. M., Huyer, A., Ramp, S. R., Smith, R. L., Chavez, F. P., Cowles, T. J., Abbott, M. R., Strub, P. T., Barber, R. T. 1991. The structure of the transition zone between coastal waters and the open ocean off northern California, winter and spring 1987. *Journal of Geophysical Research*, **96**, 14707–14730.

Kundu, P. K., Thomson, R. E. 1990. Inertial oscillations observed near British Columbia. *Pure and Applied Geophysics*, **133,** 677-689.

LeBlond, P. H., Mysak, L. A. 1978. *Waves in the Ocean.* Elsevier, 602 pp.

LeBlond, P. H., Dyck, K., Perry, K., Cumming, D. 1983. *Runoff and precipitation time series for the coasts of British Columbia and Washington State.* Dept. of Oceanography, University of British Columbia Rep. 39, 133 pp.

Ledwell, J. R., Watson, A. J., Law, C. S. 1998. Mixing of a tracer in the pycnocline. *Journal of Geophysical Research*, **103** (C10), 21,499–21,529.

Lluch-Belda, D., Laurs, R. M., Lluch-Cota, D. B., Lluch-Cota, S. E. 2001. Long-term trends of interannual variability in the California Current System. *California Cooperative Investigations Progress Report*, **42**, 129–144.

Lynn, R. J. 1983. The 1982–83 warm episode in the California current. *Geophysical Research Letters,* **10**, 1093–1095.

Lynn, R. J., Bograd, S. J. 2002. Dynamic evolution of the 1997–99 El Niño–La Niña cycle in the southern California current. *Progress in Oceanography*, **54**(1-4), 59-75.

Lynn, R. J., Simpson, J. J. 1987. The California Current system: the seasonal variability of its physical characteristics. *Journal of Geophysical Research*, **92**, 12947–12966.

Lynn, R. J., Simpson, J. J. 1990. The flow of the undercurrent over the continental borderland off southern California. *Journal of Geophysical Research*, **95**, 12,995–13,008.

MacCready, P., Rhines, P. B. 1993. Slippery bottom boundary layers on a slope. *Journal of Physical Oceanography,* **23**, 5-22.

MacFadyen, A., Hickey, B. M., Cochlan, W. P. 2008. Influences of the Juan de Fuca Eddy on circulation, nutrients, and phytoplankton production in the northern California Current System. *Journal of Geophysical Research*, **113**, C08008, doi:10.1029/2007JC004412.

Mackas, D. L., Denman, K. L., Bennett, A. F. 1987. Least squares multiple tracer analysis of water mass composition. *Journal of Geophysical Research.* **92**, 2907–2918.

Mamayev, O. I. 1975. *Temperature–Salinity Analysis of World Ocean Waters*. Elsevier Oceanography Series, No. 11, Elsevier, 374 pp.

Mantua, N. J., Hare, S. R., Zhang, Y., Wallace, J. M., Francis, R. C. 1997. A Pacific interdecadal climate oscillation with impacts on salmon production. *Bulletin of the American Meteorological Society*, **78**, 1069–1079.

Mass, C. F., Albright, M. D. 1987. Coastal southerlies and alongshore surges of the West Coast of North America: Evidence of mesoscale topographically trapped response to synoptic forcing. *Monthly Weather Review*, **115**, 1707–1738.

McCreary, J. P. 1981. A linear stratified ocean model of the Coastal Undercurrent. *Philosophical Transactions of the Royal Society of London,* **302A**, 385–413.

McCreary, J. P., Shetye, S. R., Kundu, P. K. 1986. Thermohaline forcing of eastern boundary currents: With application to the circulation off the west-coast of Australia. *Journal of Marine Research,* **44**(1), 71-92.

McCreary, J. P., Fukamachi, Y., Kundu, P. K. 1991. A numerical investigation of jets and eddies near an eastern ocean boundary. *Journal of Geophysical Research,* **96**, 2525–2534.

McGowan, J. A. 1985. El Niño 1983 in the southern California Bight. In: Wooster, W. S., Fluharty, D. L., (Eds.), *El Niño North: El Niño Effects in the Eastern Subarctic Pacific Ocean.* Washington Sea Grant Program, Seattle, 166–184.

McGowan, J. A., Bograd, S. J., Lynn, R. J., Miller, A. 2003. The biological response to the 1977 regime shift in the California Current: a tale of two regimes. *Deep-sea research. Part II - topical studies in oceanography*, **50**, doi:10.1016/S0967-0645(03)00135-8.

McLain, D. R., Thomas, D. H. 1983. Year-to-year fluctuations of the California Countercurrent and effects on marine organisms. *California Cooperative Investigations Progress Report,* **24**,165-181.

McLain, D. R., Brainard, R. E., Norton, J. G. 1985. Anomalous warm events in eastern boundary current systems. *California Cooperative Investigations Progress Report*, **26**, 51–64.

Middleton, J. F., Leth, O. K. 2004. Wind-forced setup of upwelling, geographical origins, and numerical models: The role of bottom drag. *Journal of Geophysical Research*, **109**, C12019, doi:10.1029/2003JC002126.

Mihaly, S. F., Thomson, R. E., Rabinovich, A. B. 1998. Evidence for nonlinear interaction between internal waves of inertial and semidiurnal frequency. *Geophysical Research Letters*, **25**(8), 1205-1208.

Miller, A. J. 1996. Recent advances in California Current modeling: decadal and interannual thermocline variations. *California Cooperative Investigations Progress Report*, **37**, 69–79.

Millero, F. J., Poisson, A. 1981. International one-atmosphere equation of state of seawater. *Deep-Sea Research*, **28**, 625-629.

Mooers, C. N. K. 1973. A technique for the cross spectrum analysis of pairs of complex-valued time series, with emphasis on properties of polarized components and rotational invariants. *Deep-Sea Research*, **20**, 1129-1141.

Montgomery, R. B. 1941. Transport of the Florida Current off Habana. *Journal of Marine Research*, **4**(3), 198-219.

Munk, W. H. 1950. On the wind-driven ocean circulation. *Journal of Meteorology*, **7**(2), 79–93.

Murphree, T., Reynolds, C. 1995. El Niño and La Niña effects on the northeast Pacific: the 1991–1993 and 1988–1989 events. *California Cooperative Investigations Progress Report*, **36**, 45–56.

Murphree, T., Bograd, S. J., Schwing, F. B., Ford, B. 2003. Large-scale atmosphere-ocean anomalies in the northeast Pacific during 2002. *Geophysical Research Letters*, **30**(15), 8026, doi:10.1029/2003GL017303.

Nelson, C. S. 1977. Wind stress and wind stress curl over the California current. *U.S. Department of Commerce, NOAA Technical Report* NMFS-SSRF-714.

Oey, L.-Y. 1996. Flow around a coastal bend: A model of the Santa Barbara Channel eddy. *Journal of Geophysical Research*, **101**, 16667-16682.

Overland, J. E., Adams, J. M., Bond, N. A. 1999. Decadal variability of the Aleutian low and its relation to high latitude circulation. *Journal of Climate*, **12**, 1542–1548.

Pavlova, Y. V. 1966. Seasonal variations of the California Current. *Oceanology*, **6**, 806–814.

Pawlowicz, R., Beardsley, B., Lentz, S. 2002. Classical Tidal Harmonic Analysis Including Error Estimates in MATLAB using T_TIDE". *Computers and Geosciences.* **28**, 929-937.

Pedder, M. A., Gomis, D. 1998. Application of EOF Analysis to the spatial estimation of circulation features in the ocean sampled by high-resolution CTD samplings, *Journal of Atmospheric and Oceanic Technology*, 15(4), 959-978.

Pedlosky, J. 1974. Longshore currents, upwelling and bottom topography. *Journal of Physical Oceanography,* **4,** 214–226.

Pedlosky, J. 1978a. An inertial model of steady coastal upwelling. *Journal of Physical Oceanography,* **8,** 171–177.

Pedlosky, J. 1978b. A nonlinear model of the onset of upwelling. *Journal of Physical Oceanography,* **8,** 178–187.

Philander, S. G. H. 1980. The Equatorial Undercurrent revisited. *Annual Review of Earth and Planetary Sciences.* **8**, 191-204.

Philander, S. G. H., Yoon, J. H. 1982. Eastern boundary currents and coastal upwelling. *Journal of Physical Oceanography*, **12**, 862-879.

Pierce, S. D., Smith, R. L., Kosro, P. M., Barth, J. A., Wilson, C. D. 2000. Continuity of the poleward undercurrent along the eastern boundary of the mid-latitude north Pacific. *Deep-sea research. Part II - topical studies in oceanography*, **47**(5-6), 811-829.

Pugh, D. T. 1987. *Tides, Surges and Mean Sea-Level.* J. Wiley and Sons, 472 pp.

Rabinovich, A. B., Shevchenko, G. V., Thomson, R. E. 2007. Sea ice and current response to the wind: a vector regressional analysis approach. *Journal of atmospheric and oceanic technology*, **24**, 1086-1101, DOI: 10.1175/JTECH2015.1

Rasmusson, E. M., Wang, X., Ropelewski, C. F. 1995. Secular variability of the ENSO cycle. *Natural Climate Variability on Decade-to-Century Time Scales*, D. G. Martinson et al., (Eds.), National Academy Press, 458–471.

Reason, C. J. C., Dunkley, R. 1993. Coastally trapped stratus events in British Columbia. *Atmosphere-Ocean*, **31**, 235–258.

Rebstock G. A. 2003. Long-term change and stability in the California Current System: lessons from CalCOFI and other long-term data sets. *Deep-sea research. Part II - topical studies in oceanography*, **50**, 2583–2594.

Reed, R. K., Halpern, D. 1976. Observations of the California Undercurrent off Washington and Vancouver Island. *Limnology and oceanography.* **21** (3): 389-398.

Reed, R. K., Elliott, W. P. 1973. Freshwater Input to Coastal Waters Off the Pacific Northwest. *Limnology and Oceanography*, **18**(4), 683-686.

Reid, J. L., Jr. 1962. Measurements of the California Countercurrent at a depth of 250 m. *Journal of Marine Research*, **20**(2), 134–137.

Reid, J. L., Jr. 1963. Measurements of the California Countercurrent off Baja California. *Journal of Geophysical Research*, **68**(16), 4819–4822.

Reid, J. L., Jr. Roden, G. I., Wyllie, J. G. 1958. Studies of the California current system. *California Cooperative Investigations Progress Report*, **6**, 27-56.

Reid, J. L., Jr., Mantyla, A. W. 1976. The effect of the geostrophic flow upon coastal sea elevations in the northern North Pacific Ocean. *Journal of Geophysical Research*, **81**(18), 3100–3110.

Roden, G. I. 1967. On river discharge into the northeastern Pacific Ocean and the Bering Sea. *Journal of Geophysical Research*, **72**, 5613-29.

Roemmich, D. 1992. Ocean warming and sea level rise along the southwest US coast. *Science*, **257**, 373–375.

Roemmich, D., McGowan, J. A. 1995. Climatic warming and the decline of zooplankton in the California Current. *Science*, **267**, 1324–1326.

Royer, T. C. 1982. Coastal fresh water discharge in the Northeast Pacific. *Journal of Geophysical Research*, **87**, 2017–2021.

Sandström, I. W., Helland-Hansen, B. 1903. Über die Berechung von Meeresströmungen. *Reports on Norwegian Fishery and Marine Investigations*, **2**(4), Bergen, Norway, 43 pp.

Schwing, F. B., Mendelssohn, R. 1997. Increased coastal upwelling in the California Current System. *Journal of Geophysical Research*, **102**, 3421–3438.

Shevchenko, G. V., Rabinovich, A. B., Thomson, R. E. 2004. Sea-ice drift on the northeastern shelf of Sakhalin Island. *Journal of Physical Oceanography*, **34**, 2470-2490.

Simpson, J. J. 1984b. Warm and cold episodes in the California Current: a case for large-scale mid-latitude atmospheric forcing. *Proceedings of the Ninth Annual Climate Diagnostics Workshop, Corvallis, Oregon*. National Oceanic and Atmospheric Administration, US Department of Commerce, pp. 173–184.

Smith, R. L., Huyer, A., Fleischbein, J. 2001. The coastal ocean off Oregon from 1961 to 2000: Is there evidence of climate change or only of Los Niños? *Progress in Oceanography*, **49**, 63–93.

Steger, J., Collins, C., Chu, P. 1998. Circulation in the Archipiélago de Colón (Galapagos Islands), November, 1993. *Deep-sea research. Part II - topical studies in oceanography,* **45,** 1093-1114.

Stevenson, M., Taft, B. 1971. New evidence of the Equatorial Undercurrent east of the Galapagos Islands. *Journal of Marine Research*, **29,** 103-115.

Stewart, R. H. 2003. *Introduction to physical oceanography*. Internet edition. http://oceanworld.tamu.edu/home/course_book.htm

Stommel, H. 1948. The westward intensification of wind-driven ocean currents. *Transactions, American Geophysical Union*, **29** (2), 202–206.

Strub, P. T., Allen, J. S., Huyer, A., Smith, R. L. 1987a. Large-scale structure of the spring transition in the coastal ocean off western North America. *Journal of Geophysical Research*, **92**, 1527-1544.

Strub, P., Allen, J., Huyer, A., Smith, R., Beardsley, R. 1987b. Seasonal cycles of currents, temperatures, winds, and sea level over the northeast Pacific continental shelf: 35°N to 48°N, *Journal of Geophysical Research*, **92**(C2), 1507-1526.

Strub, P. T., Kosro, P. M., Huyer, A., Brink, K. H., Hayward, T. L., Niiler, P. P., James, C., Dewey, R. K., Walstad, L. J., Chavez, F., AND OTHERS. 1991. The nature of the cold filaments in the California current system. *Journal of Geophysical Research*, **96**, 14,743-14,768.

Sturges, W. 1967. Slope of sea level along the Pacific coast of the United States. *Journal of Geophysical Research*, **72**(14), 3627–3637.

Suginohara, N. 1982. Coastal-upwelling: Onshore-offshore circulation, equatorward coastal jet and poleward undercurrent over a continental shelf-slope. *Journal of Physical Oceanography*, **12**, 272–284.

Sverdrup, H. U. 1947. Wind-driven currents in a baroclinic ocean: with application to the equatorial currents of the eastern Pacific. *Proceedings of the National Academy of Sciences*, **33**(11), 318–326.

Sverdrup, H. U., Fleming, R. H. 1941. The waters off the coast of southern California, March to July 1937. *Scripps Institute of Oceanography Bulletin*. **4**(10), 261-387.

Sverdrup, H. U., Johnson, M. W., Fleming, R. H. 1942. *The Oceans: their Physics, Chemistry and General Biology*. Prentice-Hall, Englewood Cliffs, 1087 pp.

Tabata, S. 1975. The general circulation of the Pacific Ocean and a brief account of the oceanographic structure of the North Pacific. *Atmosphere*, **13**, 1034–1054.

Tabata, S., Weichselbaumer, W. E. 1992a. An update of the statistics of oceanographic dada based on hydrographic/CTD casts made at Stations 1 through 6 along Line P during January 1959 through September 1990. *Canadian Data Report of Hydrography and Ocean Sciences*, **108**, 317 pp.

Tabata, S., Weichselbaumer, W. E. 1992b. An update of the statistics of oceanographic dada based on hydrographic/CTD casts made at Stations 7 through 12 along Line P during January 1959 through September 1990. *Canadian Data Report of Hydrography and Ocean Sciences*, **109**, 343 pp.

Thomson, R. E. 1981 (Reprinted 1983, 1984, 1991) *Oceanography of the British Columbia Coast.* Canadian Special Publication of Fisheries and Aquatic Sciences, **56**, Ottawa, 291 pp.

Thomson, R. E. 1984. A cyclonic eddy over the continental margin of Vancouver Island: Evidence for baroclinic instability. *Journal of Physical Oceanography*, **14**, 1326-1348.

Thomson, R. E., Huggett, W. S. 1981. Wind-driven Inertial Oscillations of Large Spatial Coherence. *Atmosphere-Ocean*, **19**, 281-306.

Thomson, R. E., Crawford, W. R. 1982. The generation of diurnal period shelf waves by tidal currents. *Journal of Physical Oceanography*, **12**, 635-643.

Thomson, R. E., Gower, J. F. R. 1985. A wind-induced mesoscale eddy on the Vancouver Island continental slope. *Journal of Geophysical Research*, **90**, 8981-8993.

Thomson, R. E., Gower, J. F. R. 1998. A basin-scale oceanic instability event in the Gulf of Alaska. *Journal of Geophysical Research*, **103**(C2), 3033-3040.

Thomson, R. E. Stewart, R. W. 1977. The balance and redistribution of potential vorticity within the ocean. *Dynamics of Atmosphere and Oceans*, **1**, 299-321.

Thomson, R. E., Ware, D. M. 1996. A current velocity index of ocean variability. *Journal of Geophysical Research*, **101**, 14,297-14,310.

Thomson, R. E., Crawford, W. R., Huggett, W. S. 1984. Water property observations off the west coast of Vancouver Island during CODE: May 1979 to September 1980. *Canadian Data Report of Hydrography and Ocean Sciences*, **23**, Vol. 1-3.

Thomson, R. E., Crawford, W. R., Huggett, W. S. 1985. Low-pass filtered current records for the west coast of Vancouver Island: Coastal Oceanic Dynamics Experiment, 1979-81. *Canadian Data Report of Hydrography and Ocean Sciences*, **40**, 102 pp.

Thomson, R. E., Hickey, B. M., LeBlond, P. H. 1989. *The Vancouver Island Coastal Current: Fisheries barrier and Conduit*. In: Beamish, R. and McFarlane, G. (Eds.), Effects of ocean variability on recruitment and an evaluation of parameters used in stock assessment models. Canadian Special Publication of Fisheries and Aquatic Sciences, **108**, Ottawa, 265-296.

Thomson, R.E., Roth, S.E., Dymond, J. 1990. Near-inertial motions over a mid-ocean ridge: Effects of topography and hydrothermal vents. *Journal of Geophysical Research,* **95**, 7261-7278.

Thomson, R. E., LeBlond, P. H., Rabinovich, A. B. 1998. Satellite-tracked drifter measurement of inertial and semidiurnal currents in the northeast Pacific. *Journal of Geophysical Research*, **103**(C1), 1039-1052, DOI: 10.1029/97JC02374.

Tibby R. B. 1941. The water masses off the west coast of North America. *Journal of Marine Research*, **4**(2), 113-121.

Torgrimson, G. M., Hickey, B. M. 1979. Barotropic and baroclinic tides over the continental slope and shelf of Oregon. *Journal of Physical Oceanography*, **9** (5), 945-961.

Trenberth, K. E., Hoar, T. J. 1997. El Niño and climate change. *Geophysical Research Letters*, **24**, 3057–3060.

Wang, D.-P. 1982. Development of a three-dimensional, limited area (island) shelf circulation model. *Journal of Physical Oceanography*, **12**, 605-617.

Wang, D.-P. 1997. Effects of small-scale wind on coastal upwelling with application to Point Conception. *Journal of Geophysical Research*, **102**, 15,555-15,566.

Ware, D. M. 1995. A century and a half of change in the climate of the NE Pacific. *Fisheries Oceanography*, **4,** 267–277.

Ware, D., Thomson, R. 1986. La Perouse project first progress report 1985. *Department of Fisheries and Oceans report*, 25 pp.

Ware, D. M., Thomson, R. E. 2000. Interannual to multidecadal timescale climate variations in the northeast Pacific. *Journal of Climate*, **13**, 3209–3220.

Warren, B. A. 1992. Physical oceanography in *The Oceans*. *Oceanography*, **5**(3), 157-159.

Weinheimer, A. L., Kennett, J. P., Cayan, D. R. 1999. Recent increase in surface-water stability during warming off California as recorded in marine sediments. *Geology*, **27**, 1019–1022.

Werner, F. E., Hickey, B. M. 1983. The role of a longshore pressure gradient in Pacific Northwest coastal dynamics. *Journal of Physical Oceanography*, **13**, 395–410.

Whitney, F., Freeland, H. J. 1999. Variability in upper ocean water properties in the NE Pacific Ocean, *Deep-sea research. Part II - topical studies in oceanography*, **46**, 2351– 2370.

Wickham, J. B. 1975. Observations of the California Countercurrent. *Journal of Marine Research*, **33**(3), 325–340.

Wyrtki, K. 1967. Circulation and water masses in the eastern equatorial Pacific Ocean. *International Journal of Oceanology and Limnology*, **1**(2), 117–147.

Yamazaki, H., Lueck, R. 1987. Turbulence in the California Undercurrent. *Journal of Physical Oceanography*, **17**, 1378–1396.

Yoshida, K. 1955. Coastal upwelling off the California coast. *Records of Oceanographic Works in Japan*, **2**(2), 1–13.

Yoshida, K., Mao, H. L. 1967. Circulation in the eastern tropical oceans with special reference to upwelling and undercurrents. *Japanese Journal of Geophysics*, **4**(2), 1-75.

Zetler, B. D., Schuldt, M. D., Whipple, R. W., Hicks, S. D. 1965. Harmonic analysis of tides from data randomly spaced in time. *Journal of Geophysical Research*, **70**(12), 2805-2811.

Web resources:

IRI (the International Research Institute for Climate and Society) website: http://iri.columbia.edu/climate/ENSO/background/monitoring.html Overview of the ENSO System; accessed on Jan 8, 2008.

Levitus (NODC) World Ocean Atlas 1994. Data provided by the NOAA/OAR/ESRL PSD, Boulder, Colorado, USA, from their Web site at http://www.cdc.noaa.gov/cdc/data.nodc.woa94.html

MEDS data collection: http://www.meds-sdmm.dfo-mpo.gc.ca/meds/Databases/Data_e.htm

North Pacific Index data provided by the Climate Analysis Section, National Center for Atmospheric Research, Boulder, USA, Trenberth and Hurrell (1994). Website: http://www.cgd.ucar.edu/cas/jhurrell/npindex.html; accessed on Jan 8, 2008.

NCEP Reanalysis data provided by the NOAA-CIRES Climate Diagnostics Center, Boulder, Colorado, USA, from their Web site at http://www.cdc.noaa.gov/cdc/reanalysis/ (accessed on January 4, 2007)

Appendices

Appendix A. Instrument depth corrected according to the pressure records

Table A1. Recorded and corrected instrument depth.

Deployment number and file	Original	Corrected
LAP06\A1_029	29	55
LAP10\A1_0035	35	60
LAP14\A1_0035	35	50
LAP16\A1_0035	35	15
LAP21C\A01C0035	35	70
LAP24\A1_035	35	55
LAP25\A1_032	32	15
Lap37\a1_036	36	55
lap34\a1_027	27	50
LAP10\A1_0100	100	125
LAP14\A1_0100	100	95
LAP16\A1_0100B	100	80
LAP18\A1_0100	100	115
LAP24\A1_100	100	120
LAP25\A1_097	97	87
LAP30\A1_116	97	115
lap36\a1_121	101	120
LAP10\A1_0175	175	200
LAP16\A1_0175	175	155
LAP24\A1_175	175	195
LAP25\A1_172	172	162
LAP26\A1_196	196	206
LAP10\A1_0400	400	425
LAP16\A1_0400	400	380
LAP25\A1_397	397	387
LAP26\A1_421	421	431
LAP29\A1_435	399	434
lap34\a1_397	397	417
lap36\a1_421	401	421

Appendix B. Comparison of M. Foreman's (T_TIDE) and A. Rabinovich's (LSM) tidal analysis routines.

Both T_ TIDE and LSM are tidal harmonic analysis routines. The procedure is described in Pugh (1987) and Emery and Thomson (2001). The method is based on the least squares fit of sinusoidal signals of specific frequencies (known as tidal constituents) to the data series. Therefore, if the same set of tidal harmonics is specified, both routines should give similar results. Each of these two software packages has a built-in set of tidal harmonics. All but two constituents, common to both sets, differ in frequency only because of different precision used to store the data in these two routines. Exceptions are a pair NO1 (T_TIDE) and M1 (LSM) and a pair OQ2 (T_TIDE) and OQ2 (LSM), with frequencies different by 0.03% between the two software packages. This discrepancy can give different estimates for these particular harmonics, but will not influence the overall tide and residual estimates. The corresponding tidal frequencies for the two packages can, therefore, be considered identical for practical purposes.

A test run for both routines was performed on one-month- and one-year-long series of sea level records at the Tofino tide gauge station on the west coast of Vancouver Island (see Figure 3.1.1) where the range of tidal oscillations is approximately 4 m. Tables B1 and B2 show the results of the analyses. The amplitudes of the constituents calculated by LSM and T_TIDE do not differ by more than 1 cm, most of them (including major constituents) being within 1 mm difference. The phase difference is usually within several degrees. For the significant (at 95% level) constituents, the relative differences in amplitude greater than 10% and phase differences greater than 10^o are shaded. For the shaded constituents, the discrepancies can be significant, although because the amplitude of these constituents is small, the effect on the overall tidal signal estimate is negligible. Therefore, the calculations by both LSM and T_TIDE show results so close that the routines can be considered interchangeable for the purposes of tidal estimation and subtraction (provided that an identical set of harmonics is specified for analysis). There are, however, some differences which can make one routine more suitable for certain tasks. One example is the investigation of radiational tides. LSM has a set of harmonics corresponding to radiational tidal frequencies, namely S3, S5, S7, S8, and S9, which are absent in T_TIDE, in addition to S1, S2, and S4, which are present in both sets. LSM is also more flexible in prediction and subtraction of tidal and other periodic signals since it allows specification of customised frequencies. Among the advantages of T_TIDE is the larger set of harmonics (146 versus 67 for LSM) which can slightly improve tidal prediction for long and low-noise records (usually sea level records) with strong non-linear effects. T_TIDE has also an option for automatic selection of harmonics based on the Rayleigh criterion. This method, however, should be used with care, since other factors, such as the ratio of the tidal signal strength to noise, are also important. An individual approach in each particular situation is preferable as it usually gives better results, although it demands greater expertise from the researcher. The illustration is the test run on the series described above: T_TIDE with an automatic selection of constituents gave higher residual variance for both series than the run with a manually selected set of constituents.

Table B1. Comparison of LSM and T_TIDE tidal analysis output for one month long series (January 2003) of Tofino sea level. Grey-coloured constituents are not significant at 95% level. For significant constituents, the relative differences in amplitude greater than 10% are shaded. Residual variance for LSM is 3.99% and for T_TIDE is 3.86% (T_TIDE with automatic constituent selection 4.00%).

Constituent	Frequency	Amplitude (cm)					Phase (deg)			
		LSM	T_TIDE	95%conf	Diff.abs	Diff%	LSM	T_TIDE	95%conf	Diff.abs
Q1	13.398661	3.5964	3.5791	0.9939	-0.0173	-0.48	233.13	231.30	13.88	-1.83
O1	13.943036	24.4585	24.5676	0.7964	0.1091	0.45	225.17	224.77	2.24	-0.40
P1	14.958931	12.8321	12.9939	0.9922	0.1618	1.26	240.73	241.01	3.83	0.29
K1	15.041069	38.7677	39.2564	0.9314	0.4887	1.26	240.73	241.01	1.26	0.29
J1	15.585443	2.2189	2.3536	0.7780	0.1347	6.07	274.75	279.12	24.49	4.37
OO1	16.139102	0.6066	0.5118	0.6088	-0.0948	-15.62	241.47	238.39	84.33	-3.08
MU2	27.968208	0.1653	0.1554	0.5589	-0.0099	-6.00	74.00	93.37	197.49	19.37
N2	28.439729	16.6053	16.5690	0.8574	-0.0363	-0.22	215.78	215.52	2.58	-0.26
M2	28.984104	98.2678	98.2566	0.8709	-0.0112	-0.01	239.74	239.92	0.45	0.18
L2	29.528479	2.7462	2.6893	1.0566	-0.0569	-2.07	277.80	278.64	24.19	0.84
S2	30.000000	31.8352	31.3810	0.8009	-0.4542	-1.43	269.77	270.57	1.35	0.80
K2	30.082137	8.6624	8.5388	0.7290	-0.1236	-1.43	269.77	270.57	4.87	0.80
MO3	42.927140	0.5591	0.5734	0.3548	0.0143	2.55	57.25	62.12	34.63	4.86
M3	43.476156	0.2014	0.2421	0.3423	0.0407	20.20	298.94	307.76	104.12	8.82
MK3	44.025173	0.8983	0.8979	0.3459	-0.0004	-0.05	103.04	106.57	22.93	3.53
M4	57.968208	1.9247	1.9665	0.5498	0.0418	2.17	109.63	111.35	17.69	1.71
MS4	58.984104	1.0869	1.1453	0.6196	0.0584	5.38	149.23	149.07	31.21	-0.16
M6	86.952313	0.3709	0.3320	0.2952	-0.0389	-10.50	13.73	22.88	60.27	9.15

Table B2. Comparison of LSM and T_TIDE tidal analysis output for one year long series (2003) of Tofino sea level. Grey-coloured constituents are not significant at 95% level. For significant constituents, the relative differences in amplitude greater than 10% and phase differences greater than 10^o are shaded. Residual variance for LSM is 2.24% and for T_TIDE is 2.41% (T_TIDE with automatic constituent selection 4.04%).

Constituent	Frequency	Amplitude (cm)					Phase (deg)			
		LSM	T_TIDE	95%conf	Diff.abs	Diff%	LSM	T_TIDE	95%conf	Diff.abs
SA	0.041069	14.9110	14.9083	3.7888	-0.0027	-0.02	290.53	7.53	14.91	77.00
SSA	0.082137	1.3253	1.3231	3.0608	-0.0022	-0.16	149.58	149.46	136.05	-0.13
MM	0.544375	1.3364	1.2442	2.6158	-0.0922	-6.90	273.52	273.61	138.37	0.09
MSF	1.015896	3.0385	2.9765	3.3654	-0.0620	-2.04	266.80	265.03	67.64	-1.78
MF	1.098033	2.6497	3.3614	3.3353	0.7117	26.86	210.64	228.24	67.37	17.60
2Q1	12.854286	0.4703	0.4842	0.2149	0.0139	2.95	213.97	210.57	26.58	-3.40
SIG1	12.927140	0.5531	0.5611	0.2265	0.0080	1.45	216.50	215.29	20.20	-1.20
Q1	13.398661	4.3366	4.4260	0.2080	0.0894	2.06	222.00	220.37	2.43	-1.63
RO1	13.471515	0.8576	0.8490	0.2149	-0.0086	-1.00	215.65	213.29	13.44	-2.36
O1	13.943036	24.6549	24.6461	0.1773	-0.0088	-0.04	227.27	226.87	0.50	-0.40
MP1	14.025173	0.6895	0.7371	0.2507	0.0476	6.91	177.82	199.00	20.76	21.18
M1	14.492052	1.0855	1.5670	0.1822	0.4815	44.36	236.65	239.94	6.39	3.29
HI1	14.569548	0.3916	0.3388	0.1888	-0.0528	-13.48	236.18	250.92	33.17	14.74
PI1	14.917865	0.5308	0.5334	0.2231	0.0026	0.50	259.67	260.85	22.30	1.18
P1	14.958931	12.2867	12.3586	0.2349	0.0719	0.59	239.01	238.43	0.93	-0.58
S1	15.000000	1.1584	1.6725	0.3247	0.5141	44.38	50.98	259.01	11.82	-151.97
K1	15.041069	38.8567	38.8330	0.2164	-0.0237	-0.06	241.17	241.18	0.28	0.02
PSI1	15.082135	0.2949	0.2905	0.2159	-0.0044	-1.51	115.14	112.58	47.08	-2.55
FI1	15.123206	0.6827	0.7093	0.2102	0.0266	3.90	258.31	258.98	20.35	0.66
TET1	15.512590	0.5141	0.4975	0.2167	-0.0166	-3.23	263.98	262.48	22.21	-1.50
J1	15.585443	2.4939	2.6475	0.2408	0.1536	6.16	256.39	259.21	4.73	2.83
SO1	16.056964	0.8115	0.8144	0.2134	0.0029	0.36	277.57	278.04	14.35	0.47
OO1	16.139102	1.3417	1.2790	0.1629	-0.0627	-4.68	272.04	266.79	6.05	-5.26
OQ2	27.341696	0.1188	0.1999	0.1643	0.0811	68.23	255.33	152.30	44.06	-103.03
MNS2	27.423834	0.4380	0.4638	0.1616	0.0258	5.90	214.62	214.66	18.50	0.04
2N2	27.895355	2.2697	2.4792	0.1724	0.2095	9.23	189.84	182.14	3.99	-7.70
MU2	27.968208	1.8214	1.8429	0.1714	0.0215	1.18	201.06	199.94	4.77	-1.12
N2	28.439729	20.1949	20.2629	0.1549	0.0680	0.34	216.54	216.49	0.45	-0.05
NU2	28.512583	3.9330	3.9717	0.1474	0.0387	0.98	220.47	220.94	2.64	0.47
OP2	28.901967	0.6045	0.6055	0.1411	0.0010	0.17	143.63	142.85	12.39	-0.77
M2	28.984104	98.0125	98.0610	0.1497	0.0485	0.05	240.05	240.25	0.08	0.20
MKS2	29.066242	0.1439	0.1467	0.1167	0.0028	1.97	112.00	112.34	50.14	0.33
LD2	29.455625	0.7017	0.7051	0.1577	0.0034	0.48	247.16	246.57	12.83	-0.59
L2	29.528479	1.8849	1.8958	0.1715	0.0109	0.58	249.66	249.71	4.21	0.04
T2	29.958933	1.7059	1.7054	0.1368	-0.0005	-0.03	258.94	259.84	5.09	0.90
S2	30.000000	28.1874	28.1567	0.1479	-0.0307	-0.11	269.26	269.37	0.29	0.11
R2	30.041067	0.2792	0.2299	0.1094	-0.0493	-17.67	275.26	280.33	29.94	5.07
K2	30.082137	7.7882	7.7646	0.1369	-0.0236	-0.30	262.60	262.82	0.83	0.22
MSN2	30.544375	0.2280	0.2258	0.1476	-0.0022	-0.94	64.57	64.42	35.77	-0.15
KJ2	30.626512	0.5172	0.5263	0.1297	0.0091	1.76	105.84	290.84	13.84	-175.00
2SM2	31.015896	0.2728	0.2729	0.1358	0.0001	0.02	68.72	68.28	32.49	-0.44
MO3	42.927140	0.5139	0.5167	0.0863	0.0028	0.54	62.34	62.18	8.92	-0.16
M3	43.476156	0.3740	0.3752	0.1044	0.0012	0.33	305.44	305.71	15.77	0.27
SO3	43.943036	0.3775	0.3743	0.0782	-0.0032	-0.84	95.77	95.41	13.70	-0.36
MK3	44.025173	0.6137	0.6111	0.0997	-0.0026	-0.42	81.38	81.45	8.00	0.08
SK3	45.041069	0.3392	0.3399	0.0851	0.0007	0.22	79.61	80.12	13.34	0.50
MN4	57.423834	0.7885	0.7885	0.0899	0.0000	0.00	94.79	94.89	6.18	0.10
M4	57.968208	1.7842	1.7875	0.0936	0.0033	0.18	115.98	116.30	2.94	0.31
SN4	58.439729	0.2143	0.2175	0.0768	0.0032	1.50	141.73	141.79	22.89	0.06
MS4	58.984104	0.9593	0.9568	0.0842	-0.0025	-0.26	143.68	144.13	5.11	0.46
MK4	59.066241	0.3038	0.3043	0.0735	0.0005	0.17	156.84	156.83	13.66	-0.02
S4	60.000000	0.0972	0.0990	0.0736	0.0018	1.88	164.16	163.34	46.02	-0.82
SK4	60.082137	0.0680	0.0663	0.0580	-0.0017	-2.51	179.84	181.74	52.45	1.90
2MN6	86.407938	0.3128	0.3158	0.0645	0.0030	0.96	354.52	355.32	13.88	0.81
M6	86.952313	0.4087	0.4065	0.0610	-0.0022	-0.53	20.56	21.23	9.71	0.67
MSN6	87.423834	0.1020	0.1014	0.0675	-0.0006	-0.61	11.47	10.15	34.83	-1.32
2MS6	87.968208	0.4345	0.4374	0.0608	0.0029	0.68	40.85	41.32	8.17	0.47
2MK6	88.050346	0.2003	0.1975	0.0478	-0.0028	-1.40	22.79	23.16	16.49	0.37
2SM6	88.984104	0.1375	0.1344	0.0623	-0.0031	-2.24	83.83	84.68	26.46	0.84
MSK6	89.066242	0.0786	0.0807	0.0558	0.0021	2.71	52.53	53.60	39.63	1.08
S6	90.000000	0.0157	0.0183	0.0426	0.0026	16.73	81.78	83.74	171.36	1.96
M8	115.936417	0.2218	0.2230	0.0577	0.0012	0.55	243.50	245.02	15.12	1.52